

NORTHWESTERN UNIVERSITY

Search for Higgs Boson Decays to a Z Boson and a Photon

A DISSERTATION

SUBMITTED TO THE GRADUATE SCHOOL
IN PARTIAL FULFILLMENT OF THE REQUIREMENTS

for the degree

DOCTOR OF PHILOSOPHY

Field of Physics

By

James Bueghly

EVANSTON, ILLINOIS

June 2022

© Copyright by James Bueghly 2022

All Rights Reserved

ABSTRACT

Search for Higgs Boson Decays to a Z Boson and a Photon

James Bueghly

Since its discovery in 2012 at the Large Hadron Collider (LHC), efforts have been made to measure and characterize the properties of the Higgs boson. Among these efforts have been searches for rare decays of the Higgs predicted by the standard model (SM) of particle physics. One such decay is the process $H \rightarrow Z\gamma$, which has an expected branching fraction of $\mathcal{B}(H \rightarrow Z\gamma) = (1.57 \pm 0.09) \times 10^{-3}$ in the SM, assuming a Higgs boson mass of $m_H = 125.38$ GeV. This decay mode has not yet been experimentally observed, and its observation and measurement remains an important goal of Higgs physics research at the LHC. In addition, a measurement of this decay mode at a rate deviating from the SM prediction would provide indirect evidence of new physics beyond the SM.

This thesis presents a search for $H \rightarrow Z\gamma$, where $Z \rightarrow \ell^+\ell^-$ with $\ell = e$ or μ . The search is performed using a sample of proton-proton (pp) collision data at a center-of-mass energy of 13 TeV, recorded by the Compact Muon Solenoid experiment at the LHC, corresponding to an integrated luminosity of 138 fb^{-1} . Events are assigned to mutually exclusive categories, which exploit differences in both event topology and kinematics of

distinct Higgs production mechanisms to enhance signal sensitivity. To detect a potential signal, fits are performed to the distributions of $\ell^+\ell^-\gamma$ invariant mass in each of these categories simultaneously. The signal strength μ , defined as the product of the cross section and the branching fraction [$\sigma(pp \rightarrow H)\mathcal{B}(H \rightarrow Z\gamma)$] relative to the SM expectation, is found to be $\mu = 2.4 \pm 0.9$ for $m_H = 125.38$ GeV. This measurement corresponds to $\sigma(pp \rightarrow H)\mathcal{B}(H \rightarrow Z\gamma) = 0.21 \pm 0.08$ pb. The statistical significance of the observed excess of events is 2.7 standard deviations. The observed (expected) upper limit at 95% confidence level on μ is 4.1 (1.8). The ratio of branching fractions $\mathcal{B}(H \rightarrow Z\gamma)/\mathcal{B}(H \rightarrow \gamma\gamma)$ is measured to be $1.5^{+0.7}_{-0.6}$, which agrees with the SM prediction at the 1.5 standard deviation level.

Acknowledgements

I would like to thank my adviser, Mayda Velasco, for the opportunity to pursue a goal I dreamed up years ago and for her support along the way. I'd also like to thank my many colleagues at Northwestern University, National Central University in Taiwan, CERN, and Fermilab who helped me grow both as a scientist and a person over the course of my Ph.D.

Special thanks are due to those who significantly impacted the work contained in this thesis: My coanalyzer Ming-Yan Lee, whose discipline and tireless work ethic kept us all going through the many challenges we faced; postdoc Andrew Gilbert, whose expertise and guidance were critical; and the CMS leaders who guided and reviewed our work, including the Higgs conveners, Analysis Review Committee, and our colleague and language editor Jeff Richman. Without all of you, this thesis would not exist.

To my Northwestern colleagues: I will always be grateful for your friendship over these years. The moments we shared away from the work kept me sane, focused, and balanced. It is impossible to name everyone here, but Nate Odell, Brian Pollack, Thoth Gunter, Joseph Cordero Mercado, and Ziheng Chen, thanks for your part in this.

Last, but not least, I want to thank my parents, sisters, and friends. You all have shown me so much love, encouragement, and patience throughout this process. For that, I feel extremely fortunate. This is for all of you.

Table of Contents

ABSTRACT	3
Acknowledgements	5
Table of Contents	6
List of Tables	9
List of Figures	11
Chapter 1. Introduction	24
Chapter 2. Theory	28
2.1. The Standard Model	28
2.2. The Elementary Particles	28
2.3. Electroweak Theory	30
2.4. Spontaneous Symmetry Breaking (Higgs Mechanism)	31
2.5. Higgs Production	37
2.6. Higgs Decay	38
2.7. Physics Beyond the Standard Model	39
Chapter 3. Experiment Description	43
3.1. The Large Hadron Collider	43

3.2. The Compact Muon Solenoid	45
3.3. Trigger System	51
3.4. Object Reconstruction	53
Chapter 4. Analysis Overview	60
4.1. History of the $H \rightarrow Z\gamma$ Search	60
4.2. The CMS Run 2 Strategy	63
Chapter 5. Data and Simulated Samples	65
5.1. $Z+jets$ Overlap Removal	68
5.2. Photon Internal Conversion	68
5.3. Transverse Momentum Reweighting	69
5.4. Pileup Reweighting	70
5.5. Level-1 Trigger Prefiring Reweighting	71
Chapter 6. Physics Object and Event Selection	73
6.1. Primary Vertex	73
6.2. Triggers	73
6.3. Photon Selection	76
6.4. Electron Selection	81
6.5. Muon Selection	83
6.6. Jet Selection	84
6.7. Object Corrections	85
6.8. Event Selection	86
6.9. Kinematic Fit	87

6.10. Yields and Kinematic Distributions	88
Chapter 7. Event Categorization	91
7.1. Kinematic Boosted Decision Tree	92
7.2. Vector Boson Fusion Boosted Decision Tree	96
7.3. Categorization Procedure	103
Chapter 8. Statistical Analysis	107
8.1. Signal Modeling	107
8.2. Resonant Background Modeling	108
8.3. Nonresonant Background Modeling	108
8.4. Obtaining Results	119
Chapter 9. Systematic Uncertainties	123
Chapter 10. Results and Interpretation	127
10.1. Ratio Measurement	130
Chapter 11. Conclusion	133
References	135
Appendix A. Shower Shape Corrections	144
Appendix B. Signal Fits	149
Appendix C. Resonant Background Fits	156
Appendix D. Nuisance Parameter Impacts	158

List of Tables

5.1	Summary of MINIAOD data samples used.	66
5.2	Simulated event samples used in the analysis. For Higgs samples, the listed cross sections and branching fractions correspond to the values for $m_H = 125$ GeV.	67
6.1	Photon conversion-safe electron veto SFs.	79
6.2	Expected signal and data yields corresponding to each year of data-taking in the electron and muon channels.	89
7.1	Importance of the kinematic BDT training features.	98
7.2	Importance of the VBF BDT training features.	103
7.3	Summary of the category definitions. The lepton-tagged category requires at least one additional electron or muon. Dijet categories are defined by regions of \mathcal{D}_{VBF} and untagged categories are defined by regions of \mathcal{D}_{kin} .	105
7.4	Yields and approximate significance (S/\sqrt{B}) for each category, where S and B are the expected number of signal and background events in the narrowest $m_{\ell^+\ell^-\gamma}$ interval containing 95% of the expected signal distribution. Also shown is the $m_{\ell^+\ell^-\gamma}$ resolution, computed using the	105

narrowest interval containing 68% of the expected signal distribution.

106

8.1 Bias and coverage results for each category. 121

9.1 Sources of systematic uncertainty affecting the simulated signal. The normalization effect on the expected yield, or the effect on the signal shape parameters, is given as indicated, with the values averaged over all event categories. The third column shows the uncertainties that have a correlated effect across the three data-taking periods. 126

List of Figures

1.1	Feynman diagrams for $H \rightarrow Z\gamma$ decay.	25
2.1	Table of elementary particles in the SM. The leftmost three columns correspond to three generations of fermions, the fourth column from the left shows the gauge bosons which mediate the elementary forces, and the rightmost column shows the Higgs boson. For each particle, mass, charge, and spin are labeled, with mass values given as of 2019.	29
2.2	Comparison of the shapes of complex scalar potentials without symmetry breaking (left) and with spontaneous symmetry breaking (right). The transverse axes represent the real-imaginary Φ plane, and the vertical axis represents the magnitude of the potential $V(\Phi)$. The diagram at right corresponds to the shape of the Higgs potential in the SM.	33
2.3	Cross sections for different Higgs boson production mechanisms as a function of center of mass energy for $m_H = 125$ GeV.	37
2.4	Branching fractions for different Higgs decay modes as a function of m_H .	38
2.5	Contours of constant branching fraction enhancement relative to the SM for the W' (left), charged scalar (center), and charged lepton	

(right) scenarios. The solid lines represent contours of enhancement in $\mathcal{B}(H \rightarrow Z\gamma)$, while the dashed lines correspond to $H \rightarrow \gamma\gamma$. The yellow boxed numbers label the enhancement for each $H \rightarrow Z\gamma$ contour, and the unboxed numbers label the enhancement for each $H \rightarrow \gamma\gamma$ contour.	40
2.6 Ratio of decay widths $\Gamma(H \rightarrow Z\gamma)/\Gamma(H \rightarrow \gamma\gamma)$ as a function of the mass coefficient of the additional scalar field(s) for seven BSM models with extended Higgs sectors. The models plotted on the left correspond to one additional singly-charged boson, and those on the right to one additional singly-charged and one additional doubly-charged boson.	41
2.7 Examples of two-loop diagrams contributing to $H \rightarrow Z\gamma$ decay.	42
3.1 CERN accelerator complex.	44
3.2 CMS detector apparatus.	46
3.3 Cross section of the CMS inner tracking system in the r-z plane.	47
3.4 Response of the CMS ECAL crystals to injected laser light as a function of time, broken into regions of $ \eta $.	49
3.5 Diagram of the CMS detector in the r-z plane showing the components of the muon system.	51
3.6 Visualization of different types of particles interacting with the CMS detector.	54

3.7	Energy resolution for simulated electrons in the barrel (left) and endcaps (right) as a function of generated p_{T} . The green markers represent tracker measurement only, the orange markers represent ECAL measurement only, and the purple markers represent the combination of tracker and ECAL information.	55
3.8	Left: dimuon mass resolution as a function of leading muon η for $Z \rightarrow \mu^+ \mu^-$ events in 2018 data and simulation. Right: reconstructed dimuon mass.	57
3.9	An example of the first few steps of the anti- k_{T} jet clustering algorithm.	58
3.10	Jet energy resolution as a function of simulated jet p_{T} in the barrel (left) and in the endcap (right) regions. Calo refers to the sum of ECAL and HCAL energy deposits, while PF corresponds to jets clustered from PF particles using the anti- k_{T} algorithm.	59
4.1	ATLAS (left) and CMS (right) Run 1 limit results as a function of m_{H} .	62
4.2	Left: CMS 2016 limit results as a function of m_{H} . Right: ATLAS Run 2 signal plus background fit, for $m_{\text{H}} = 125.09 \text{ GeV}$, weighted by $\ln(1+S_{68}/B_{68})$, where S_{68} and B_{68} are the expected signal and background events in an $m_{\ell^+\ell^-\gamma}$ window containing 68% of the expected signal yield.	63

5.1	Left: Background simulation modeling of $p_T^{\ell^+\ell^-\gamma}$ in each data-taking year. There is a shape discrepancy between 2016 and 2017–2018 due to the updated underlying event tuning. Right: Final comparison between data and simulation after the $p_T^{\ell^+\ell^-\gamma}$ reweighting is performed on 2017 and 2018 background simulation.	70
5.2	Distributions of the number of primary vertices in data and simulation for $e^+e^-\gamma$ events in 2016 (left), 2017 (center), and 2018 (right) after pileup reweighting.	71
6.1	Efficiency measurements for each leg of the double electron trigger in 2016 (left), 2017 (center), and 2018 (right). The upper (lower) plots correspond to the leading (subleading) trigger leg.	75
6.2	Efficiency measurements for each leg of the double muon trigger in 2016 (left), 2017 (center), and 2018 (right). The upper (lower) plots correspond to the leading (subleading) trigger leg.	76
6.3	Comparison of simulation with 2017 data for the photon MVA ID before and after shower shape corrections are applied to the simulation. The plots on the left (right) correspond to the barrel and endcap regions, and the upper (lower) plots correspond to $Z \rightarrow e^+e^-$ ($Z \rightarrow \mu^+\mu^- + \gamma$) events.	78
6.4	ROC curves for the corrected photon MVA ID in the barrel (red) and endcaps (blue). Here, signal refers to real photons from the $Z\gamma$ simulation and background refers to jets misreconstructed as photons	

from the Z+jets simulation. Also shown are the cuts used for the H → Z γ analysis WP and for the standard CMS 90% WP.	79
6.5 Left: Photon MVA ID efficiency SFs for 2016 (upper), 2017 (middle), and 2018 (lower). Right: The corresponding uncertainties for the SFs.	80
6.6 Left: Electron MVA ID efficiency SFs for 2016 (upper), 2017 (middle), and 2018 (lower). Right: The corresponding uncertainties for the SFs.	82
6.7 Dimuon invariant mass around the Z boson peak in 2018 data before (left) and after (right) the muon Rochester momentum corrections are applied.	85
6.8 Dilepton invariant mass (left) and $\ell^+\ell^-\gamma$ invariant mass (right) with (blue) and without (red) FSR photon recovery for simulated H → Z γ → $\mu^+\mu^-\gamma$ events containing at least one FSR photon.	86
6.9 Dilepton invariant mass in 2016 data before and after the kinematic fit for the electron (left) and muon (right) channels.	88
6.10 Basic kinematic distributions after event selection. The top (middle) row shows the p_T (η) of the photon (left), leading lepton (middle), and trailing lepton (right). From left to right, the bottom row shows the dilepton mass, p_T/m of the $\ell^+\ell^-\gamma$ system, and corrected $m_{\ell^+\ell^-\gamma}$ after the kinematic fit is performed.	90
7.1 Definitions of theoretical angles used for kinematic BDT training. The left diagram is in the Higgs boson center-of-mass frame, and the right diagram is in the Z boson center-of-mass frame.	93

7.2	Top: Expected theoretical shapes for the angular features used for kinematic BDT training. Bottom: Reconstructed shapes for these quantities after the $H \rightarrow Z\gamma$ selection requirements have been applied. Please note that the red and blue color conventions are reversed for the top and bottom plots.	94
7.3	Comparison of reconstructed signal and background shapes for several kinematic variables used for kinematic BDT training. The blue histograms represent the signal, while the red histograms represent the background.	95
7.4	Comparison of reconstructed signal and background shapes for the photon quality features used for kinematic BDT training. The blue histograms represent the signal, while the red histograms represent the background.	96
7.5	Comparison of data and simulation for the kinematic BDT training features. The plotted distributions include data and simulated samples from the combination of the three data-taking years in both the electron and muon channels.	97
7.6	Shapes of the kinematic BDT distributions for signal and background for both training and test sets. No BDT overtraining is observed.	98
7.7	Comparison of signal and background shapes for the kinematic features used for VBF BDT training. The blue histograms represent	

	the VBF signal, while the red histograms represent the training background, including ggH $H \rightarrow Z\gamma$ events.	100
7.8	Comparison of signal and background shapes for several variables used for VBF BDT training. The blue histograms represent the VBF signal, while the red histograms represent the training background, including ggH $H \rightarrow Z\gamma$ events.	101
7.9	Comparison of data and simulation for the VBF BDT training features. The plotted distributions include data and simulated samples from the combination of the three data-taking years in both the electron and muon channels.	102
7.10	Shapes of the VBF BDT distributions for signal and background for both training and test sets. No BDT overtraining is observed.	103
7.11	The \mathcal{D}_{VBF} (left) and \mathcal{D}_{kin} (right) distributions for signal, simulated background, and data. The \mathcal{D}_{VBF} distribution includes only dijet-tagged events, and the \mathcal{D}_{kin} distribution includes only untagged events. The sum of contributions from all signal production mechanisms is shown by the blue line, while the contribution from only the VBF mechanism is shown by the red line. The uncertainty band incorporates all statistical and systematic uncertainties in the expected background. The dashed lines indicate the boundaries for the dijet and untagged categories. The gray shaded region in the \mathcal{D}_{kin} distribution is excluded from the analysis.	104

- 8.1 Fits to simulated $m_{\ell^+\ell^-\gamma}$ signal distributions in the electron channel for $m_H = 125$ GeV for the 2016 data-taking period. The blue line shows the total fit function, the green line shows the Crystal Ball function component, and the red line shows the Gaussian function component. The top four plots correspond to the untagged categories, and the bottom three plots correspond to the dijet categories. 109
- 8.2 Fits to simulated $m_{\ell^+\ell^-\gamma}$ signal distributions in the muon channel for $m_H = 125$ GeV for the 2016 data-taking period. The blue line shows the total fit function, the green line shows the Crystal Ball function component, and the red line shows the Gaussian function component. The top four plots correspond to the untagged categories, and the bottom three plots correspond to the dijet categories. 110
- 8.3 Fits to simulated $m_{\ell^+\ell^-\gamma}$ signal distributions in the electron and muon channels combined in the lepton-tagged category for $m_H = 125$ GeV for the 2016 data-taking period. The left plot shows the fit to simulated ZH production events, and the right plot shows the fit to simulated WH production events. The blue line shows the total fit function, the green line shows the Crystal Ball function component, and the red line shows the Gaussian function component. 111
- 8.4 Comparison of background fits with and without modeling the turn-on. The top four plots correspond to the untagged categories, and the bottom four plots correspond to the dijet categories and lepton-tagged category. 113

- 8.5 Background functions selected for the envelope in each category. The top four plots correspond to the untagged categories, and the bottom four plots correspond to the dijet categories and lepton tag category. 120
- 10.1 Fits to the $m_{\ell^+\ell^-\gamma}$ data distribution in the lepton-tagged (upper left), dijet 1 (upper right), dijet 2 (lower left), and dijet 3 (lower right) categories. In the upper panel, the red solid line shows the result of a signal-plus-background fit to the given category. The red dashed line shows the background component of the fit. The green and yellow bands represent the 68 and 95% CL uncertainties in the fit. Also plotted is the expected SM signal, scaled by a factor of 10. In the lower panel, the data minus the background component of the fit is shown. 128
- 10.2 Fits to the $m_{\ell^+\ell^-\gamma}$ data distribution in the untagged 1 (upper left), untagged 2 (upper right), untagged 3 (lower left), and untagged 4 (lower right) categories. In the upper panel, the red solid line shows the result of a signal-plus-background fit to the given category. The red dashed line shows the background component of the fit. The green and yellow bands represent the 68 and 95% CL uncertainties in the fit. Also plotted is the expected SM signal, scaled by a factor of 10. In the lower panel, the data minus the background component of the fit is shown. 129

10.3	Sum over all categories of the data points and signal-plus-background model after the simultaneous fit to each $m_{\ell^+\ell^-\gamma}$ distribution. The contribution from each category is weighted by $S/(S + B)$, as defined in the text. In the upper panel, the red solid line shows the signal-plus-background fit. The red dashed line shows the background component of the fit. The green and yellow bands represent the 68 and 95% CL uncertainties in the fit. Also plotted is the expected SM signal weighted by $S/(S + B)$ and scaled by a factor of 10. In the lower panel, the data minus the background component of the fit is shown.	130
10.4	Observed signal strength (μ) for a SM Higgs boson with $m_H = 125.38 \text{ GeV}$. The labels “untagged combined,” “dijet combined,” and “combined” represent the results obtained from simultaneous fits of the untagged categories, dijet categories, and full set of categories, respectively. The black solid line shows $\mu = 1$, and the red dashed line shows the best fit value $\hat{\mu} = 2.4 \pm 0.9$ of all categories combined.	131
10.5	Upper limit (95% CL) on the signal strength (μ) relative to the SM prediction, as a function of the assumed value of the Higgs boson mass used in the fit.	132
10.6	Profile likelihood scans of $\mu_{\gamma\gamma}$ and $\mu_{Z\gamma}/\mu_{\gamma\gamma}$ for $m_H = 125.38 \text{ GeV}$.	132
A.1	Shower shape correction for the photon isolation.	144
A.2	Shower shape correction for the charged hadron isolation.	145

A.3	Shower shape correction for the charged hadron isolation with worst vertex.	145
A.4	Shower shape correction for the η width.	146
A.5	Shower shape correction for the ϕ width.	146
A.6	Shower shape correction for the variable R_9 .	147
A.7	Shower shape correction for the variable S_4 .	147
A.8	Shower shape correction for the variable $\sigma_{inj\eta}$.	148
A.9	Shower shape correction for the variable $\sigma_{inj\phi}$.	148
B.1	Fits to simulated $m_{\ell^+\ell^-\gamma}$ signal distributions in the electron channel for $m_H = 125$ GeV for the 2016 data-taking period. The top four plots correspond to the untagged categories, and the bottom three plots correspond to the dijet categories.	149
B.2	Fits to simulated $m_{\ell^+\ell^-\gamma}$ signal distributions in the muon channel for $m_H = 125$ GeV for the 2016 data-taking period. The top four plots correspond to the untagged categories, and the bottom three plots correspond to the dijet categories.	150
B.3	Fits to simulated $m_{\ell^+\ell^-\gamma}$ signal distributions in the electron channel for $m_H = 125$ GeV for the 2017 data-taking period. The top four plots correspond to the untagged categories, and the bottom three plots correspond to the dijet categories.	151
B.4	Fits to simulated $m_{\ell^+\ell^-\gamma}$ signal distributions in the muon channel for $m_H = 125$ GeV for the 2017 data-taking period. The top four plots	

	correspond to the untagged categories, and the bottom three plots correspond to the dijet categories.	152
B.5	Fits to simulated $m_{\ell^+\ell^-\gamma}$ signal distributions in the electron channel for $m_H = 125$ GeV for the 2018 data-taking period. The top four plots correspond to the untagged categories, and the bottom three plots correspond to the dijet categories.	153
B.6	Fits to simulated $m_{\ell^+\ell^-\gamma}$ signal distributions in the muon channel for $m_H = 125$ GeV for the 2018 data-taking period. The top four plots correspond to the untagged categories, and the bottom three plots correspond to the dijet categories.	154
B.7	Fits to simulated $m_{\ell^+\ell^-\gamma}$ signal distributions in the electron and muon channels combined in the lepton-tagged category for $m_H = 125$ GeV for the 2016 data-taking period. The left plot shows the fit to simulated ZH production events, and the right plot shows the fit to simulated WH production events.	155
B.8	Fits to simulated $m_{\ell^+\ell^-\gamma}$ signal distributions in the electron and muon channels combined in the lepton-tagged category for $m_H = 125$ GeV for the 2017 data-taking period. The left plot shows the fit to simulated ZH production events, and the right plot shows the fit to simulated WH production events.	155
B.9	Fits to simulated $m_{\ell^+\ell^-\gamma}$ signal distributions in the electron and muon channels combined in the lepton-tagged category for $m_H = 125$ GeV	

for the 2018 data-taking period. The left plot shows the fit to simulated ZH production events, and the right plot shows the fit to simulated WH production events.

155

- C.1 Fits to simulated $m_{\mu^+\mu^-\gamma}$ resonant background distributions from $H \rightarrow \mu^+\mu^-$ for $m_H = 125$ GeV for the 2016 data-taking period. The blue line shows the total fit function, the green line shows the Crystal Ball function component, and the red line shows the Gaussian function component. The top four plots correspond to the untagged categories, and the bottom three plots correspond to the dijet categories. 156
- C.2 Fits to simulated $m_{\ell^+\ell^-\gamma}$ resonant background distributions from $H \rightarrow \mu^+\mu^-$ in the electron and muon channels combined in the lepton-tagged category for $m_H = 125$ GeV for the 2016 data-taking period. The left plot shows the fit to simulated ZH production events, and the right plot shows the fit to simulated WH production events. The blue line shows the total fit function, the green line shows the Crystal Ball function component, and the red line shows the Gaussian function component. 157
- D.1 Observed nuisance parameter impacts on the signal strength in the $H \rightarrow Z\gamma$ search. 158
- D.2 Expected nuisance parameter impacts under the SM hypothesis on the signal strength in the $H \rightarrow Z\gamma$ search. 159
- D.2 Nuisance parameter impacts on $\mu_{Z\gamma}/\mu_{\gamma\gamma}$. 160

CHAPTER 1

Introduction

The standard model (SM) of particle physics is one of the most successful physics theories in history. It describes all of the fundamental particles we currently know in our universe, including the ways in which those particles interact with one another. Since its development in the second half of the twentieth century, the SM has been extensively tested through many measurements by numerous experiments. The Large Hadron Collider (LHC) was built with the goal of further testing the SM, while also searching for possible beyond the SM (BSM) physics at groundbreaking energy scales. One of the main goals of the LHC was to search for and observe the Higgs boson, a critical piece of the SM associated with the origin of particle mass. In 2012, the Compact Muon Solenoid (CMS) and A Toroidal LHC Apparatus (ATLAS) Collaborations announced its discovery.

Since the discovery of the Higgs boson [1, 2, 3], an extensive program of measurements [4] has been undertaken to determine its properties and couplings to different types of particles and to assess whether these properties are consistent with those predicted by the SM. With the successful running of the LHC, large data samples of proton-proton (pp) collisions at center of mass energy $\sqrt{s} = 13 \text{ TeV}$ have been accumulated, increasing the sensitivity to rare decays of the Higgs boson. Such decays also provide probes for possible contributions arising from BSM physics and include the process $H \rightarrow Z\gamma$ [5, 6, 7, 8, 9, 10, 11].

Figure 1.1 shows Feynman diagrams for the key SM contributions to the $H \rightarrow Z\gamma$ decay process. Experimentally, the final state resulting from $Z \rightarrow \ell^+\ell^-$ ($\ell = e$ or μ) is the most accessible, since the leptons are highly distinctive, well-measured, and provide a means to trigger the recording of the events. In the SM, the expected branching fraction for $H \rightarrow Z\gamma$ is $\mathcal{B}(H \rightarrow Z\gamma) = (1.57 \pm 0.09) \times 10^{-3}$, assuming a Higgs boson mass of $m_H = 125.38$ GeV. This branching fraction is comparable to $\mathcal{B}(H \rightarrow \gamma\gamma) = (2.27 \pm 0.04) \times 10^{-3}$ [12, 13]. The value $m_H = 125.38 \pm 0.14$ GeV is taken from the most recent CMS Higgs boson mass measurement [14], which uses the combination of $H \rightarrow \gamma\gamma$ and $H \rightarrow ZZ^* \rightarrow 4\ell$ results from the 2011–2012 and 2016 data samples. The ratio $\mathcal{B}(H \rightarrow Z\gamma)/\mathcal{B}(H \rightarrow \gamma\gamma) = 0.69 \pm 0.04$ is potentially sensitive to BSM physics, such as supersymmetry (SUSY) and extended Higgs sectors [15, 16, 17, 18]. The effects from these models can shift the $H \rightarrow Z\gamma$ and $H \rightarrow \gamma\gamma$ branching fractions by different amounts, making the ratio a sensitive observable. The impact on the ratio can be $\mathcal{O}(10\%)$, depending on the model. The $H \rightarrow Z\gamma$ branching fraction is sensitive to a potential anomalous trilinear Higgs self-coupling [10], and a

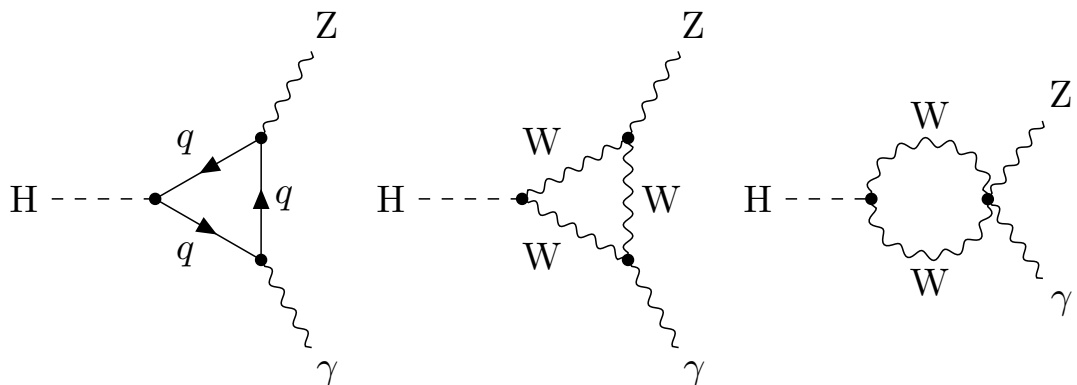


Figure 1.1. Feynman diagrams for $H \rightarrow Z\gamma$ decay.

precise measurement of the branching fraction could help to test the SM prediction for this fundamental quantity.

The ATLAS and CMS Collaborations have performed searches for the decay process $H \rightarrow Z\gamma \rightarrow \ell^+\ell^-\gamma$ [19, 20, 21, 22] at $\sqrt{s} = 7, 8$, and 13 TeV in the $e^+e^-\gamma$ and $\mu^+\mu^-\gamma$ final states. The most stringent bound has been set by the ATLAS Collaboration using $\sqrt{s} = 13$ TeV data corresponding to an integrated luminosity of 139 fb^{-1} . The observed (expected) upper limit at 95% confidence level (CL) on $\sigma(pp \rightarrow H)\mathcal{B}(H \rightarrow Z\gamma)$ relative to the SM is 3.6 (2.6), assuming $m_H = 125.09$ GeV. The region with lower dilepton invariant mass ($m_{\ell^+\ell^-}$) has also been explored. The ATLAS experiment has reported evidence for the decay $H \rightarrow \ell^+\ell^-\gamma$ with $m_{\ell^+\ell^-} < 30$ GeV using both dilepton channels [23]. The CMS Collaboration has also searched for the $H \rightarrow \ell^+\ell^-\gamma$ process with $m_{\ell^+\ell^-} < 50$ GeV in the dimuon channel at $\sqrt{s} = 8$ TeV [24] and 13 TeV [21].

This thesis describes a search for the decay $H \rightarrow Z\gamma$, where $Z \rightarrow \ell^+\ell^-$ for the dilepton invariant mass range $m_{\ell^+\ell^-} > 50$ GeV. This phase space is chosen in order to target on-shell Z bosons, since the region $m_{\ell^+\ell^-} < 50$ GeV contains a contribution from an additional process, $H \rightarrow \gamma^*\gamma \rightarrow \ell^+\ell^-\gamma$ [7]. The data sample corresponds to an integrated luminosity of 138 fb^{-1} of pp collisions at $\sqrt{s} = 13$ TeV accumulated between 2016 and 2018 by the CMS detector at the LHC. This thesis is organized as follows. The relevant theoretical physics background is provided in Chapter 2, and the CMS detector and event reconstruction are described in Chapter 3. Chapter 4 provides an overview of the $H \rightarrow Z\gamma$ search strategy, and the data and simulated event samples are described in Chapter 5. Chapter 6 outlines the object and event selection, and Chapter 7 discusses event categorization. The statistical procedure, including signal and background modeling, is

presented in Chapter 8, with systematic uncertainties discussed in Chapter 9. The final results of the search are discussed in Chapter 10, followed by a conclusion in Chapter 11.

CHAPTER 2

Theory

2.1. The Standard Model

The SM is currently our best theoretical framework for understanding the nature of fundamental particles. It is rooted in the idea that particles exist as excitations of quantum fields. These fields are constructed so as to obey fundamental symmetries of nature, and quantum field theory describes both the particles of our universe and their interactions. The SM is not only elegant and extensive, but provides a wide variety of measurable observables for the experimentalist to probe. So far, many measurements have been made of the known elementary particles and their interactions, and the predictions of the SM have held up in each case. In this respect, it is a wildly successful theory. In other respects, it is obviously incomplete. It does not account for the gravitational force, dark matter, or dark energy, among other phenomena. Thus, there is value in testing the SM even more carefully with experiments like those at the LHC, in hopes of refining our understanding and potentially discovering new physics.

2.2. The Elementary Particles

Figure 2.1 catalogs the elementary particles of the SM. These particles come in two broad types: fermions and bosons. Fermions are particles of half-integer spin that obey the Pauli exclusion principle. They are, therefore, responsible for the structure of matter. Each fermion has a corresponding antiparticle that has opposite electrical charge, but is

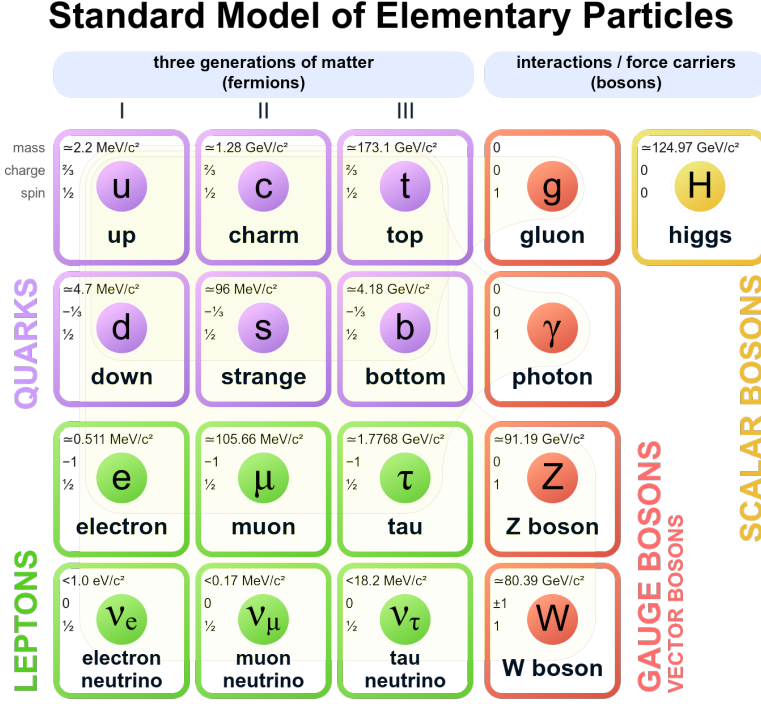


Figure 2.1. Table [25] of elementary particles in the SM. The leftmost three columns correspond to three generations of fermions, the fourth column from the left shows the gauge bosons which mediate the fundamental forces, and the rightmost column shows the Higgs boson. For each particle, mass, charge, and spin are labeled, with mass values given as of 2019.

otherwise identical. The fermions are subdivided into two types in three generations, the generations corresponding to mass. Quarks are fermions that carry both fractional electric charge and color charge, so they participate in the electroweak and strong interactions. Leptons are fermions that carry integer electric charge and participate in the electroweak interaction. In contrast to fermions, bosons have integer spin. The vector gauge bosons function as mediators of the fundamental forces of nature. The gluons mediate the strong force, the photon the electromagnetic force, and the W and Z bosons the weak force. Finally, the electrically neutral, scalar Higgs boson emerges due to electroweak symmetry

breaking, described later in this chapter. The interaction of the Higgs with the other particles in the SM is responsible for particle masses. In the context of this thesis, which is a search for $H \rightarrow Z\gamma$, the most relevant elementary particles are the Higgs boson, Z boson, leptons, and photon. Therefore, the remainder of this chapter will describe electroweak theory and the Higgs mechanism in more detail. Other aspects of the SM, such as quantum chromodynamics, are of importance in collider physics, but of less relevance for this specific search. Such topics are omitted in order to narrow the scope of the discussion.

2.3. Electroweak Theory

To motivate the Higgs mechanism and Higgs interactions, it is useful to first consider the electroweak interaction absent the Higgs. The electroweak piece of the SM Lagrangian can be written as

$$(2.1) \quad \mathcal{L}_{EW} = -\frac{1}{4}A_a^{\mu\nu}A_{\mu\nu}^a - \frac{1}{4}B^{\mu\nu}B_{\mu\nu} + i \sum_L \bar{L}\gamma^\mu D_{\mu,L}L + i \sum_R \bar{R}\gamma^\mu D_{\mu,R}R$$

$$(2.2) \quad A_{\mu\nu}^a = \partial_\mu A_\nu^a - \partial_\nu A_\mu + g\varepsilon_{abc}W_\mu^b W_\nu^c$$

$$(2.3) \quad B_{\mu\nu} = \partial_\mu B_\nu - \partial_\nu B_\mu$$

$$(2.4) \quad D_{\mu,L} = \partial_\mu + \frac{ig}{2}\tau \cdot A_\mu + \frac{ig'}{2}B_\mu Y$$

$$(2.5) \quad D_{\mu,R} = \partial_\mu + \frac{ig'}{2}B_\mu Y.$$

In the above equations, $A_{\mu\nu}^a$ represents an $SU(2)_L$ triplet of gauge fields and $B_{\mu\nu}$ represents a $U(1)$ gauge field. The third and fourth terms in equation 2.1 describe the interactions of these gauge fields with the fermions, both quarks and leptons. Note that the interaction

depends on the chirality of the fermions, where the left-handed fermions are denoted as L and the right-handed as R . The right-handed fermions interact only with the $U(1)$ field, while the left-handed fermions interact with the $U(1)$ and $SU(2)_L$ fields. This is encoded by the derivative operators $D_{\mu,L}$ and $D_{\mu,R}$ defined in equations 2.4 and 2.5 in terms of the fields, Pauli matrices (τ), hypercharge operator Y , and the couplings g and g' .

2.4. Spontaneous Symmetry Breaking (Higgs Mechanism)

One important property of the electroweak Lagrangian in equation 2.1 is that the bosons associated with the gauge fields are all massless. However, the direct observation of charged and neutral current interactions [26, 27] at CERN in 1973 implied that the W and Z boson must have relatively large masses in the range of 50–100 GeV. Indeed, the massive W and Z bosons were later discovered and measured [28, 29] at the CERN Super Proton Synchrotron in 1983. A solution to this shortcoming of the electroweak theory came in the form of the Higgs mechanism [30, 31, 32], which spontaneously breaks the $SU(2)_L \times U(1)$ gauge symmetry. One consequence of this is the addition of a real Higgs field accompanied by a massive Higgs boson. The W and Z boson masses arise naturally due to the electroweak symmetry breaking, while fermion masses are explained via additional Yukawa couplings to the Higgs boson. The discovery of the Higgs boson and subsequent measurements of its properties have provided experimental verification that the Higgs mechanism is a central piece of the SM.

To understand how the Higgs mechanism works, consider the introduction of a complex scalar field Φ , which transforms as a doublet under $SU(2)_L$.

$$(2.6) \quad \Phi = \begin{bmatrix} \phi^+ \\ \phi^0 \end{bmatrix}$$

Its contribution to the Lagrangian is given by:

$$(2.7) \quad \mathcal{L}_H = (D_L^\mu \Phi)^\dagger (D_{\mu,L} \Phi) - V(\Phi),$$

where the Higgs potential takes the form

$$(2.8) \quad V(\Phi) = \mu^2 |\Phi^\dagger \Phi| + \lambda \left(|\Phi^\dagger \Phi| \right)^2.$$

Consider the case in which the parameters of the Higgs potential λ and μ satisfy the conditions $\lambda > 0$ and $\mu^2 < 0$. Then the shape of the potential is shown in Fig. 2.2 (right). There is no minimum of the potential at $\Phi = 0$. Rather, an infinite set of minima lie around a circle in the complex plane. Hence, it is said that Φ has a nonzero vacuum expectation value (VEV). The value of the VEV in terms of μ and λ can be determined by explicitly minimizing the potential:

$$(2.9) \quad \begin{aligned} \frac{\partial}{\partial(\Phi^\dagger \Phi)} V(\Phi) &= 0 \\ \mu^2 + 2\lambda \left(|\Phi^\dagger \Phi| \right) &= 0 \\ \mu^2 + 2\lambda \left[(\phi^+)^2 + (\phi^0)^2 \right] &= 0. \end{aligned}$$

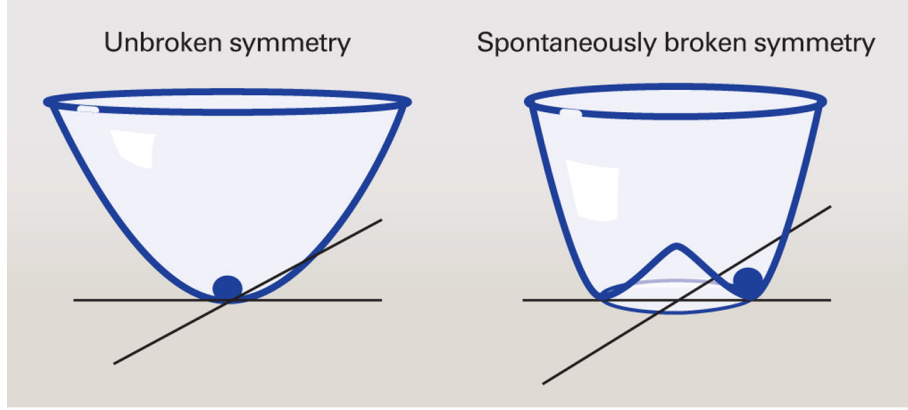


Figure 2.2. Comparison of the shapes of complex scalar potentials without symmetry breaking (left) and with spontaneous symmetry breaking (right) [33]. The transverse axes represent the real-imaginary Φ plane, and the vertical axis represents the magnitude of the potential $V(\Phi)$. The diagram at right corresponds to the shape of the Higgs potential in the SM.

This can be minimized in many ways depending on individual values of ϕ^+ and ϕ^0 in the vacuum. By convention, and without loss of generality, we choose the case in which $\phi^+ = 0$. In this case, we obtain the equation

$$(2.10) \quad \phi^0 = \sqrt{\frac{-\mu^2}{2\lambda}} = \frac{1}{\sqrt{2}}v,$$

where we have defined $v \equiv \sqrt{-\mu^2/\lambda}$.

The existence of the Higgs VEV has profound implications. To see this, it is helpful to reparameterize the scalar doublet field Φ as follows:

$$(2.11) \quad \Phi = \frac{1}{\sqrt{2}}e^{i\frac{\tau^a}{2}\theta_a(x)} \begin{bmatrix} 0 \\ v + h(x) \end{bmatrix}.$$

As Φ is invariant under local $SU(2)_L$ gauge transformations, the prefactor may be rotated away. This is equivalent to setting $\theta(x) = 0$ in equation 2.11. This choice of gauge is

known as the unitary gauge, and leads to

$$(2.12) \quad \Phi = \frac{1}{\sqrt{2}} \begin{bmatrix} 0 \\ v + h(x) \end{bmatrix}.$$

Given the above form of Φ , we can now evaluate the Higgs Lagrangian (equation 2.7), starting with the kinetic term $(D_L^\mu \Phi)^\dagger (D_{\mu,L} \Phi)$.

$$\begin{aligned} (D_L^\mu \Phi)^\dagger (D_{\mu,L} \Phi) &= \left| \left(\partial_\mu - \frac{ig}{2} \tau \cdot A_\mu - \frac{ig'}{2} B_\mu Y \right) \Phi \right|^2 \\ &= \frac{1}{2} \left| \begin{bmatrix} \partial_\mu - \frac{i}{2}(gA_\mu^3 + g'B_\mu) & -\frac{ig}{2}(A_\mu^1 - iA_\mu^2) \\ -\frac{ig}{2}(A_\mu^1 + iA_\mu^2) & \partial_\mu + \frac{i}{2}(gA_\mu^3 - g'B_\mu) \end{bmatrix} \begin{bmatrix} 0 \\ v + h(x) \end{bmatrix} \right|^2 \\ &= \frac{1}{2} \left| \begin{bmatrix} -\frac{ig}{2}(A_\mu^1 - iA_\mu^2)(v + h(x)) \\ \partial_\mu h(x) + \frac{i}{2}(gA_\mu^3 - g'B_\mu)(v + h(x)) \end{bmatrix} \right|^2 \\ &= \frac{1}{2} \partial_\mu h(x) \partial^\mu h(x) + \frac{1}{8} (gA_\mu^3 - g'B_\mu)(gA_\mu^\mu - g'B^\mu)(v + h(x))^2 \\ &\quad + \frac{g^2}{8} (A_\mu^1 - iA_\mu^2)(A_\mu^1 + iA_\mu^2)(v + h(x))^2 \end{aligned} \tag{2.13}$$

With some foreknowledge of the result, we define the physical gauge fields and their masses.

$$(2.14) \quad W_\mu^\pm = \frac{1}{\sqrt{2}} (A_\mu^1 \mp iA_\mu^2) \quad m_W = \frac{gv}{2}$$

$$(2.15) \quad Z_\mu = \frac{1}{\sqrt{g^2 + g'^2}} (gA_\mu^3 - g'B_\mu) \quad m_Z = \sqrt{g^2 + g'^2} \frac{v}{2}$$

$$(2.16) \quad A_\mu = \frac{1}{\sqrt{g^2 + g'^2}} (g'A_\mu^3 + gB_\mu) \quad m_A = 0$$

Then the kinetic term of the Higgs Lagrangian can be recast as

$$\begin{aligned}
 (D_L^\mu \Phi)^\dagger (D_{\mu,L} \Phi) = & \frac{1}{2} \partial_\mu h(x) \partial^\mu h(x) \\
 & + \frac{1}{2} m_Z^2 Z_\mu Z^\mu + m_W^2 W_\mu^+ W^{-\mu} \\
 & + \frac{v}{4} (g^2 + g'^2) Z_\mu Z^\mu h + \frac{1}{8} (g^2 + g'^2) Z_\mu Z^\mu h^2 \\
 (2.17) \quad & + \frac{v}{4} g^2 W_\mu^+ W^{-\mu} h + \frac{1}{8} g^2 W_\mu^+ W^{-\mu} h^2.
 \end{aligned}$$

Equation 2.17 provides a great deal of information on the physical ramifications of the Higgs mechanism. The first term is the kinetic term of the physical Higgs boson field. The second and third terms are the mass terms of the Z and W bosons, respectively. The fourth and fifth terms show the linear and quadratic couplings of the Z boson to the Higgs boson, respectively. Finally, the sixth and seventh terms show the linear and quadratic couplings of the W boson to the Higgs boson, respectively. Given the form of equation 2.12, a similar expansion can be carried out on the Higgs potential (equation 2.8). Here, the terms involving the physical Higgs boson are most interesting, so constant terms are dropped.

$$\begin{aligned}
 V(\Phi) = & \frac{\mu^2}{2} (v + h)^2 + \frac{\lambda}{4} ((v + h)^2)^2 \\
 (2.18) \quad & \rightarrow \lambda v^2 h^2 + \lambda v h^3 + \frac{\lambda}{4} h^4
 \end{aligned}$$

The first term is a Higgs mass term, with $m_H = \sqrt{2\lambda v^2}$. The second and third terms describe the Higgs trilinear and quartic self-couplings, respectively.

The Lagrangian including the Higgs doublet Φ can be further extended to incorporate interactions between the Higgs and fermion fields. These interactions, along with the nonzero Higgs VEV, provide a mechanism to generate the fermion masses. The interactions take the form of Yukawa couplings:

$$(2.19) \quad \mathcal{L}_{Yukawa} = Y_{ij}^d \bar{Q}_L^i \Phi d_R^j + Y_{ij}^u \bar{Q}_L^i \tilde{\Phi} u_R^j + Y_{ij}^e \bar{L}_L^i \Phi e_R^j + h.c.,$$

where $\tilde{\Phi} \equiv i\tau_2 \Phi^*$, and u , d , and e represent up-type quarks, down-type quarks, and leptons, respectively. The constants Y_{ij}^a denote the Yukawa couplings in each case, Q^i is the set of $SU(2)_L$ quark doublets, and L^i is the set of $SU(2)_L$ lepton doublets. Plugging in the unitary gauge parameterization of equation 2.12, this evaluates to

$$(2.20) \quad \mathcal{L}_{Yukawa} = \frac{Y_{ij}^d}{\sqrt{2}} \bar{d}_L^i (v + h) d_R^j + \frac{Y_{ij}^u}{\sqrt{2}} \bar{u}_L^i (v + h) u_R^j + \frac{Y_{ij}^e}{\sqrt{2}} \bar{e}_L^i (v + h) e_R^j$$

It is worth looking closely at the terms in equation 2.20. For a given fermion type, the first term in the parentheses is a fermion mass term. The second term in the parentheses gives the coupling of the fermion to the Higgs boson. With this in mind, we observe that the fermion mass is given in terms of the couplings and the Higgs vev by

$$(2.21) \quad m_f = \frac{y_f v}{\sqrt{2}},$$

where y_f is the relevant value taken from the Yukawa coupling matrix. In addition, we see that the strength of the fermion coupling to the Higgs boson is given by $\frac{m_f}{v}$. Thus, fermions couple to the Higgs boson with strengths directly proportional to their masses. This result has important consequences in the context of collider experiments,

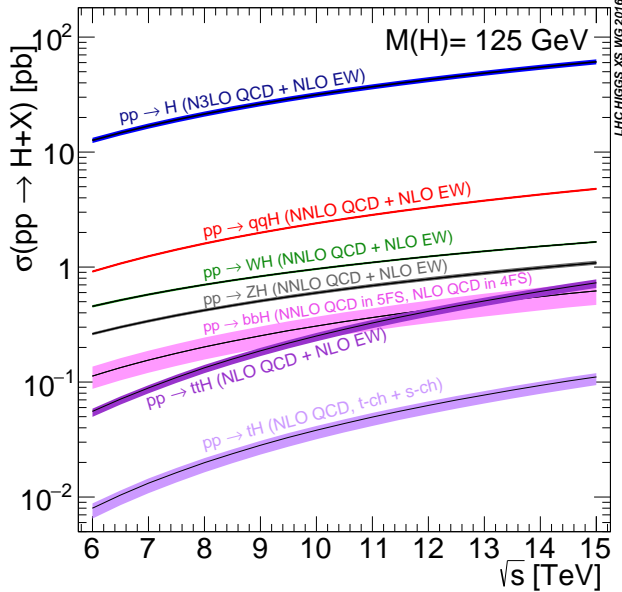


Figure 2.3. Cross sections for different Higgs boson production mechanisms as a function of center of mass energy for $m_H = 125 \text{ GeV}$ [12].

as it regulates the rates of Higgs production and decay related to each fermion-Higgs interaction.

2.5. Higgs Production

At a hadron collider like the LHC, the Higgs boson can be produced via several different mechanisms, with each mechanism occurring at a certain rate. The dominant production mechanism is gluon-gluon fusion (ggH), followed by vector boson fusion (VBF) production, which is about an order of magnitude rarer. Less common production mechanisms, but still relevant for a search at the LHC, are the associated production mechanisms WH , ZH , and $t\bar{t}H$. The cross sections for each Higgs production mechanism as a function of center of mass energy are shown in Fig. 2.3.

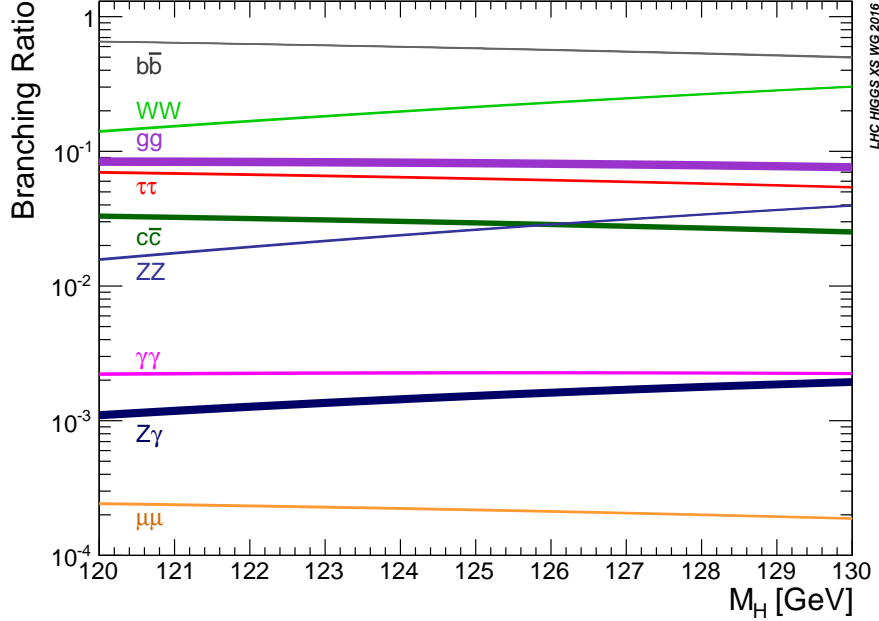


Figure 2.4. Branching fractions for different Higgs decay modes as a function of m_H [12].

2.6. Higgs Decay

The Higgs boson decays rapidly after it is produced at the LHC. It can decay into a variety of final states, each occurring at a certain rate. Tree-level Higgs decays occur at rates proportional to the square of the mass of the decay products. Decays to $b\bar{b}$, W^+W^- , $\tau^+\tau^-$, and ZZ^* are among the most common and experimentally accessible at the LHC. Other Higgs decays occur at loop-level, including $H \rightarrow \gamma\gamma$ and $H \rightarrow Z\gamma$. Figure 2.4 shows the branching fractions at $\sqrt{s} = 13$ TeV for different decay modes as a function of Higgs boson mass. The branching fraction of $H \rightarrow Z\gamma$ is suppressed relative to several other production modes, so a search for $H \rightarrow Z\gamma$ must rely on the clean $\ell^+\ell^-\gamma$ signature.

2.7. Physics Beyond the Standard Model

One of the goals of the LHC is to search for BSM physics. While the decay $H \rightarrow Z\gamma$ is predicted in the SM, searching for it and measuring its branching fraction can indirectly probe potential new physics phenomena. A few unique features of $H \rightarrow Z\gamma$ make it well-suited as a BSM probe. First, the decay is loop-induced, which means that the introduction of new particles will contribute to the loop, interfering and altering the final branching fraction. Secondly, the decay $H \rightarrow \gamma\gamma$ is a very similar loop-induced process. This means any new particle content entering into the $H \rightarrow Z\gamma$ loop will also enter into the $H \rightarrow \gamma\gamma$ loop. However, in the case of $H \rightarrow Z\gamma$, the Z boson couples to loop particles according to the $SU(2)_L \times U(1)$ quantum number rather than just the electric charge, as is the case for $H \rightarrow \gamma\gamma$. It follows that potential BSM physics scenarios can shift the branching fractions of $H \rightarrow Z\gamma$ and $H \rightarrow \gamma\gamma$ by differing amounts, making the ratio $\mathcal{B}(H \rightarrow Z\gamma)/\mathcal{B}(H \rightarrow \gamma\gamma)$ a sensitive observable. In the SM, $\mathcal{B}(H \rightarrow Z\gamma)/\mathcal{B}(H \rightarrow \gamma\gamma) = 0.69 \pm 0.04$. A measurement of a significant deviation from this value would be an indicator of possible BSM physics. Below, we describe a few examples of BSM scenarios that can affect this ratio.

One way to consider BSM effects in the context of $H \rightarrow Z\gamma$ is to introduce new particles, like a W' boson, charged scalar, or a pair of charged leptons. This is the approach taken by Carena, Low, and Wagner [16]. The W' possibility is motivated by the fact that the W boson loop is the dominant contribution in the SM. The W' can be defined by an $SU(2)_L$ triplet and characterized by mass and Higgs coupling parameters. Figure 2.5 (left) shows contours of constant branching fraction enhancement in the $H \rightarrow Z\gamma$ and $H \rightarrow \gamma\gamma$ decay channels in the mass-coupling plane for the W' model. Depending on

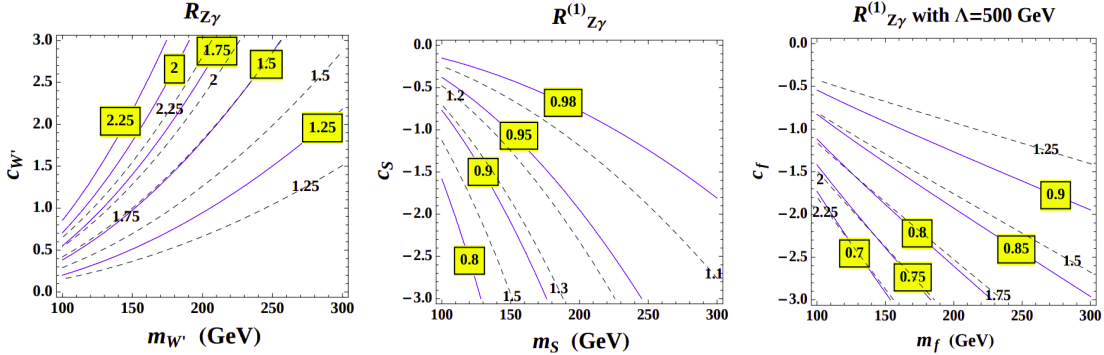


Figure 2.5. Contours of constant branching fraction enhancement relative to the SM for the W' (left), charged scalar (center), and charged lepton (right) scenarios [16]. The solid lines represent contours of enhancement in $\mathcal{B}(H \rightarrow Z\gamma)$, while the dashed lines correspond to $H \rightarrow \gamma\gamma$. The yellow boxed numbers label the enhancement for each $H \rightarrow Z\gamma$ contour, and the unboxed numbers label the enhancement for each $H \rightarrow \gamma\gamma$ contour.

the parameter values, the level of enhancement can be up to double the SM value, and it differs significantly in the two channels. Similarly, we can imagine a new charged scalar or a pair of new charged leptons. The branching fraction enhancement contour plots in Fig. 2.5 show that for similar regions in the mass-coupling plane, $H \rightarrow Z\gamma$ can be enhanced, while $H \rightarrow \gamma\gamma$ is simultaneously diminished.

Other relevant BSM physics models include extended Higgs sectors. Such models often contain charged Higgs bosons, which enter into the $H \rightarrow Z\gamma$ and $H \rightarrow \gamma\gamma$ loops and impact the branching fractions. In Ref. [17], Chiang and Yagyu catalog extended Higgs models of varying types: models with one singly-charged boson, those with one singly-charged and one doubly-charged boson, and those with two singly-charged bosons. In total, the authors consider thirteen models, including the two Higgs doublet model, the minimal SUSY model, and the Higgs triplet model. Figure 2.6 gives the ratio of decay widths $\Gamma(H \rightarrow Z\gamma)/\Gamma(H \rightarrow \gamma\gamma)$ as a function of the mass coefficient of the additional

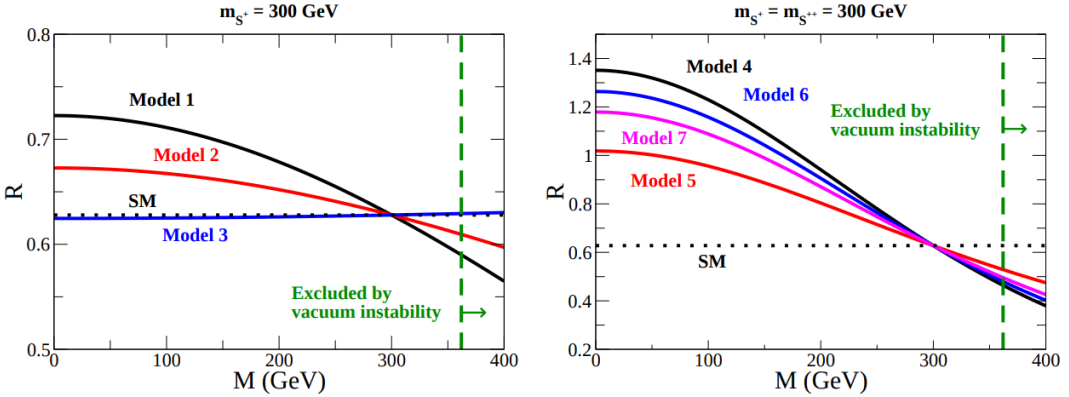


Figure 2.6. Ratio of decay widths $\Gamma(H \rightarrow Z\gamma)/\Gamma(H \rightarrow \gamma\gamma)$ as a function of the mass coefficient of the additional scalar field(s) for seven BSM models with extended Higgs sectors [17]. The models plotted on the left correspond to one additional singly-charged boson, and those on the right to one additional singly-charged and one additional doubly-charged boson.

scalar field(s) for seven of the models. For mass scales accessible at the LHC, the ratio can be significantly shifted relative to the SM prediction.

Another approach, discussed by Degrassi and Vitti in Ref. [10], is to consider how an anomalous Higgs trilinear self-coupling would modify the $H \rightarrow Z\gamma$ branching fraction. In the SM, the value of λ in equation 2.18 is the same for each of the three terms. However, one can consider a case in which the value of the trilinear term is different than the value in the SM. This would enter into amplitudes for two-loop processes, such as those shown in Fig. 2.7. In turn, this would modify the $H \rightarrow Z\gamma$ branching fraction relative to the SM prediction. An advantage of this approach is that it does not depend on the specifics of the BSM model giving rise to the anomalous trilinear Higgs self-coupling, so it can serve as a more general probe for new physics. Degrassi and Vitti show that $H \rightarrow Z\gamma$ is among the most sensitive Higgs decay modes to an anomalous trilinear Higgs self-coupling, more sensitive than $H \rightarrow \gamma\gamma$ and only slightly less sensitive than $H \rightarrow ZZ$.

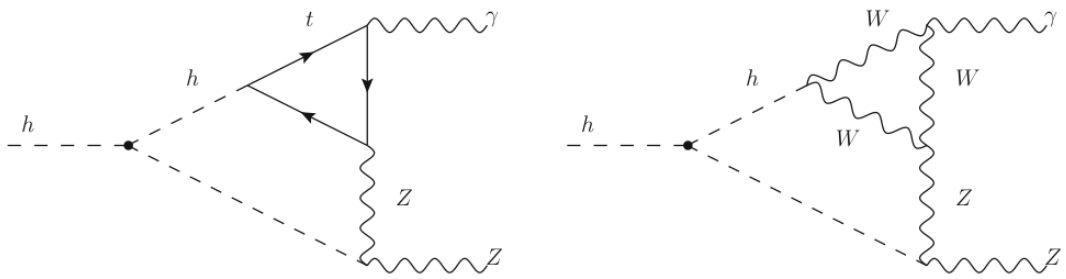


Figure 2.7. Examples of two-loop diagrams [10] contributing to $H \rightarrow Z\gamma$ decay. The presence of the three-Higgs vertex makes these diagrams sensitive to an anomalous trilinear Higgs self-coupling.

CHAPTER 3

Experiment Description

3.1. The Large Hadron Collider

The Large Hadron Collider (LHC) [34] is a high energy pp collider that serves several modern particle physics detector experiments. Built at CERN, straddling the French-Swiss border, and turned on for operation in 2008, it is the most powerful particle collider in history. The LHC was designed to collide protons at a maximum center of mass energy of $\sqrt{s} = 14 \text{ TeV}$ with a maximum instantaneous luminosity of $10^{34} \text{ cm}^{-2}\text{s}^{-1}$. To achieve this performance, the 27 km tunnel originally constructed for the Large Electron-Positron Collider (LEP) [35] was repurposed to separately accelerate two counterrotating proton beams. The separate acceleration of the beams is made possible by oppositely oriented magnetic dipole fields in the two rings. When the beams achieve the desired energy, they are collided at one of four interaction points.

The protons collided in the LHC are first gathered, bunched, and accelerated in other parts of the CERN accelerator complex before injection into the LHC ring. A detailed description of the injection chain can be found in Ref. [36], and a short summary is provided below. First, protons are stripped off of hydrogen atoms by a duoplasmatron and accelerated to 50 MeV by a linear accelerator (LINAC). Next, the protons are further accelerated in a series of synchrotron rings of increasing size, the Proton Synchrotron Booster (PSB), Proton Synchrotron (PS), and Super Proton Synchrotron (SPS). The SPS brings

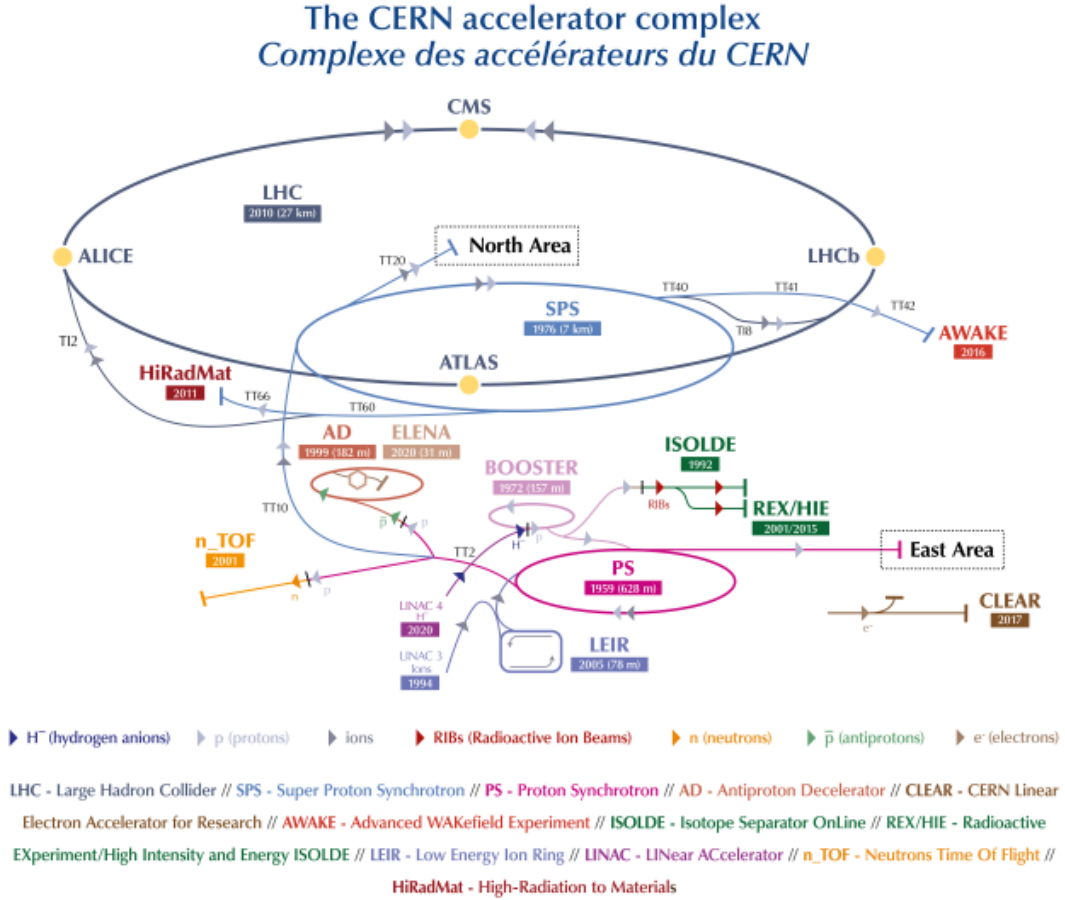


Figure 3.1. CERN accelerator complex [37].

the proton beam energy up to 450 GeV. At this point, the beam is injected to the two LHC rings to be accelerated up to the final collision energy. Acceleration in the main ring is achieved by a system of thousands of superconducting dipole magnets, along with hundreds of correcting quadrupole magnets. A liquid helium cooling system is used to maintain the magnets at cryogenic temperatures. A full diagram of the CERN accelerator complex [37], including the parts relevant for the LHC, is shown in Fig. 3.1.

3.2. The Compact Muon Solenoid

The CMS apparatus [38] is a multipurpose, nearly hermetic detector, designed to trigger on [39, 40] and identify photons, electrons, muons, and (charged and neutral) hadrons [41, 42, 43, 44]. The central feature of the CMS apparatus is a superconducting solenoid of 6 m internal diameter, providing a magnetic field of 3.8 T. Within the solenoid volume are a silicon pixel and strip tracker, a lead tungstate crystal electromagnetic calorimeter (ECAL), and a brass and scintillator hadron calorimeter (HCAL), each composed of a barrel and two endcap sections. The ECAL consists of 75,848 lead tungstate crystals, which provide coverage in pseudorapidity $|\eta| < 1.48$ in a barrel region (EB) and $1.48 < |\eta| < 3.0$ in two endcap regions (EE). Preshower detectors consisting of two planes of silicon sensors interleaved with a total of 3 radiation lengths of lead are located in front of each EE detector. Forward calorimeters extend the pseudorapidity coverage provided by the barrel and endcap detectors. Muons are measured in gas-ionization detectors embedded in the steel flux-return yoke outside the solenoid. Figure 3.2 shows a schematic diagram of the CMS detector, and a more detailed description of the individual detector components and detector operation is provided below.

3.2.1. Superconducting Magnet

The function of the superconducting magnet within the CMS detector is to bend the trajectories of charged particles. This is crucial for accurate particle identification and momentum measurement. Designed to provide a maximum magnetic field of 4 T, its operating strength during pp collision runs is set to 3.8 T. The bulk of the magnet is composed of NbTi, cooled by liquid helium to 4.5 K, which is below the critical temperature

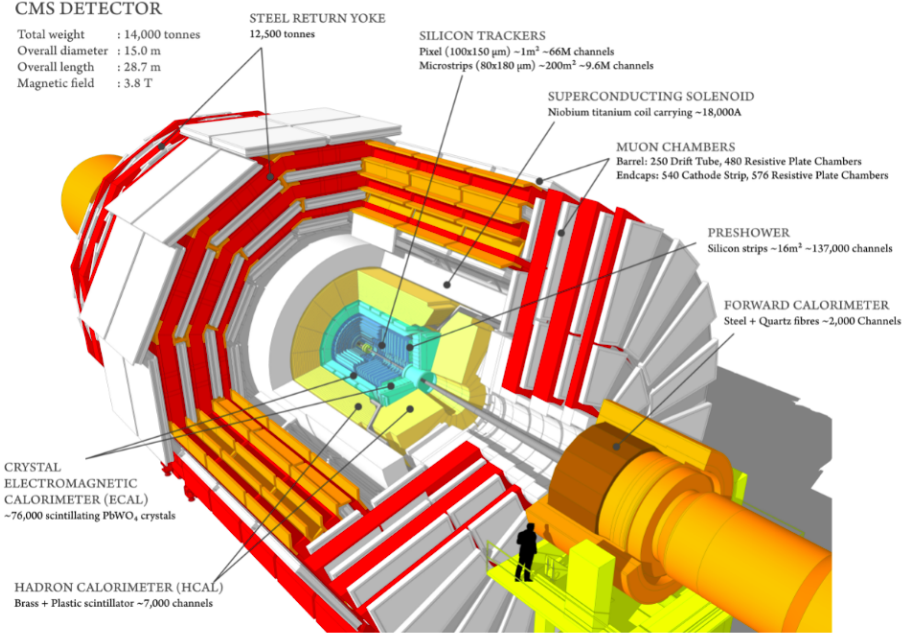


Figure 3.2. CMS detector apparatus. [45]

for superconductivity. The magnet has a length of 12.5m, diameter of 6.3m, and mass of 220 tons. The solenoid encloses several detector components, including the tracker and the majority of the calorimeters. A steel flux-return yoke is built around the solenoid, and is composed of 5 wheels and two endcaps weighing a total of roughly 10,000 tons.

3.2.2. Inner Tracking System

The inner tracking system is designed to reconstruct charged particle trajectories and vertices arising from particle decays. Comprised of a silicon pixel detector and silicon strip tracker, it covers the pseudorapidity region $|\eta| < 2.5$ and is designed for efficient and precise measurement of charged particles with transverse momentum (p_T) above about 1 GeV. At the LHC design luminosity for pp collisions, each bunch crossing leads to about

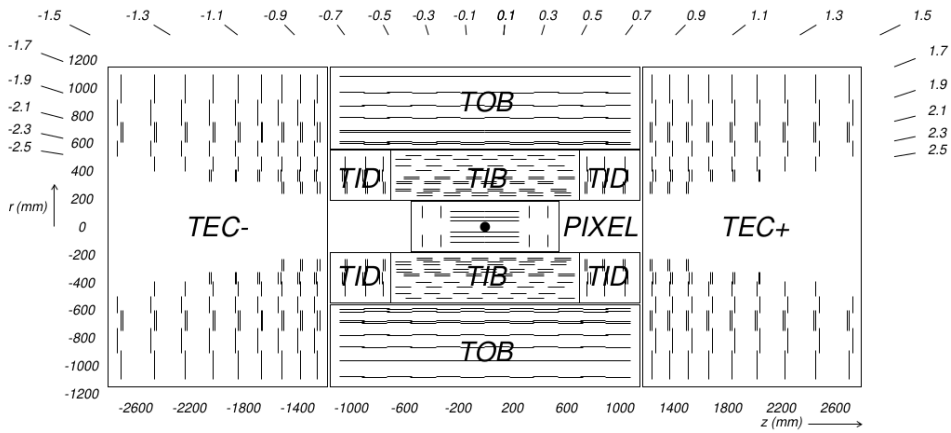


Figure 3.3. Cross section of the CMS inner tracking system in the r-z plane. [38]

1,000 hits in the inner tracking system. As such, the inner tracking system was designed to be maximally radiation tolerant.

The silicon pixel detector covers the inner region of $r < 10\text{ cm}$. It is composed of $100 \times 150 \mu\text{m}^2$ pixels, arranged in three barrel layers and two endcap disks. Due to the extreme radiation environment, the innermost layer was designed to be replaced after about two years of LHC operation. In response to LHC running conditions and detector degradation, a replacement and upgrade of the full pixel detector was made during the LHC extended year-end technical stop in 2016–2017.

The silicon strip tracker covers the region $20 < r < 116\text{ cm}$. It is divided into three subsystems: the Tracker Inner Barrel (TIB), Tracker Inner Disks (TID), and Tracker Outer Barrel (TOB). The strip thickness is $320 \mu\text{m}$ ($500 \mu\text{m}$) in the TIB/TID (TOB). A schematic diagram of the CMS inner tracking system in the r-z plane is shown in Fig. 3.3.

3.2.3. Electromagnetic Calorimeter (ECAL)

The electromagnetic calorimeter (ECAL) is designed to identify and measure electromagnetic particles by inducing and characterizing electromagnetic showers. It is made up of 61,200 lead tungstate (PbWO_4) crystals in the barrel (EB), which covers $|\eta| < 1.479$, plus 7,324 crystals in each endcap (EE), which cover the range $1.479 < |\eta| < 3.0$. A preshower system lies in front of the EE. The preshower is a lead and silicon sampling calorimeter designed to aid in the identification of neutral pions and to improve the spatial resolution in the endcap region. The crystal length corresponds to 25.8 (24.7) radiation lengths in the EB (EE). When electromagnetic particles, such as electrons and photons, encounter the ECAL and interact with the crystal material, electromagnetic showers are induced. Light is emitted by the ECAL crystals proportional to the energy of constituent particles in the shower, allowing for reconstruction of the shower energy. An array of fast and radiation-tolerant photodetectors detects the emitted light, and this information is saved off detector. As shown in Fig. 3.4, the ECAL has maintained good performance with minimal degradation throughout the duration of Run 1 and Run 2 of the LHC.

3.2.4. Hadronic Calorimeter (HCAL)

Measurements of hadrons, jets, and missing transverse momentum are crucial at a hadron collider like the LHC. The CMS hadronic calorimeter (HCAL) is instrumental in such measurements. The HCAL is primarily a sampling calorimeter broken into several sub-detectors. The barrel (HB) covers the range $|\eta| < 1.3$, the endcaps (HE) cover the range $1.3 < |\eta| < 3$, the forward calorimeter (HF) covers the range $3 < |\eta| < 5$, and an outer barrel calorimeter (HO) covers $|\eta| < 1.3$ outside of the solenoid magnet.

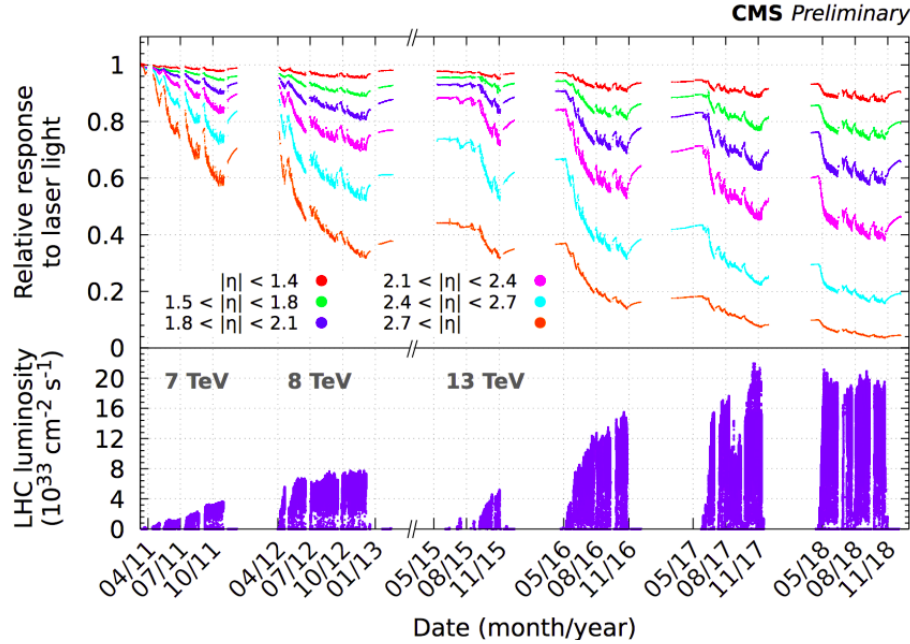


Figure 3.4. Response of the CMS ECAL crystals to injected laser light as a function of time, broken into regions of $|\eta|$ [46].

Layers of brass absorber are interleaved with plastic scintillator in the HB and HE, with a total absorber thickness of 5.82–10.6 interaction lengths in the HB and about 10 interaction lengths in the HE. Scintillation light emitted by the active material is measured and transmitted off detector using hybrid photodiodes. The design of the HF was motivated by the extreme particle fluxes in the very forward region. The HF is made up of steel plate absorbers, in which quartz fibers are inserted to serve as the active material. Cherenkov light is produced when shower particles moving at speeds above the Cherenkov threshold pass through the fibers, and a calculable fraction of the light is captured by the fibers. The function of the HO is to recover the energy in showers that leak through the HB, which is needed for the accurate measurement of missing transverse momentum. In the HO, the solenoid coil, itself, as well as a thick iron tail catcher,

function as absorbers. This extends the effective HCAL depth to 11.8 interaction lengths everywhere except at the barrel-endcap boundary.

3.2.5. Muon Detectors

The CMS muon detector system is comprised of a set of gas ionization detectors embedded in the flux-return yoke outside the solenoid magnet. These detectors cover the range $|\eta| < 2.4$. The positioning of the muon detectors outside the magnet takes advantage of the fact that muons deposit minimal energy in the detector materials within the solenoid, such as the calorimeters. Most other types of particles will have deposited their energy before reaching the muon system, so using the combination of muon detector and tracker information, CMS is able to reconstruct muons with good momentum resolution. The gas ionization detectors in the muon system come in three types: drift tubes (DTs), cathode strip chambers (CSCs), and resistive plate chambers (RPCs). The DTs cover the barrel region ($|\eta| < 1.2$) and are arranged in four stations, each with 60–70 drift chambers containing a gas mixture of 85% Ar and 15% CO₂. The CSCs are multiwire proportional chambers composed of anode wire planes interleaved with cathode panels. Muons passing through the CSCs ionize a gas mixture of 40% Ar, 50% CO₂, and 10% CF₄, and the electrons flow to the anodes, yielding a detectable avalanche of charge. Covering the region $|\eta| < 2.1$, the RPCs are composed of oppositely charged parallel plates enclosing a gas mixture of primarily C₂H₂F₄. One advantage of the RPCs is their good time resolution, which is less than the LHC bunch spacing time of 25 ns. This makes them useful for fast muon triggering that matches muon tracks to the relevant

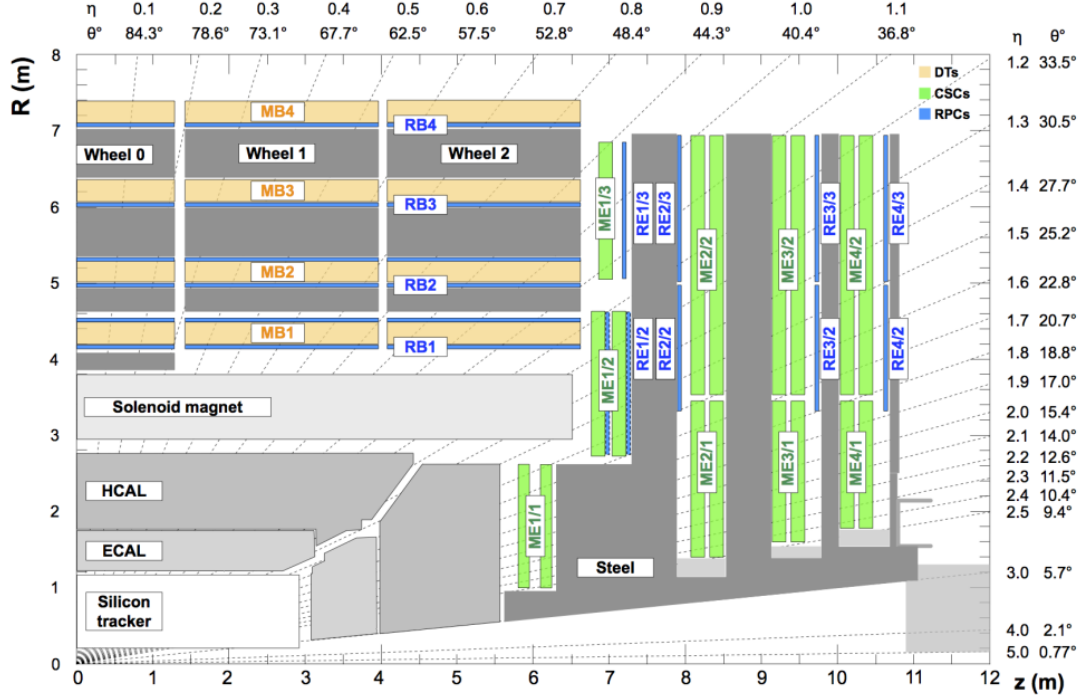


Figure 3.5. Diagram of the CMS detector in the r - z plane showing the components of the muon system [38].

bunch crossing. Figure 3.5 shows a cross-sectional view of the CMS detector highlighting the muon system components.

3.3. Trigger System

At the LHC, the proton beam crossing interval is 25 ns, which corresponds to a pp collision rate of 40 MHz. Recording the full set of detector information for each collision is unfeasible, as there is far too much data to save to disk. Because of this, the CMS experiment employs a two-tiered trigger system, designed to preserve information of physics interest while reducing the stored event rate to a more manageable 100 Hz. The first level of the trigger (L1) is a hardware trigger, which reduces the event rate from

40 MHz to about 100 kHz. The second layer is the high level trigger (HLT), a processor farm using software optimized for fast processing.

The L1 trigger is implemented using field-programmable gate arrays and application-specific integrated circuits, and has local, regional, and global components. First, local patterns in the calorimeters, track segments, and hit patterns in the muon chambers are processed by the Trigger Primitive Generators (TPGs). The TPGs rank and sort primitive objects corresponding to particle candidates based on energy, momentum, and reconstruction quality. Information from the TPGs is taken as input by regional triggers for the calorimeters and muon systems. These regional triggers further determine candidate physics objects, as well as energy sums and isolation information. Finally, this information is fed to a set of global triggers, which rank trigger objects across the entire detector. The final global trigger must decide whether to accept or reject an event based on information input from the global calorimeter and muon trigger systems. Algorithms used for this decision can be based on single object p_T thresholds and multiplicity-related requirements, such as the presence of multiple jets, among other criteria. Events passing the L1 trigger are read out and passed to the HLT for further processing.

In contrast to the L1 trigger, the HLT incorporates the full physics object reconstruction based on the full precision of the detector. This allows the HLT to accept and reject events with algorithms of similar quality to those used by offline analyses. Over 13,000 central processing unit cores are dedicated to HLT processing. For speed and efficiency, reconstruction and filtering algorithms are applied in increasing order of complexity. If a filter sequence fails, the rest of the reconstruction is skipped. Additionally, processing is done regionally based on the L1 candidates and relevant detector components passed as

input to the HLT. Events that pass the HLT are assigned to relevant data streams based on their physics content. For the $H \rightarrow Z\gamma$ search, the relevant streams are the Double Muon and Double Electron streams, triggered by events with two muons or two electrons passing a set of minimum p_T requirements and other cuts.

3.4. Object Reconstruction

The global event reconstruction (also called particle-flow (PF) event reconstruction [47]) aims to reconstruct and identify each individual particle in an event, with an optimized combination of all subdetector information. In this process, the identification of the particle type (photon, electron, muon, charged hadron, neutral hadron) plays an important role in the determination of the particle direction and energy. Figure 3.6 provides a simple visualization of how each type of particle types interacts with each of the CMS subdetectors. An overview of the reconstruction procedure for each particle type is provided below.

3.4.1. Photon and Electron Reconstruction

Photons and electrons interact with the material in the ECAL, depositing the majority of their energy before reaching the HCAL. As they interact, photons convert into electron-positron pairs and electrons radiate bremsstrahlung photons. This leads to the formation of an electromagnetic shower. Because of this, the original particle energy is split into multiple energy deposits, which must be combined to reconstruct the original energy. Deposits in individual ECAL crystals are combined into clusters, and these clusters are in turn combined into superclusters. Two algorithms are used to define superclusters: the

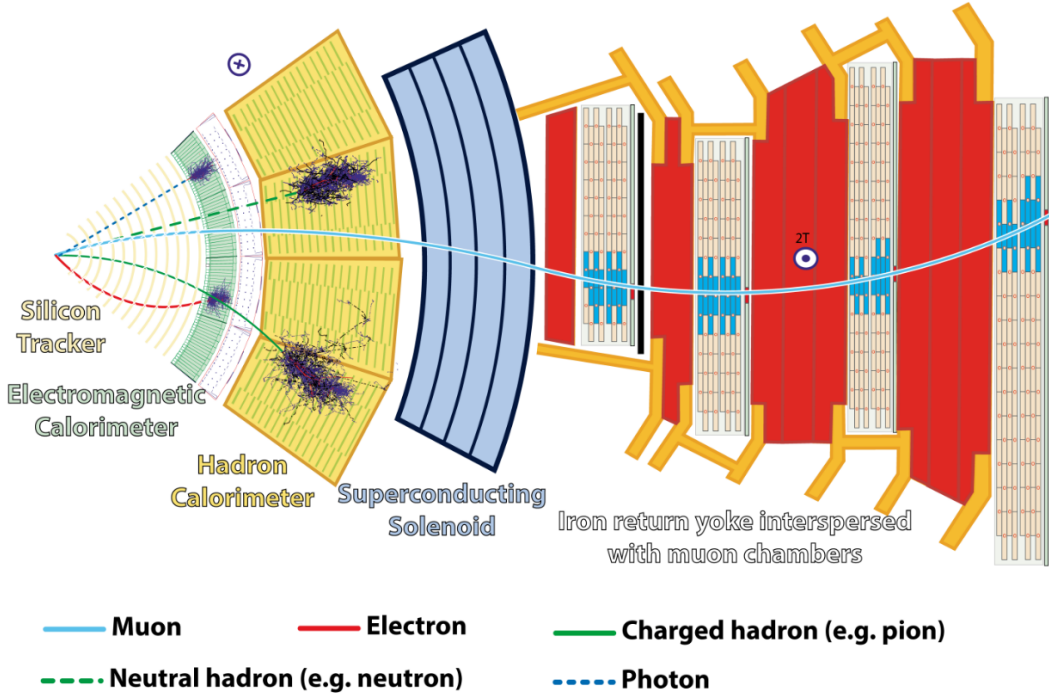


Figure 3.6. Visualization of different types of particles interacting with the CMS detector.

“mustache” algorithm, and the “refined” algorithm. The mustache algorithm defines a seed cluster with energy above a certain threshold, and then combines it with other clusters within a region of the $\eta\phi$ plane centered at the seed location. The refined algorithm uses the mustache superclusters and tracking information to extrapolate bremsstrahlung and conversion tracks, in order to decide whether a cluster should belong to the supercluster.

The distinction between photons and electrons is made using tracking information, where photons are associated with no tracks and electrons with tracks. The Gaussian Sum Filter (GSF) [48] track fitting algorithm is used to identify and characterize tracks that might be associated with an electron. It first begins with a hit pattern in the tracker, which is used as a seed. This seed can either be tracker-driven, coming from the collection

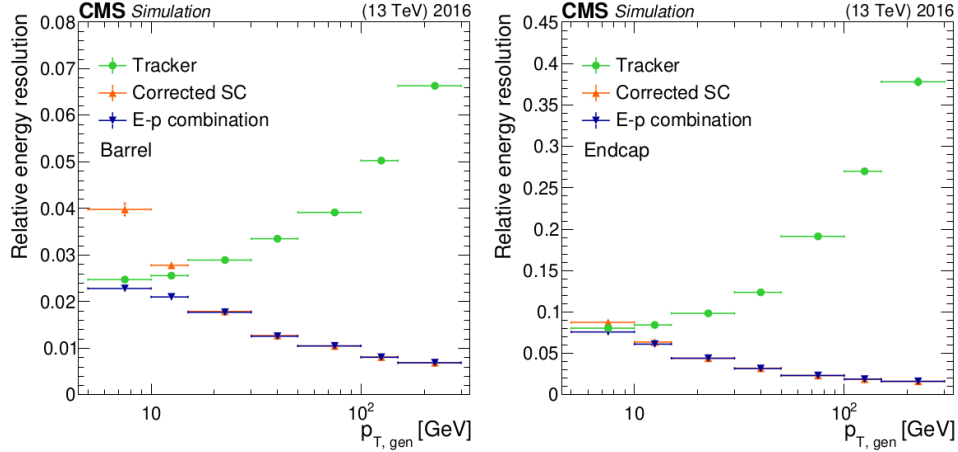


Figure 3.7. Energy resolution for simulated electrons in the barrel (left) and endcaps (right) as a function of generated p_T [49]. The green markers represent tracker measurement only, the orange markers represent ECAL measurement only, and the purple markers represent the combination of tracker and ECAL information.

of generic tracks tested for mutual compatibility, or it can be ECAL-driven, where a mustache supercluster is compared in location with a collection of tracker hit patterns to determine if the supercluster is consistent with the trajectory indicated by the track. Electron seeds are then converted into reconstructed electron tracks. In the absence of any GSF electron tracks, a photon candidate is obtained. Additional distinction between photons and electrons is obtained through further selection requirements. Fig. 3.7 shows the energy resolution for simulated electrons in the barrel and endcaps as a function of generated p_T . The measured energy resolution for electrons produced in Z boson decays in pp collision data ranges from 2–5%, depending on electron pseudorapidity and energy loss through bremsstrahlung in the detector material [49].

3.4.2. Muon Reconstruction

Muon reconstruction utilizes information from the muon detectors and the tracker. First, detector hits in the CSCs, DTs, and RPCs are used to build standalone tracks using a Kalman filter [50] technique. Subsequently, these standalone muon tracks are combined with tracker information via two algorithms. So-called “tracker muons” are reconstructed using an “inside-out” algorithm, which starts from tracker tracks and matches them to DT or CSC segments. So-called “global muons” are reconstructed with an “outside-in” approach, which starts from standalone muon tracks and matches them to tracker tracks using a Kalman filter technique. If both algorithms reconstruct a muon sharing the same tracker track, the two outputs are merged into a single muon candidate. In general, the tracker muon algorithm is more efficient for low muon p_T , while the global algorithm is more efficient for high p_T .

The momentum of muons is obtained from the corresponding track momentum. Matching muons to tracks measured in the silicon tracker results in a p_T resolution, for muons with p_T up to 100 GeV, of 1% in the barrel and 3% in the endcaps. The p_T resolution in the barrel is better than 7% for muons with p_T up to 1 TeV [43]. As shown in Fig. 3.8, this corresponds to a dimuon mass resolution in $Z \rightarrow \mu^+ \mu^-$ events of roughly 1–2 GeV, depending on the pseudorapidity of the muons [51].

3.4.3. Hadron Reconstruction

All particles within an event that are not reconstructed as photons, electrons, or muons are reconstructed as hadrons. Note that within the tracker acceptance ($|\eta| < 2.5$), all ECAL clusters not linked to a track are considered photons. All of the remaining ECAL and

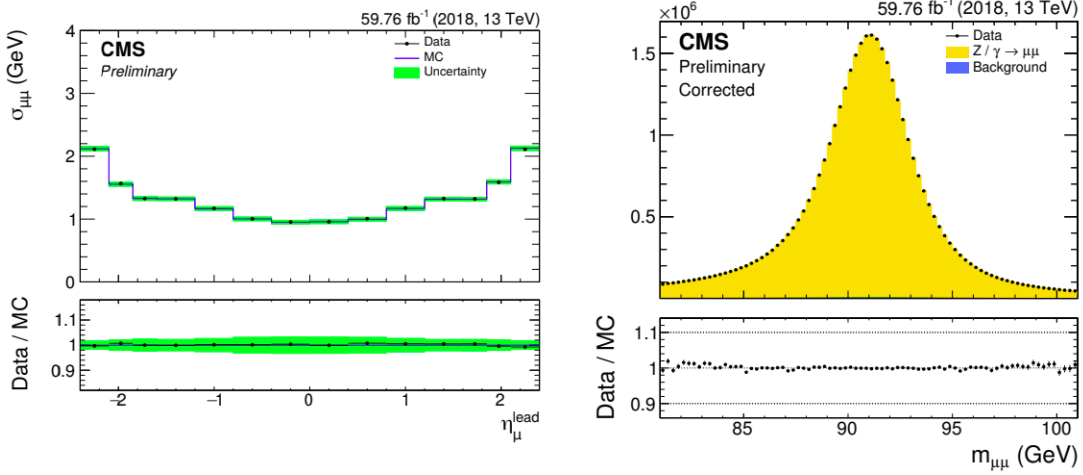


Figure 3.8. Left: dimuon mass resolution as a function of leading muon η for $Z \rightarrow \mu^+ \mu^-$ events in 2018 data and simulation. Right: reconstructed dimuon mass. [51]

HCAL clusters are processed further by the PF algorithm. The HCAL clusters are first linked to any associated tracks and ECAL clusters. Then, a comparison is made between the calorimetric energy sum and the sum of the track momenta. If the calorimetric energy sum is compatible with the sum of track momenta, a charged hadron is reconstructed. If the calorimetric energy sum is greater than the sum of track momenta, the excess prompts the reconstruction of photons and neutral hadrons, depending on the size of the excess.

3.4.4. Jet Reconstruction

For each event, hadronic jets are reconstructed as clusters of PF particles, including photons, electrons, muons, and hadrons. For clustering, the infrared and collinear-safe anti- k_T algorithm [52, 53] is used. The goal of jet clustering algorithms is to combine PF particles together into a single jet object by merging them together based on their relative geometric distances and transverse momenta (k_T). In the case of the anti- k_T algorithm, clustering

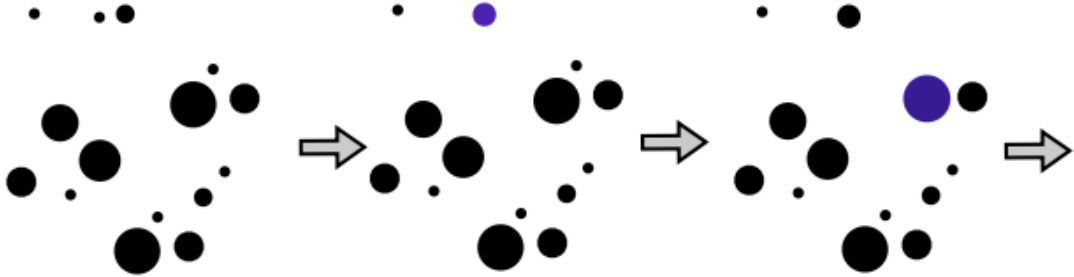


Figure 3.9. An example of the first few steps of the anti- k_{T} jet clustering algorithm.

proceeds from smallest geometric distance to largest, weighted by squared inverse k_{T} . This inverse weighting preferentially combines PF particles with higher momenta before lower momenta, for a given distance. The advantage of this approach is that low momentum particles are more likely to be clustered with high momentum counterparts, rather than with other low momentum particles. It follows that these low momentum particles will not significantly modify the jet shape, whereas the more important, high-momentum particles, will. A precise definition of the anti- k_{T} algorithm is given in equation 3.1.

$$(3.1) \quad d_{ij} = \min(k_{T,i}^{2p}, k_{T,j}^{2p}) \frac{(\eta_i - \eta_j)^2 + (\phi_i - \phi_j)^2}{R^2}, \quad d_i = k_{T,i}^{2p}$$

The indices i and j refer to two PF particles, the parameter p is taken to be -1, and the radius parameter R can be tuned. For standard jets in CMS, as used in this analysis, R is set to 0.4. Particles are clustered from smallest d_{ij} to largest, until there is no d_{ij} smaller than k_{ti}^{-2} , at which point the final jet is defined. A visual representation of the anti- k_{T} algorithm is shown in Fig. 3.9.

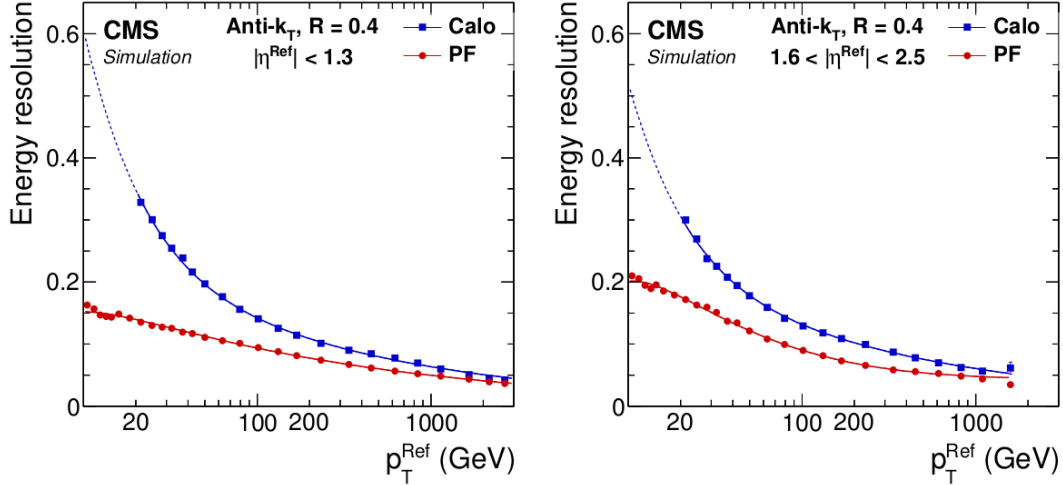


Figure 3.10. Jet energy resolution as a function of simulated jet p_T in the barrel (left) and in the endcap (right) regions [47]. Calo refers to the sum of ECAL and HCAL energy deposits, while PF corresponds to jets clustered from PF particles using the anti- k_T algorithm.

Jet momentum is determined as the vectorial sum of all particle momenta in the jet, and is found from simulation to be, on average, within 5–10% of the true momentum over the entire p_T spectrum and detector acceptance. Additional pp interactions within the same or nearby bunch crossings (pileup) can contribute additional tracks and calorimetric energy depositions to the jet momentum. To mitigate this effect, charged particles identified as originating from pileup vertices are discarded, and an offset correction is applied to correct for the remaining contributions [54]. The jet energy resolution, as shown in Fig. 3.10, typically amounts to 15–20% at 30 GeV, 10% at 100 GeV, and 5% at 1 TeV [55].

CHAPTER 4

Analysis Overview

4.1. History of the $H \rightarrow Z\gamma$ Search

Both the CMS and ATLAS collaborations have undertaken the search for $H \rightarrow Z\gamma$ since Run 1 of the LHC. Before the CMS Run 2 analysis, which is the focus of this thesis, each collaboration published results using Run 1 data at $\sqrt{s} = 7$ and 8 TeV [20, 19], CMS published a result with 2016 data at $\sqrt{s} = 13$ TeV [21], and ATLAS published a full Run 2 result at $\sqrt{s} = 13$ TeV [22]. As such, the present analysis represents the continuation of a broader effort, so we will give a brief history of these prior searches to put our work in context. While some of the analysis strategies of past searches inform our current strategy, there are also many differences and innovations in our analysis. We will emphasize the ways in which our analysis overlaps and differs with previous approaches, and will show that our innovations have significantly improved the expected sensitivity and statistical robustness of the search.

4.1.1. The Run 1 Searches

In 2014, ATLAS published its Run 1 results [19] for the search for $H \rightarrow Z\gamma$ where $Z \rightarrow \ell^+ \ell^-$ with $\ell = e$ or μ . The baseline strategy was a standard dilepton plus photon selection, with $m_{\ell^+ \ell^-}$ near the Z boson mass and $\ell^+ \ell^- \gamma$ invariant mass ($m_{\ell^+ \ell^- \gamma}$) between 115 and 170 GeV. The resolution of $m_{\ell^+ \ell^- \gamma}$ was improved using a kinematic fit procedure,

accounting for the true Z boson line shape. Events were categorized based on lepton flavor; the pseudorapidity difference between the photon and Z boson; and the variable p_T^t , defined as $|\vec{p}_T^{Z\gamma} \times \hat{t}|$, where $\hat{t} = (\vec{p}_T^Z - \vec{p}_T^\gamma)/|\vec{p}_T^Z - \vec{p}_T^\gamma|$ [56, 57], the p_T of the $Z\gamma$ system that is perpendicular to the difference of the three-momenta of the Z boson and the photon, a quantity that is strongly correlated with the p_T of the $\ell^+\ell^-\gamma$ system. Limits on the signal strength relative to the SM prediction, shown in Fig. 4.1 (left), were obtained from a simultaneous fit to the $m_{\ell^+\ell^-\gamma}$ distributions in all categories.

The CMS Run 1 analysis [20] was published in 2015 for the $\mu^+\mu^-\gamma$ and $e^+e^-\gamma$ final states. It employed a standard dilepton plus photon selection, but the $m_{\ell^+\ell^-\gamma}$ range was 100–190 GeV, which includes a kinematic turn-on around 110–115 GeV, mainly driven by the photon p_T selection. The choice to model this turn-on increased the complexity of the fit relative to the ATLAS analysis above, but was made in order to minimize potential bias. Events were categorized based on flavor; presence of a dijet system; lepton and photon pseudorapidity; and the photon R_9 , which is the energy sum of the 3x3 ECAL crystal array centered on the most energetic crystal divided by the supercluster energy, and is associated with the quality of the photon. The CMS Run 1 limits on the signal strength are shown in Fig. 4.1 (right).

4.1.2. The Previous Run 2 Searches

The first CMS $H \rightarrow Z\gamma$ results at $\sqrt{s} = 13$ TeV [21] were published in 2018 using the 2016 data set, corresponding to an integrated luminosity of 35.9 fb^{-1} . The search strategy was largely similar to the CMS Run 1 analysis, with a few main differences. First, a boosted category was introduced to the analysis, defined by $p_T^{\ell^+\ell^-\gamma} > 60 \text{ GeV}$. This category

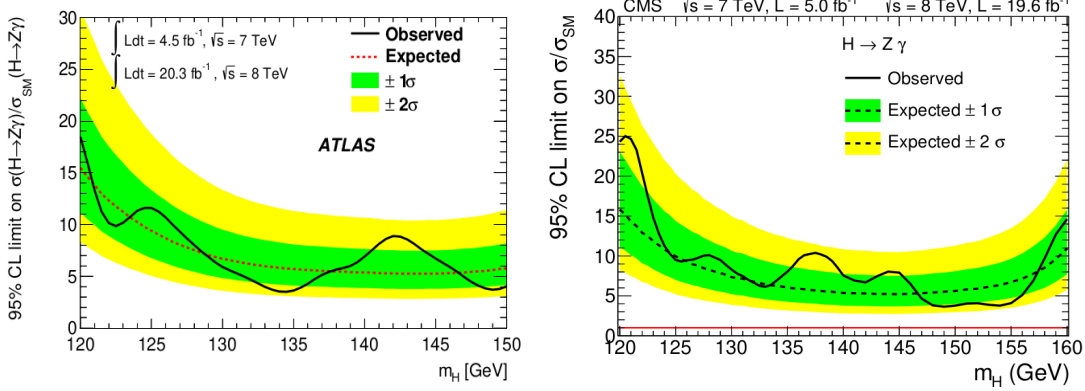


Figure 4.1. ATLAS (left [19]) and CMS (right [20]) Run 1 limit results as a function of m_H .

targeted events with a Higgs boson recoiling against a jet. Second, the range of $m_{\ell^+\ell^-\gamma}$ was restricted to 115–170 GeV in order to avoid fitting the kinematic turn-on. The decision of whether or not to fit the turn-on became critically important in the full CMS Run 2 analysis, and will be discussed in more detail later in this thesis. Limits from the CMS 2016 search are shown in Fig. 4.2 (left).

The ATLAS full Run 2 search [22] was published in 2020, with a largely similar strategy to the Run 1 analysis. As in Run 1, a kinematic fit was used to improve the $m_{\ell^+\ell^-\gamma}$ resolution and the variable p_T^t was used for categorization. However, there were a few major differences introduced in the Run 2 analysis. The fit range was changed to $105 \text{ GeV} < m_{\ell^+\ell^-\gamma} < 160 \text{ GeV}$ and some aspects of the categorization strategy were updated. For categorization, the most significant change was the use of a boosted decision tree (BDT) trained to separate VBF Higgs production events from other Higgs production mechanisms and backgrounds. As will be discussed later in this thesis, the use of BDTs for categorization can significantly improve the sensitivity of searches for $H \rightarrow Z\gamma$. Figure

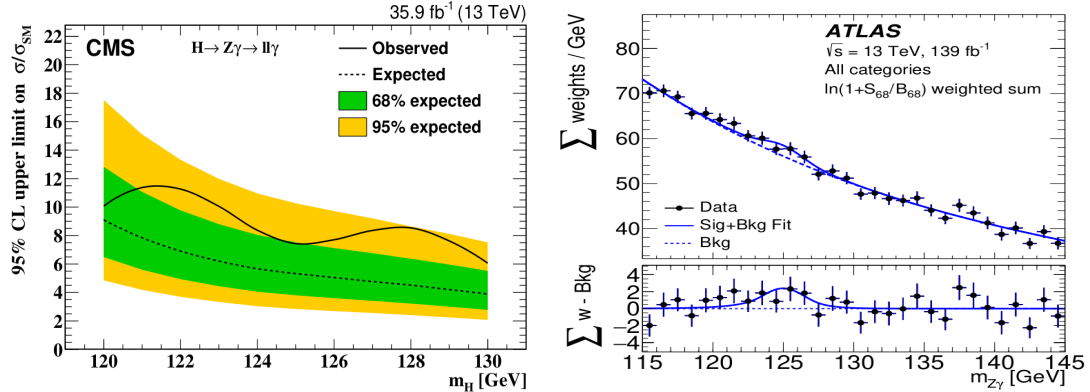


Figure 4.2. Left: CMS 2016 limit results [21] as a function of m_H . Right: ATLAS Run 2 signal plus background fit [22], for $m_H = 125.09$ GeV, weighted by $\ln(1+S_{68}/B_{68})$, where S_{68} and B_{68} are the expected signal and background events in an $m_{\ell^+\ell^-\gamma}$ window containing 68% of the expected signal yield.

4.2 (right) shows a summary of the fit results for the ATLAS Run 2 search. An excess in data was observed, corresponding to 2.2 standard deviations for $m_H = 125.09$ GeV.

4.2. The CMS Run 2 Strategy

The remainder of this thesis provides a thorough description of the CMS Run 2 search for $H \rightarrow Z\gamma$. First, a brief overview is provided below. The data sample corresponds to an integrated luminosity of 138 fb^{-1} of pp collisions at $\sqrt{s} = 13 \text{ TeV}$ accumulated between 2016 and 2018. Much of the analysis strategy has been inspired by the prior CMS and ATLAS $H \rightarrow Z\gamma$ searches, as well as other CMS Higgs analyses. The baseline event selection is similar to the previous CMS searches. One crucial difference with respect to the CMS 2016 analysis is that the $m_{\ell^+\ell^-\gamma}$ range has been extended to 105–170 GeV, including the kinematic turn-on, as was done in the CMS Run 1 analysis. This choice will be discussed in detail later in this thesis. Additionally, a kinematic fit procedure has been

added to the analysis to improve the $m_{\ell^+\ell^-\gamma}$ resolution, similar to what has been done in the previous ATLAS $H \rightarrow Z\gamma$ analyses and in other CMS Higgs analyses, including $H \rightarrow ZZ^* \rightarrow 4\ell$ [58].

The sensitivity of the analysis is enhanced by searching for Higgs boson production in a variety of mechanisms, including gluon-gluon fusion (ggH); vector boson fusion (VBF); and the associated production of a Higgs boson with either a weak vector boson (VH , where $V = Z$ or W) or a top quark pair ($t\bar{t}H$). The dominant backgrounds arise from Drell–Yan production in association with an initial-state photon ($Z/\gamma^* + \gamma$) and Drell–Yan production in association with jets, where a jet or additional lepton is misidentified as a photon ($Z/\gamma^* + \text{jets}$). After using a set of discriminating variables to suppress background in the different production mechanisms, the signal is identified as a narrow resonant peak around m_H in the distribution of $m_{\ell^+\ell^-\gamma}$.

The data sample is divided into mutually exclusive categories according to (i) the presence of an additional lepton produced by $Z(\rightarrow \ell^+\ell^-)$ or $W(\rightarrow \ell\nu)$ decay, indicating the possible associated production of a Higgs boson with a W or Z boson, or $t\bar{t}H$ production with a leptonic top quark decay; (ii) the value of a multivariate analysis (MVA) discriminant characterizing the kinematic properties of a dijet system together with the $\ell^+\ell^-\gamma$ candidate, indicating possible VBF production; and (iii) the value of an MVA discriminant characterizing the kinematic properties of the $\ell^+\ell^-\gamma$ system. This MVA categorization procedure is an innovation of the CMS Run 2 analysis. While a VBF MVA was used in the ATLAS full Run 2 analysis, we are the first to also leverage a kinematic MVA for maximal discrimination between signal and background.

CHAPTER 5

Data and Simulated Samples

The data sample used for the CMS Run 2 $H \rightarrow Z\gamma$ search corresponds to a total integrated luminosity of 138 fb^{-1} and was collected over a data-taking period spanning three years: 36.3 fb^{-1} in 2016, 41.5 fb^{-1} in 2017, and 59.8 fb^{-1} in 2018 [59, 60, 61]. To be considered in the analysis, events must satisfy the HLT requirements for at least one of the dielectron or dimuon triggers. The dielectron trigger requires a leading (subleading) electron with $p_T > 23$ (12) GeV, while the dimuon trigger requires a leading (subleading) muon with $p_T > 17$ (8) GeV. The corresponding CMS data streams are listed in Table 5.1. All data samples use the CMS MINIAOD data format. To ensure data quality, luminosity masks are applied based on recommendations from the Physics Performance and Dataset group.

Signal samples for ggH, VBF, VH, and $t\bar{t}H$ production, with $H \rightarrow Z\gamma$ and $Z \rightarrow \ell^+\ell^-$ ($\ell = e, \mu$, or τ), are generated at next-to-leading order (NLO) using POWHEG v2.0 [62, 63]. These samples are produced for m_H of 120, 125, and 130 GeV. The dominant backgrounds, $Z/\gamma^*(\rightarrow \ell^+\ell^-)+\gamma$ and $Z/\gamma^*(\rightarrow \ell^+\ell^-)+\text{jets}$, are generated at NLO using the MADGRAPH5_aMC@NLO v2.6.0 (v2.6.1) generator [64] for 2016 (2017 and 2018) samples. Events arising from $t\bar{t}$ production [65] are a relatively minor background and are generated at NLO with POWHEG v2.0 [62, 63]. The background from vector boson scattering (VBS) production of $Z/\gamma^*+\gamma$ pairs, with the Z boson decaying to a pair of leptons, is simulated at leading order using the MADGRAPH5_aMC@NLO generator. The decay $H \rightarrow \mu^+\mu^-$

Table 5.1. Summary of MINIAOD data samples used.

$e^+e^-\gamma$ final state	$\mu^+\mu^+\gamma$ final state
/DoubleEG/Run2016B-17Jul2018_ver2-v1	/DoubleMuon/Run2016B-17Jul2018_ver2-v1
/DoubleEG/Run2016C-17Jul2018-v1	/DoubleMuon/Run2016C-17Jul2018-v1
/DoubleEG/Run2016D-17Jul2018-v1	/DoubleMuon/Run2016D-17Jul2018-v1
/DoubleEG/Run2016E-17Jul2018-v1	/DoubleMuon/Run2016E-17Jul2018-v1
/DoubleEG/Run2016F-17Jul2018-v1	/DoubleMuon/Run2016F-17Jul2018-v1
/DoubleEG/Run2016G-17Jul2018-v1	/DoubleMuon/Run2016G-17Jul2018-v1
/DoubleEG/Run2016H-17Jul2018-v1	/DoubleMuon/Run2016H-17Jul2018-v1
/DoubleEG/Run2016H-17Jul2018-v1	/DoubleMuon/Run2016H-17Jul2018-v1
/DoubleEG/Run2017B-31Mar2018-v1	/DoubleMuon/Run2017B-31Mar2018-v1
/DoubleEG/Run2017C-31Mar2018-v1	/DoubleMuon/Run2017C-31Mar2018-v1
/DoubleEG/Run2017D-31Mar2018-v1	/DoubleMuon/Run2017D-31Mar2018-v1
/DoubleEG/Run2017E-31Mar2018-v1	/DoubleMuon/Run2017E-31Mar2018-v1
/DoubleEG/Run2017F-31Mar2018-v1	/DoubleMuon/Run2017F-31Mar2018-v1
/EGamma/Run2018A-17Sep2018-v2	/DoubleMuon/Run2018A-17Sep2018-v2
/EGamma/Run2018B-17Sep2018-v1	/DoubleMuon/Run2018B-17Sep2018-v1
/EGamma/Run2018C-17Sep2018-v1	/DoubleMuon/Run2018C-17Sep2018-v1
/EGamma/Run2018D-22Jan2019-v2	/DoubleMuon/Run2018D-PromptReco-v2

is considered as a resonant background and is generated for the ggH, VBF, VH, and $t\bar{t}H$ production mechanisms. The ggH production cross section is computed at next-to-next-to-NLO precision in QCD and at NLO in electroweak (EWK) theory [66]. The cross sections for Higgs boson production in the VBF [67] and VH [68] mechanisms are calculated at next-to-NLO in QCD, including NLO EWK corrections, while the $t\bar{t}H$ cross section is computed at NLO in QCD and EWK theory [69].

A full list of simulated physics processes used in the analysis is provided in Table 5.2, along with cross section and branching fraction information. For the $H \rightarrow Z\gamma$ and $H \rightarrow \mu^+\mu^-$ samples, the SM Higgs boson production cross sections and branching fractions recommended by the LHC Higgs Working Group [12] are used for each mass point. The values for the Higgs boson processes listed in Table 5.2 correspond to $m_H = 125$ GeV.

Table 5.2. Simulated event samples used in the analysis. For Higgs samples, the listed cross sections and branching fractions correspond to the values for $m_H = 125$ GeV.

process	cross section (pb)	branching fraction
ggH $\rightarrow Z\gamma \rightarrow \ell^+\ell^-\gamma$	48.58	1.548×10^{-3}
q \bar{q} H $\rightarrow Z\gamma \rightarrow \ell^+\ell^-\gamma$	3.782	1.548×10^{-3}
ZH $\rightarrow Z\gamma \rightarrow \ell^+\ell^-\gamma$	0.8839	1.548×10^{-3}
W $^+H \rightarrow Z\gamma \rightarrow \ell^+\ell^-\gamma$	0.84	1.548×10^{-3}
W $^-H \rightarrow Z\gamma \rightarrow \ell^+\ell^-\gamma$	0.532	1.548×10^{-3}
t $\bar{t}H \rightarrow Z\gamma \rightarrow \ell^+\ell^-\gamma$	0.5071	1.548×10^{-3}
ggH $\rightarrow \mu^+\mu^-$	48.58	2.176×10^{-4}
q \bar{q} H $\rightarrow \mu^+\mu^-$	3.782	2.176×10^{-4}
ZH $\rightarrow \mu^+\mu^-$	0.8839	2.176×10^{-4}
W $^+H \rightarrow \mu^+\mu^-$	0.84	2.176×10^{-4}
W $^-H \rightarrow \mu^+\mu^-$	0.532	2.176×10^{-4}
t $\bar{t}H \rightarrow \mu^+\mu^-$	0.5071	2.176×10^{-4}
Z/ $\gamma^* \rightarrow \ell^+\ell^-\gamma$	117.864	—
Z/ $\gamma^* \rightarrow \ell^+\ell^- + \text{jets}$	6225.42	—
t \bar{t} (inclusive)	831.76	—
VBF Z/ $\gamma^* + \gamma$	0.1097	—

All simulated events are interfaced with PYTHIA v8.226 (v8.230) [70] with the CUETP8M1 [71] (CP5 [72]) underlying event tune for 2016 (2017–2018) for the fragmentation and hadronization of partons and the internal bremsstrahlung of the leptons. The NLO parton distribution function (PDF) set, NNPDF v3.0 [73] (NNPDF v3.1) [74], is used to produce these samples in 2016 (2017–2018). The response of the CMS detector is modeled using the GEANT4 program [75]. The simulated events are reweighted to correct for differences between data and simulation in the number of additional pp interactions, trigger efficiencies, selection efficiencies, and efficiencies of isolation requirements for photons, electrons, and muons. These corrections and their associated uncertainties will be described in more

detail throughout the remainder of this thesis. The rest of this chapter will discuss general procedures and corrections related to the data and simulated samples.

5.1. Z+jets Overlap Removal

The two dominant backgrounds in this analysis are $Z/\gamma^*(\rightarrow \ell^+\ell^-) + \gamma$, or $Z\gamma$ for short, and $Z/\gamma^*(\rightarrow \ell^+\ell^-) + \text{jets}$, or $Z+\text{jets}$ for short. Both processes are simulated independently in order to obtain the best model of the kinematics of the $\ell^+\ell^-\gamma$ system. The $Z\gamma$ sample simulates photons from initial-state and final-state radiation at the matrix element level and includes a better computation of the interference between the corresponding Feynman diagrams than the $Z+\text{jets}$ sample. However, the $Z+\text{jets}$ simulated sample also includes the contribution from $Z\gamma$. Therefore, this contribution must be removed from the $Z+\text{jets}$ sample in order to avoid double counting events and to utilize the better kinematic modeling of the $Z\gamma$ sample. To handle this, $Z+\text{jets}$ events are removed from the analysis if they contain prompt, final state photons within $\Delta R = \sqrt{(\Delta\phi)^2 + (\Delta\eta)^2} = 0.1$ of the photon selected to reconstruct the $\ell^+\ell^-\gamma$ system. The events with prompt, final state photons are tagged using generator-level truth information.

5.2. Photon Internal Conversion

The PYTHIA 8 showering algorithm automatically includes a component in which $H \rightarrow \gamma\gamma$ photons are internally converted via the process $H \rightarrow \gamma\gamma^* \rightarrow f\bar{f}\gamma\gamma$, with $f\bar{f}$ mostly e^+e^- . This also affects the $H \rightarrow Z\gamma$ signal and $Z\gamma$ background samples. Since the normalization of these samples does not include the internal conversion component, the cross section must be adjusted accordingly. To determine the amount by which the cross section is adjusted, we measure the internal conversion rate in simulation. We define a

ratio where the numerator is the number of events with hard process final state photons and the denominator is total number of events in the simulation. Subtracting this ratio from unity gives the internal conversion rate. The hard process final state photon flagging is done using generator-level truth information. In our analysis, the internal conversion rate is about 3.1% (2016) and 3.0% (2017 and 2018). We, therefore, divide the affected sample cross sections by 0.969 (0.97) for 2016 (2017 and 2018).

5.3. Transverse Momentum Reweighting

The underlying event tuning was updated from CUETP8M1 (2016) to CP5 (2017–2018). Unfortunately, it was discovered that this update caused significant mismodeling of the $\ell^+\ell^-\gamma p_T$ spectrum in the $Z\gamma$ and $Z+jets$ background samples in 2017 and 2018. Figure 5.1 (left) shows the clear difference between simulated $p_T^{\ell^+\ell^-\gamma}$ in 2016 and 2017–2018. As will be described later in this thesis, the variable $p_T^{\ell^+\ell^-\gamma}/m_{\ell^+\ell^-\gamma}$ has good discriminating power between signal and background and is a useful feature for MVA training. Therefore, it is important to correct this discrepancy. To do this, a simple reweighting of the distribution is performed using two sideband regions in $m_{\ell^+\ell^-\gamma}$. The sidebands are defined as 115–120 and 130–135 GeV. The resulting weights are then applied to the $Z\gamma$ and $Z+jets$ simulated events in 2017 and 2018. Figure 5.1 (right) shows the final distribution of $p_T^{\ell^+\ell^-\gamma}/m_{\ell^+\ell^-\gamma}$ for all data-taking years combined after the $p_T^{\ell^+\ell^-\gamma}$ reweighting is applied. The overall agreement between data and simulation is good over the full p_T spectrum.

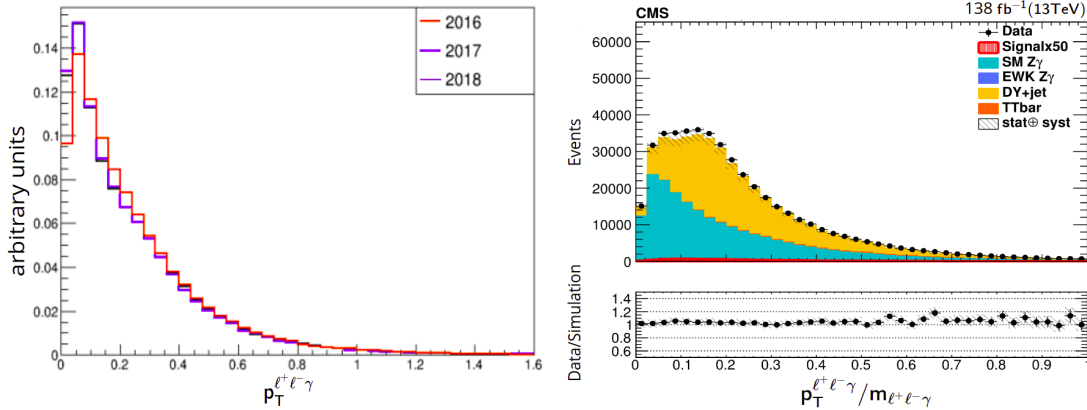


Figure 5.1. Left: Background simulation modeling of $p_T^{\ell^+\ell^-\gamma}$ in each data-taking year. There is a shape discrepancy between 2016 and 2017–2018 due to the updated underlying event tuning. Right: Final comparison between data and simulation after the $p_T^{\ell^+\ell^-\gamma}$ reweighting is performed on 2017 and 2018 background simulation.

5.4. Pileup Reweighting

In order to correctly model the pileup distribution in data, a pileup reweighting procedure must be applied to the simulation. Although the Deterministic Annealing primary vertex (PV) reconstruction [76] has been shown to be efficient and well-behaved up to the observed levels of pileup, the final distribution for the number of reconstructed PVs is still sensitive to differences between data and simulation in the PV reconstruction and underlying event. Additionally, the offline event selection criteria and trigger can potentially impact the distribution for the number of reconstructed vertices. To handle this, the pileup distribution for data is first derived by using the per-bunch-crossing, per-luminosity-section instantaneous luminosity, together with the total pp inelastic cross section. The total pp inelastic cross section is taken to be 66 mb, 72.4 mb, and 80 mb

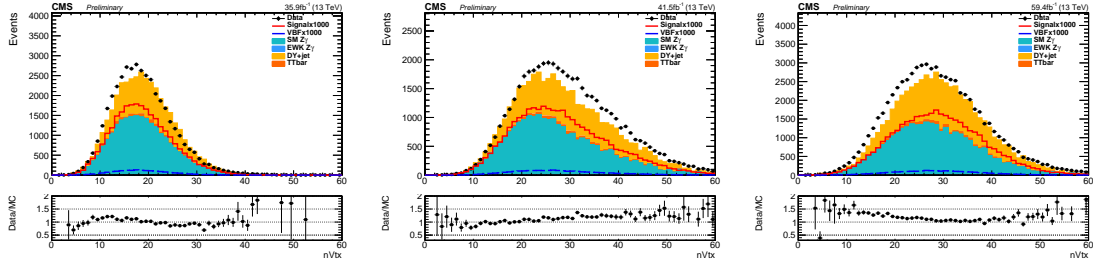


Figure 5.2. Distributions of the number of primary vertices in data and simulation for $e^+e^-\gamma$ events in 2016 (left), 2017 (center), and 2018 (right) after pileup reweighting.

for 2016, 2017, and 2018 respectively. This yields an expected pileup distribution, correctly weighted over the entire data-taking period. The simulation is then reweighted to match this expected pileup distribution. Figure 5.2 shows the number of PV after pileup reweighting for each data-taking year. The uncertainties associated with pileup reweighting are accounted for in the analysis and are discussed further in Chapter 9.

5.5. Level-1 Trigger Prefiring Reweighting

In 2016 and 2017, a gradual timing shift of the ECAL was not properly propagated to L1 trigger primitives, resulting in a significant fraction of high-pseudorapidity trigger primitives mistakenly associated to the previous bunch crossing [77]. Since L1 trigger rules forbid two consecutive bunch crossings from triggering, a consequence is that events can self-veto if a significant amount of ECAL energy is found in the region $2 < |\eta| < 3$. This effect is not described in simulation. To handle this, a weight is applied to each simulated event based on the probability of an event not to prefire and self-veto. The prefire probability is determined by measuring the timing distributions of physics objects in the subset of data events for which prefire is impossible due to the lack of a L1 trigger accept in the previous bunch crossing. The measurement is parameterized in η and p_T . The final

event weight applied to the simulation is the product of the non-prefiring probability of all objects, as shown in equation 5.1.

$$(5.1) \quad \omega = 1 - P(\text{Prefiring}) = \prod_{i=\text{photons, jets, muons}} (1 - \epsilon_i^{\text{pref}}(\eta, p_T^{\text{EM}, \mu}))$$

The impact of the L1 prefiring for electrons (muons) is a 1.4 (0.8)% loss in signal yield for 2016 and 2.4 (1.1)% loss in signal yield for 2017. The uncertainties associated with the L1 prefiring reweighting are accounted for in the analysis and are discussed further in Chapter 9.

CHAPTER 6

Physics Object and Event Selection

This chapter outlines the basic $H \rightarrow Z\gamma$ physics object and event selection before any event categorization is done. Along the way, we will also point out the most relevant corrections applied, including trigger scale factors (SFs), physics object energy and momentum corrections, and identification and isolation SFs.

6.1. Primary Vertex

Events are required to have at least one good PV with a reconstructed longitudinal position within 24 cm of the geometric center of the detector and a transverse position within 2 cm of the nominal beam collision point. To avoid fake vertices, the PV reconstruction is required to have more than four degrees of freedom. In the case of multiple satisfactory vertices, the vertex with the highest scalar sum of squared p_T is chosen.

6.2. Triggers

The topology and kinematics of the $H \rightarrow Z\gamma$ process guide the choice of triggers used in this analysis. As there are at least three final state decay products, the photon p_T tends to be less than in other channels, such as $H \rightarrow \gamma\gamma$. Consequently, the CMS single photon trigger p_T thresholds are too great to make them viable options. In addition, there is no suitable unprescaled multijet plus photon trigger to target events with hadronic decays of the Z boson, so the triggers are chosen to target the $\ell^+\ell^-\gamma$ final states. Therefore,

we trigger on the leptons arising from the decay of the Z boson, which tend to have larger values of p_T . The best approach to maximize signal efficiency is to use the double lepton triggers. The dielectron trigger requires a leading (subleading) electron with $p_T > 23(12)$ GeV, while the dimuon trigger requires a muon with $p_T > 17(8)$ GeV. Events passing both the double muon and double electron triggers are classified as $\mu^+\mu^-\gamma$ events.

The triggers are applied to both data and simulation. Trigger efficiencies and SFs are measured using the simulation samples corresponding to each data-taking year. These measurements use a tag and probe [78] method. This method takes advantage of the high purity of $Z \rightarrow \ell^+\ell^-$ events near the Z boson mass peak. One lepton functions as the tag, and satisfies a set of tight trigger, identification, isolation, and p_T requirements. The second lepton, the probe, must pass a looser selection and is used to measure the efficiency in question. Using this approach, trigger efficiencies for each leg of a given double lepton trigger are measured in both data and simulation. Then a corrective SF, defined as the ratio of data efficiency to simulation efficiency, is applied to the simulation. Scale factors are measured and applied in bins of p_T and $|\eta|$.

For the double electron trigger efficiency measurements, the tag electron must satisfy a set of requirements. The tag must pass the single electron trigger, pass a tight cut-based identification, have $p_T > 30(35)$ GeV in 2016 (2017 and 2018), and have $|\eta| < 2.5$. The probe electron must pass a loose electron MVA identification requirement. The details of the electron MVA identification will be described later in this chapter. The efficiencies for each leg of the trigger are measured separately, so in each case, the probe electron must match the trigger leg being measured. The efficiencies for each double electron trigger leg

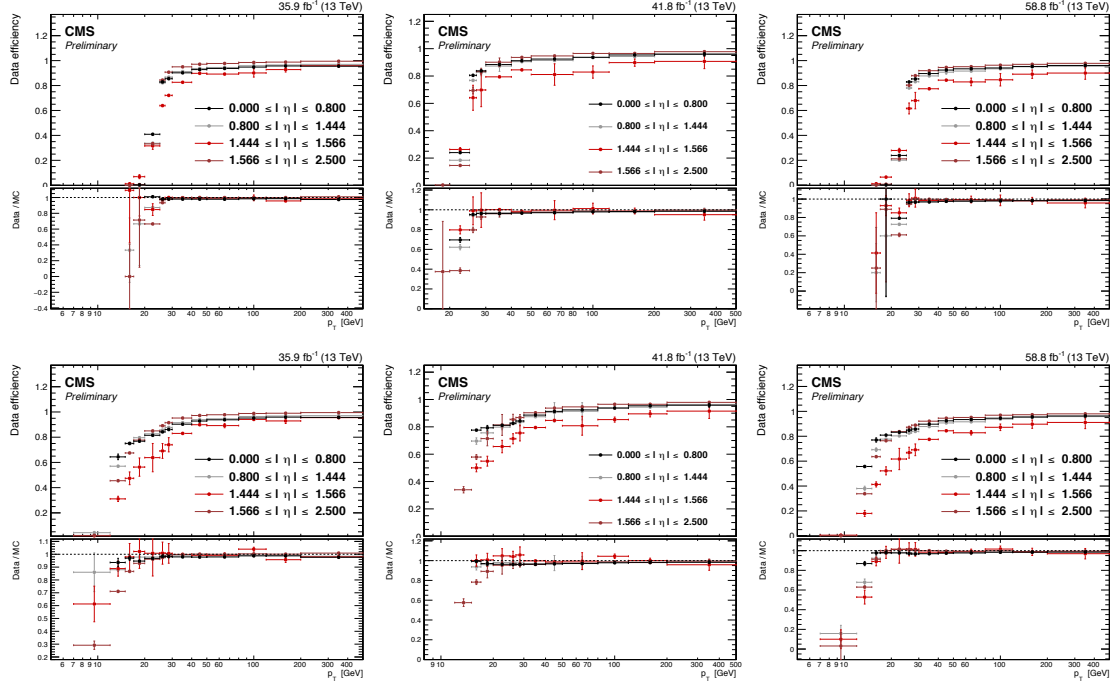


Figure 6.1. Efficiency measurements for each leg of the double electron trigger in 2016 (left), 2017 (center), and 2018 (right). The upper (lower) plots correspond to the leading (subleading) trigger leg.

for 2016, 2017, and 2018 are shown in Fig. 6.1. On average, the double electron trigger efficiency is measured to be in the range of 86–97%, depending on the electron p_T and η .

For the double muon trigger efficiency measurements, the tag muon must satisfy a set of requirements. It must pass the single muon trigger, pass a tight cut-based identification, have $p_T > 26$ (29) GeV for 2016 (2017 and 2018) and satisfy $|\eta| < 2.4$. The probe muon must pass the $H \rightarrow ZZ$ identification and isolation cuts. The details of the $H \rightarrow ZZ$ muon identification will be described later in this chapter. The efficiencies for each leg of the trigger are measured separately, so in each case, the probe muon must match the trigger leg being measured. The efficiencies for each double muon trigger leg for 2016, 2017, and

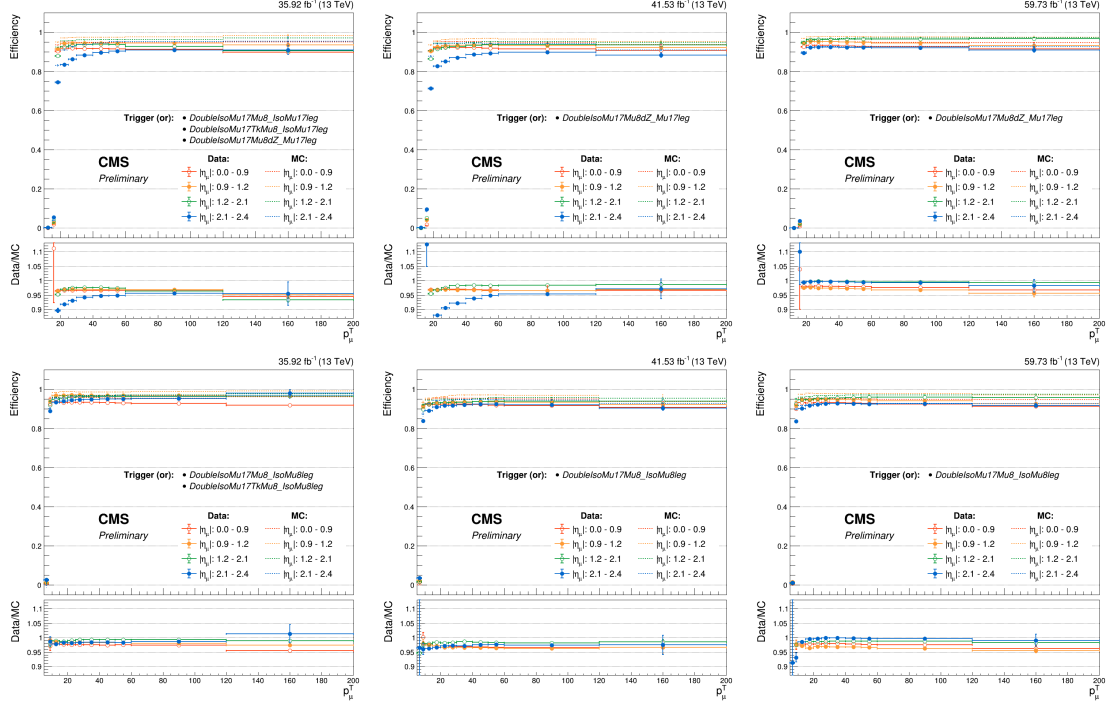


Figure 6.2. Efficiency measurements for each leg of the double muon trigger in 2016 (left), 2017 (center), and 2018 (right). The upper (lower) plots correspond to the leading (subleading) trigger leg.

2018 are shown in Fig. 6.2. On average, the double muon trigger efficiency is measured to be in the range of 93–95%, depending on the muon p_T and η .

6.3. Photon Selection

Photons are identified using a BDT discriminant (photon MVA ID) trained on $\gamma + \text{jets}$ simulation in order to distinguish real photons from jets misreconstructed as photons. The features used for the BDT training include supercluster kinematics, isolation variables, and shower shape variables [79]. To reject electrons faking photons, a conversion-safe electron veto is also applied. In order to improve agreement between simulation and data for the photon MVA ID, shower shape corrections are taken from the CMS $H \rightarrow \gamma\gamma$

analysis of the same data set [13] and applied to simulated events. The photon MVA ID is then reevaluated after these corrections. We correct the following features: R_9^{5x5} , defined as the ratio of energy in the 5x5 array of ECAL crystals to the supercluster energy; S_4 , defined as the ratio of the maximum energy 2x2 array to the energy of the 5x5 array; the energy weighted shower widths σ_η and σ_ϕ ; the energy weighted widths by crystal index $\sigma_{i\eta i\eta}$ and $\sigma_{i\eta i\phi}$; photon isolation, charged isolation with respect to the primary vertex, and charged isolation with respect to the worst vertex choice. The validity of the shower shape corrections is checked using tag and probe procedures for $Z \rightarrow e^+e^-$ events where the probe electron mimics a photon and $Z \rightarrow \mu^+\mu^-$ events with an FSR photon. Comparisons of the agreement between uncorrected and corrected simulation with data for the photon MVA ID are shown in Fig. 6.3. Similar plots for individual shower shape features can be found in Appendix A.

Based on the corrected photon MVA ID, 90% signal efficiency working point (WP) cuts for barrel and endcap photons are determined for the $H \rightarrow Z\gamma$ analysis. The WPs are defined based on real photons from $Z\gamma$ simulation, and correspond to photon MVA ID scores greater than -0.4 (-0.59) for barrel (endcap) photons. These relatively loose cuts are chosen because the photon MVA ID is later used as an input to a BDT for categorization, as described in the next chapter. A comparison of these WPs with the general CMS 90% efficiency WPs, plotted on the receiver operator characteristic (ROC) curve for $Z\gamma$ (signal) and $Z+jets$ (background) simulation, is shown in Fig. 6.4. The efficiency of the photon MVA ID is measured with $Z \rightarrow e^+e^-$ data using a tag and probe technique. The tag electron must pass the single electron trigger with p_T threshold 27 (32) GeV in 2016 (2017 and 2018), pass a tight cut-based identification, have $p_T > 30$ (35) GeV for 2016

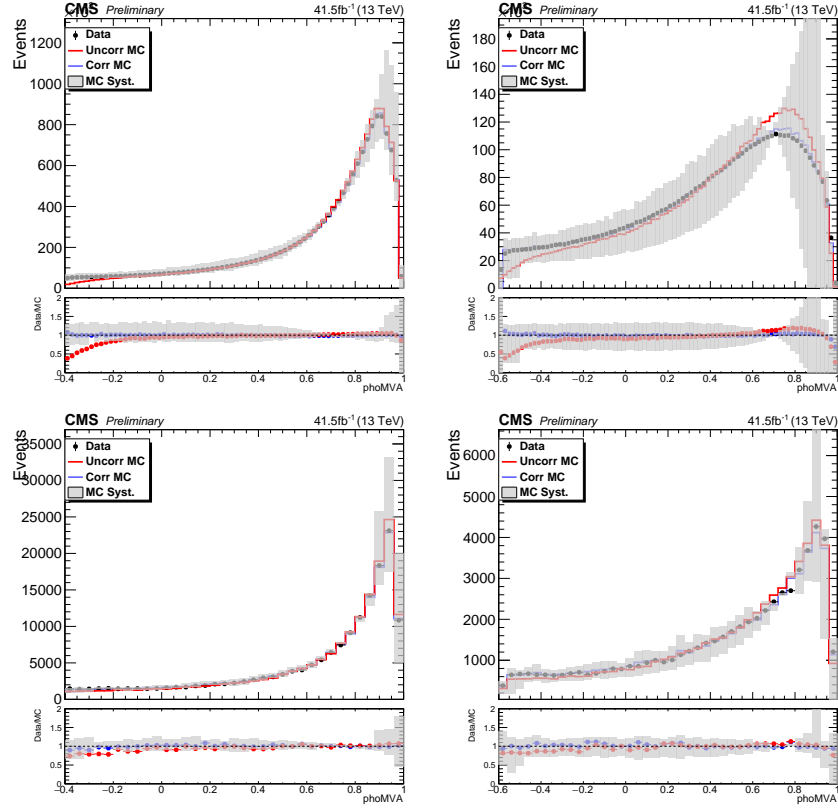


Figure 6.3. Comparison of simulation with 2017 data for the photon MVA ID before and after shower shape corrections are applied to the simulation. The plots on the left (right) correspond to the barrel and endcap regions, and the upper (lower) plots correspond to $Z \rightarrow e^+e^-$ ($Z \rightarrow \mu^+\mu^- + \gamma$) events.

(2017 and 2018), and have $|\eta| < 2.5$. The probe electron must pass the corrected photon MVA ID. The corresponding SFs, measured and applied in bins of p_T and supercluster η , are shown in Fig. 6.5. The efficiencies and SFs for the conversion-safe electron veto are measured by CMS using $Z \rightarrow \mu^+\mu^-$ events with an FSR photon and are applied in the $H \rightarrow Z\gamma$ analysis. These SFs are catalogued in Table 6.1.

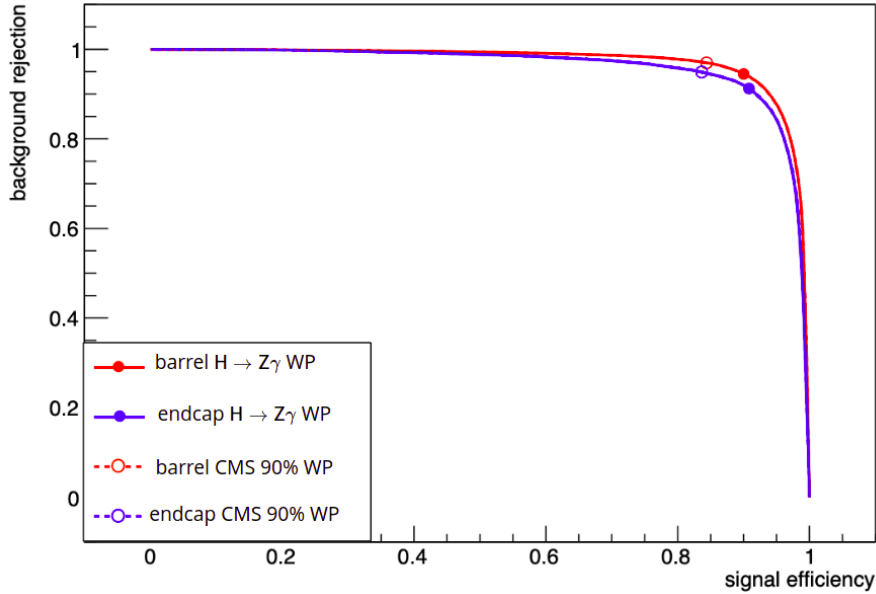


Figure 6.4. ROC curves for the corrected photon MVA ID in the barrel (red) and endcaps (blue). Here, signal refers to real photons from the $Z\gamma$ simulation and background refers to jets misreconstructed as photons from the $Z+jets$ simulation. Also shown are the cuts used for the $H \rightarrow Z\gamma$ analysis WP and for the standard CMS 90% WP.

Table 6.1. Photon conversion-safe electron veto SFs.

	barrel			endcap		
	0–30 GeV	30–60 GeV	60–200 GeV	0–30 GeV	30–60 GeV	60–200 GeV
2016		0.9938			0.9875	
2017		0.967			0.915	
2018	0.987613	0.98895	1.00006	0.95461	0.962451	0.99791

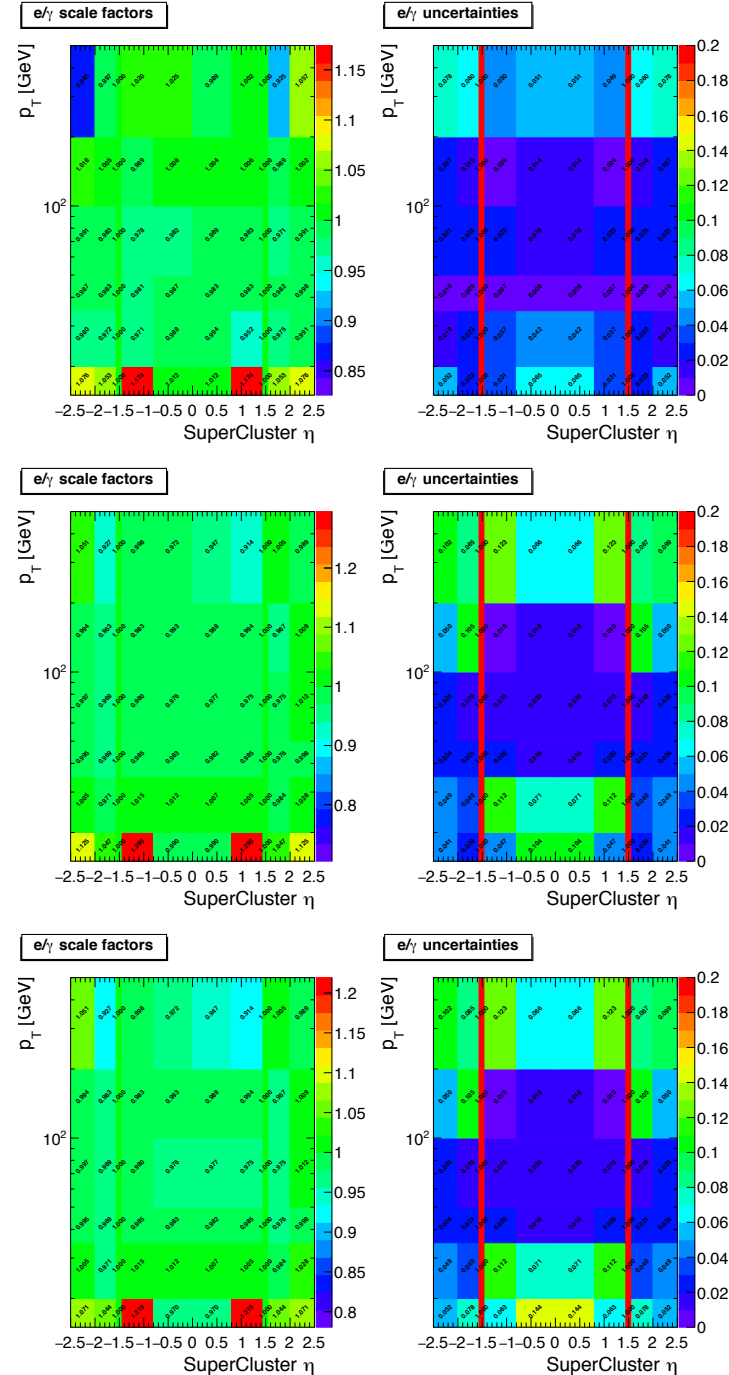


Figure 6.5. Left: Photon MVA ID efficiency SFs for 2016 (upper), 2017 (middle), and 2018 (lower). Right: The corresponding uncertainties for the SFs.

6.4. Electron Selection

Electrons are identified using a BDT discriminant (electron MVA ID) trained on Drell–Yan plus jets simulation, with prompt electrons matched to generator-level objects as signal and unmatched and non-prompt electrons as background. The features used in the BDT training include p_T , supercluster η , shower shape variables, ratio of hadronic to electromagnetic energy, track and pixel hit variables, and isolation variables [80]. Since isolation features are included in the training of the photon MVA ID, there is no need for a separate isolation requirement. For the $H \rightarrow Z\gamma$ analysis, an electron is selected if its photon MVA ID score is higher than a loose WP value, corresponding to 98% signal efficiency. In addition to the photon MVA ID cut, electrons must satisfy the impact parameter requirements $|d_{xy}| < 0.5$ cm and $|d_z| < 1$ cm with respect to the PV.

Electron MVA ID efficiencies and SFs are measured using a tag and probe method on dielectron events near the Z boson mass peak. The electrons used by this procedure are required to pass the single electron trigger with a p_T threshold of 27 (32) GeV for 2016 (2017 and 2018) data. The dielectron mass must be in the range 60–120 GeV. The tag electron must pass a tight cut-based electron ID and have $p_T > 30$ (35) GeV for 2016 (2017 and 2018) and $|\eta| < 2.5$. The probe electron is required to pass the loose electron MVA ID cut and the impact parameter cuts described above. Identification efficiencies and SFs are measured and applied in bins of p_T and supercluster η . The SFs for each data-taking year are shown in Fig. 6.6.

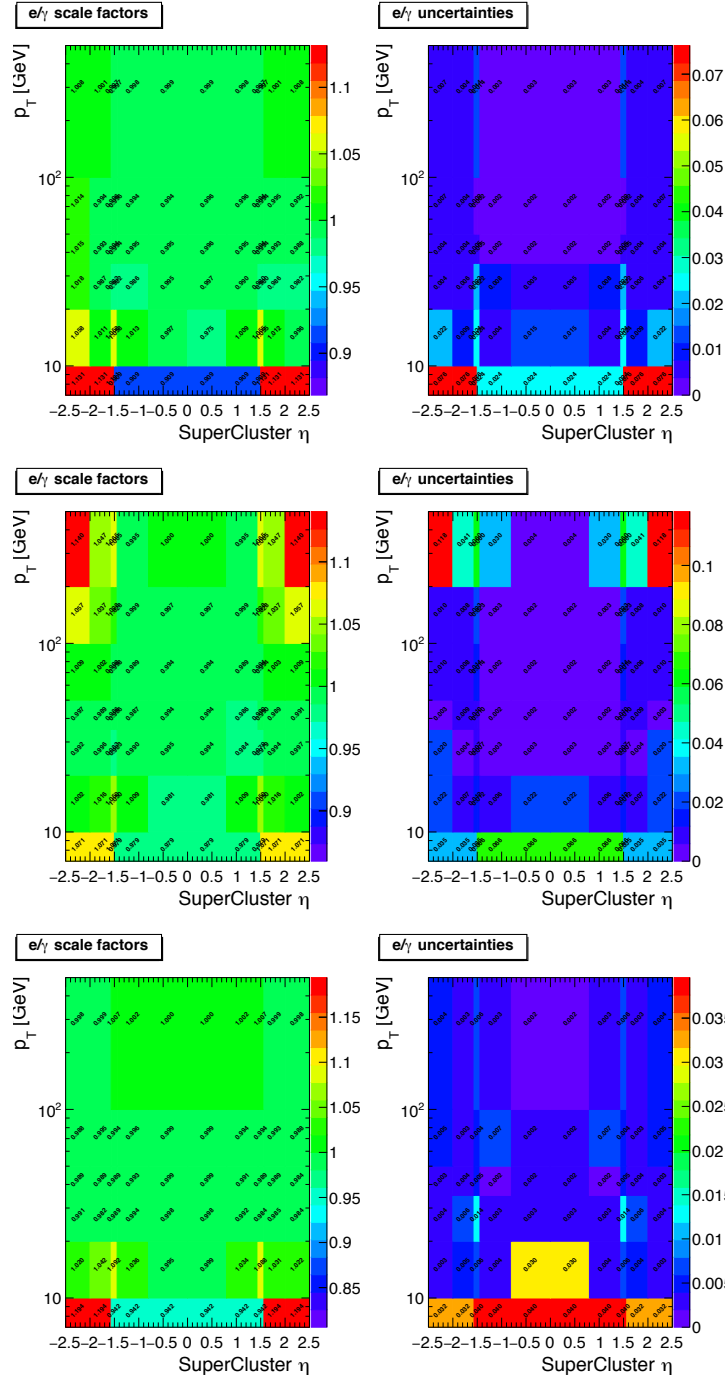


Figure 6.6. Left: Electron MVA ID efficiency SFs for 2016 (upper), 2017 (middle), and 2018 (lower). Right: The corresponding uncertainties for the SFs.

6.5. Muon Selection

A loose cut-based muon identification is used in this analysis. This ID was originally developed for the CMS $H \rightarrow ZZ^* \rightarrow 4\ell$ analysis of the 2016 data set [58] and is well-suited for $H \rightarrow Z\gamma$ due to the similar kinematics of the multiple muons in the final state. All muons are first required to pass a set of common ID cuts, followed by a separate set of cuts for high (> 200 GeV) and low p_T muons. All muons are required to satisfy $|\eta| < 2.4$, $|d_{xy}| < 0.5$ cm, and $|d_z| < 1$ cm, where the impact parameters are defined with respect to the PV using the best fit muon track. Additionally, the three-dimensional impact parameter with respect to the PV must have a magnitude less than four times its uncertainty. Muons are required to either be reconstructed as global muons or tracker muons. Those with standalone tracks only in the muon system are rejected. Low p_T muons satisfying the common requirements of the PF ID algorithm are selected. High p_T muons are selected if they pass the PF ID or if they pass the following high p_T requirements: the muon is matched to segments in at least two muon stations; satisfies $\frac{p_T}{\sigma_{p_T}} < 0.3$, $|d_{xy}| < 0.2$ cm, $|d_z| < 0.5$ cm; has at least one pixel hit; and has tracker hits in at least six tracker layers.

A relative PF isolation requirement is imposed, defined by the variable

$$(6.1) \quad \mathcal{I}^\mu \equiv \left[\sum p_T^{\text{charged}} + \max(0, \sum p_T^{\text{neutral}} + \sum p_T^\gamma - p_T^{\mu, \text{PU}}) \right] / p_T^\mu.$$

The quantity $\sum p_T^{\text{charged}}$ is the scalar sum of the p_T of charged hadrons originating from the PV, and $\sum p_T^{\text{neutral}}$ and $\sum p_T^\gamma$ are the scalar sums of the p_T of neutral hadrons and photons, respectively. The sums are over all PF candidates within a cone of radius $\Delta R = 0.3$ around the photon or lepton direction at the PV. Muons are required to satisfy

$\mathcal{I}^\mu < 0.35$. The ID and isolation efficiencies and SFs with uncertainties were measured and provided by the CMS $H \rightarrow ZZ^* \rightarrow 4\ell$ analysis working group.

In 2016, data-taking was affected by a problem in which the L1 trigger sent only one candidate per 60° sector instead of up to three [81]. As a result, when two muons in the same endcap had a low $\Delta\phi$ separation, only one would fire the trigger. To account for this, 2016 data events containing identified muons with $\Delta\phi < 70^\circ$ in the same endcap region are rejected.

6.6. Jet Selection

Jets are selected in order to categorize events coming from potential VBF Higgs production, but there is no jet multiplicity requirement for the $H \rightarrow Z\gamma$ event selection. In fact, the majority of simulation and data events selected in the analysis have no jets. However, identifying and selecting jets to categorize VBF events can still significantly improve the sensitivity of the search. Jets are required to pass a loose cut-based identification in 2016 and a tight cut-based identification in 2017 and 2018. Additionally, jets must satisfy $p_T > 30 \text{ GeV}$, $|\eta| < 4.7$, and $\Delta R > 0.4$ with respect to each lepton and the photon selected in the analysis. An issue with noise in the ECAL endcaps in 2017 [82] caused an artificial increase in jet multiplicity in data within a specific kinematic phase space. To mitigate this, jets are rejected if they have uncorrected $p_T < 50 \text{ GeV}$ and $2.65 < |\eta| < 3.139$. This cut reduces the efficiency to reconstruct dijet pairs by 12% in the specified region. To tag VBF events, we are interested in dijet pairs. If there are more than two jets satisfying the above criteria, only the two highest p_T jets are selected. No SFs are needed for these jet selection requirements as they do not impact the event selection.

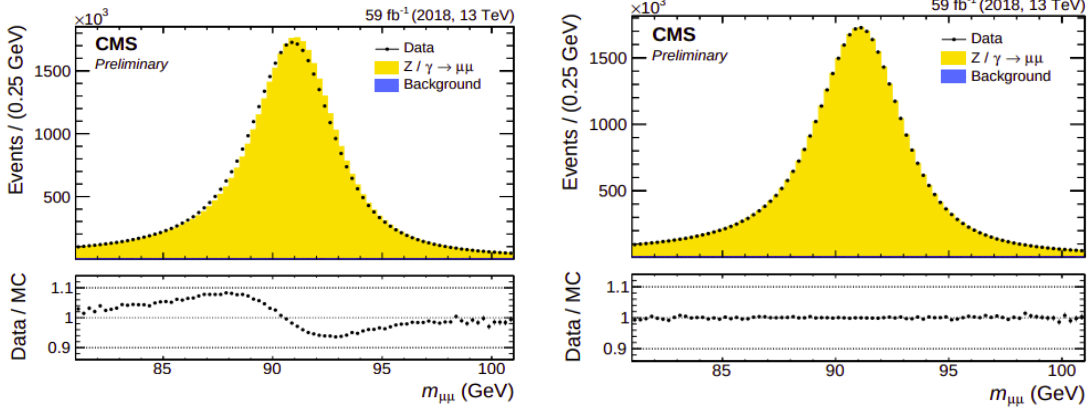


Figure 6.7. Dimuon invariant mass around the Z boson peak in 2018 data before (left) and after (right) the muon Rochester momentum corrections are applied [83].

6.7. Object Corrections

Several corrections are applied to the physics objects selected in the analysis. Rochester muon momentum scale and resolution corrections [83] are applied to both data and simulation. This greatly improves the calibration of the dimuon mass near the Z boson peak, as shown in Fig. 6.7. Energy scale and resolution corrections for electrons, photons, and jets are also applied in the analysis. The procedures for these corrections and the corresponding SFs for simulation are provided by CMS.

An FSR recovery procedure is performed for the selected muons, following a similar approach to that used in Ref. [58]. An FSR photon is identified and associated to its radiating muon based on the following criteria. The photon must satisfy $p_T > 2 \text{ GeV}$, $|\eta| < 2.4$, $\Delta R(\gamma, \mu)/p_{T\gamma}^2 < 0.012 \text{ GeV}^{-2}$, $\Delta R(\gamma, \mu) < 0.4$, and relative PF isolation smaller than 1.8, where the pileup contribution is excluded from the isolation calculation. If multiple FSR photons are associated to one muon, the photon with the smallest value of

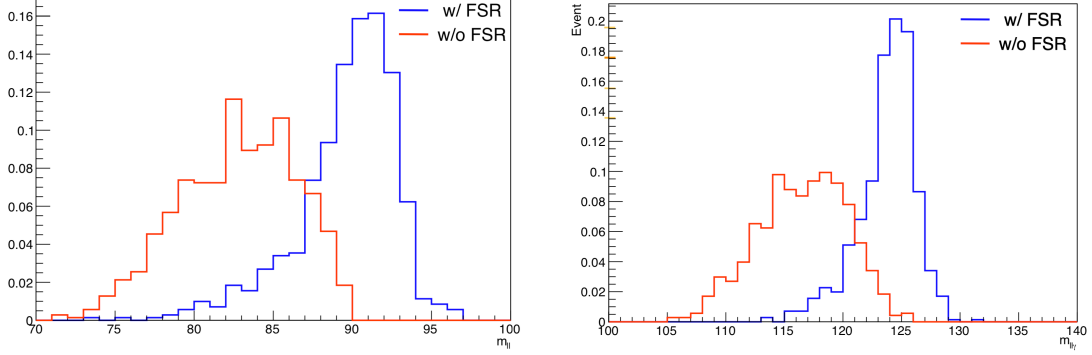


Figure 6.8. Dilepton invariant mass (left) and $\ell^+\ell^-\gamma$ invariant mass (right) with (blue) and without (red) FSR photon recovery for simulated $H \rightarrow Z\gamma \rightarrow \mu^+\mu^-\gamma$ events containing at least one FSR photon.

$\Delta R(\gamma, \mu)/p_{T\gamma}^2$ is selected. In simulation, we find that the selected FSR photon matches the generator level FSR photon with 93% efficiency. Figure 6.8 shows the dilepton and $\ell^+\ell^-\gamma$ invariant mass among FSR photon-containing signal events with and without applying the FSR recovery correction. The FSR recovery procedure improves the $m_{\ell^+\ell^-\gamma}$ resolution by 1% in the muon channel.

6.8. Event Selection

Events are required to contain a photon and at least two same-flavor, oppositely charged leptons ($\ell = e$ or μ) with $m_{\ell^+\ell^-} > 50$ GeV. The dilepton mass requirement, although relatively loose, is sufficient to suppress backgrounds that do not contain Z boson decays while retaining high signal efficiency. The particles used to reconstruct the $Z\gamma$ candidate system are required to have $p_T > 25$ (15) GeV for the leading (subleading) electron, $p_T > 20$ (10) GeV for the leading (subleading) muon, and $p_T > 15$ GeV for the photon. The photon must also satisfy $0 < |\eta| < 1.4442$ or $1.566 < |\eta| < 2.5$. This avoids the calorimeter transition region, in which photon reconstruction is more difficult. In

events with multiple dilepton pairs, the pair with mass closest to the nominal Z boson mass [4] is selected. Additional electrons (muons) with p_T greater than 7 (5) GeV are also used for categorization, as described in the next chapter.

The invariant mass of the $\ell^+\ell^-\gamma$ system is required to be in the range $105 < m_{\ell^+\ell^-\gamma} < 170$ GeV, which provides a broad range around the Higgs boson mass in which to perform the fit. Events are required to have a photon satisfying $p_T^\gamma/m_{\ell^+\ell^-\gamma} > 0.14$, which suppresses the Z+jets background without significantly reducing signal efficiency, with minimal bias in the $m_{\ell^+\ell^-\gamma}$ spectrum. Each lepton is required to have $\Delta R > 0.4$ with respect to the photon to reject events with FSR. To further reject FSR from Z γ processes, we require $m_{\ell^+\ell^-\gamma} + m_{\ell^+\ell^-} > 185$ GeV.

6.9. Kinematic Fit

A kinematic fit procedure is used to improve the dilepton mass and $m_{\ell^+\ell^-\gamma}$ resolutions, following a similar approach to that used in Ref. [58]. A maximum likelihood fit is performed, taking into account the true Z boson line shape, obtained from $H \rightarrow Z\gamma$ simulation, the p_T of each lepton, and the p_T resolution of each lepton. The outputs of this fit are the corrected p_T values for each lepton. The likelihood function for the fit is given by

$$(6.2) \quad \mathcal{L}(p_{T1}, p_{T2}|p_{T1}^R, \sigma_{p_{T1}}, p_{T2}^R, \sigma_{p_{T2}}) = \mathcal{N}(p_{T1}^R|p_{T1}, \sigma_{p_{T1}}) \cdot \mathcal{N}(p_{T2}^R|p_{T2}, \sigma_{p_{T2}}) \cdot \mathcal{L}(m_{12}|m_Z),$$

where \mathcal{N} represents the normal distribution, p_{T1}^R and p_{T2}^R are the reconstructed transverse momenta of the two leptons, $\sigma_{p_{T1}}$ and $\sigma_{p_{T2}}$ are the per-lepton transverse momentum

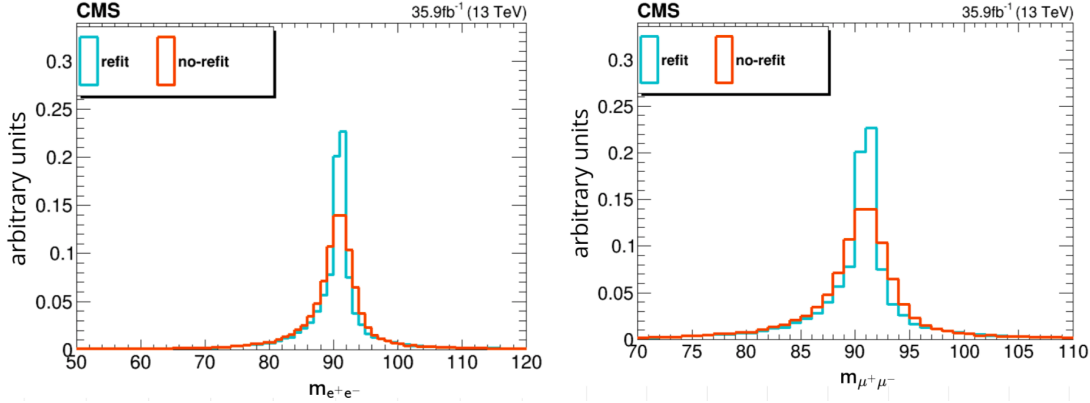


Figure 6.9. Dilepton invariant mass in 2016 data before and after the kinematic fit for the electron (left) and muon (right) channels.

resolutions, p_{T1} and p_{T2} are the corrected p_T values, m_{12} is the invariant mass calculated from p_{T1} and p_{T2} , and $\mathcal{L}(m_{12}|m_Z)$ is the likelihood given the true Z mass lineshape. The corrected p_T values are used to recalculate the dilepton mass and $m_{\ell^+\ell^-\gamma}$. Figure 6.9 shows the dilepton mass distributions before and after the kinematic fit. The improvement in signal $m_{\ell^+\ell^-\gamma}$ resolution varies with data-taking year and is between 20–27% in the electron channel and 10–12% in the muon channel. The effect of the kinematic fit is larger for the electron channel because of the poorer momentum resolution for electrons compared to muons.

6.10. Yields and Kinematic Distributions

Table 6.2 shows the number of expected $H \rightarrow Z\gamma$ signal events and the number of data events selected by the analysis, before any event categorization is done. The signal acceptance times efficiency ranges from 12–17% depending on the year and final state. Also shown are the event yields normalized by luminosity. We note that these are fairly

Table 6.2. Expected signal and data yields corresponding to each year of data-taking in the electron and muon channels.

	2016				2017				2018			
	Signal		Data		Signal		Data		Signal		Data	
	e	μ	e	μ	e	μ	e	μ	e	μ	e	μ
Total Events	200.2		475M	278M	239.1		266M	210M	384.4		1320M	300M
HLT	59.5	68.0	51.5M	96.8M	67.2	77.5	57.0M	92.8M	91.5	110	67.6M	100M
Selected Events	29.2	33.5	54.4k	67.4k	31.4	39.3	65.7k	83.1k	48.6	57.6	95.6k	117.6k
Selected Events/ fb^{-1}	0.80	0.93	1.50k	1.86k	0.76	0.95	1.58k	2.00k	0.81	0.96	1.60k	1.97k

consistent from year to year. The minor increase in selected data per unit luminosity from 2016 to 2018 is explained by increased pileup due to higher instantaneous luminosity.

Distributions of several basic kinematic quantities after selection are shown in Fig. 6.10. While the background for this analysis is estimated from data, it is still worth checking the agreement between data and background simulation for these quantities. We see that the level of agreement is good in all cases.

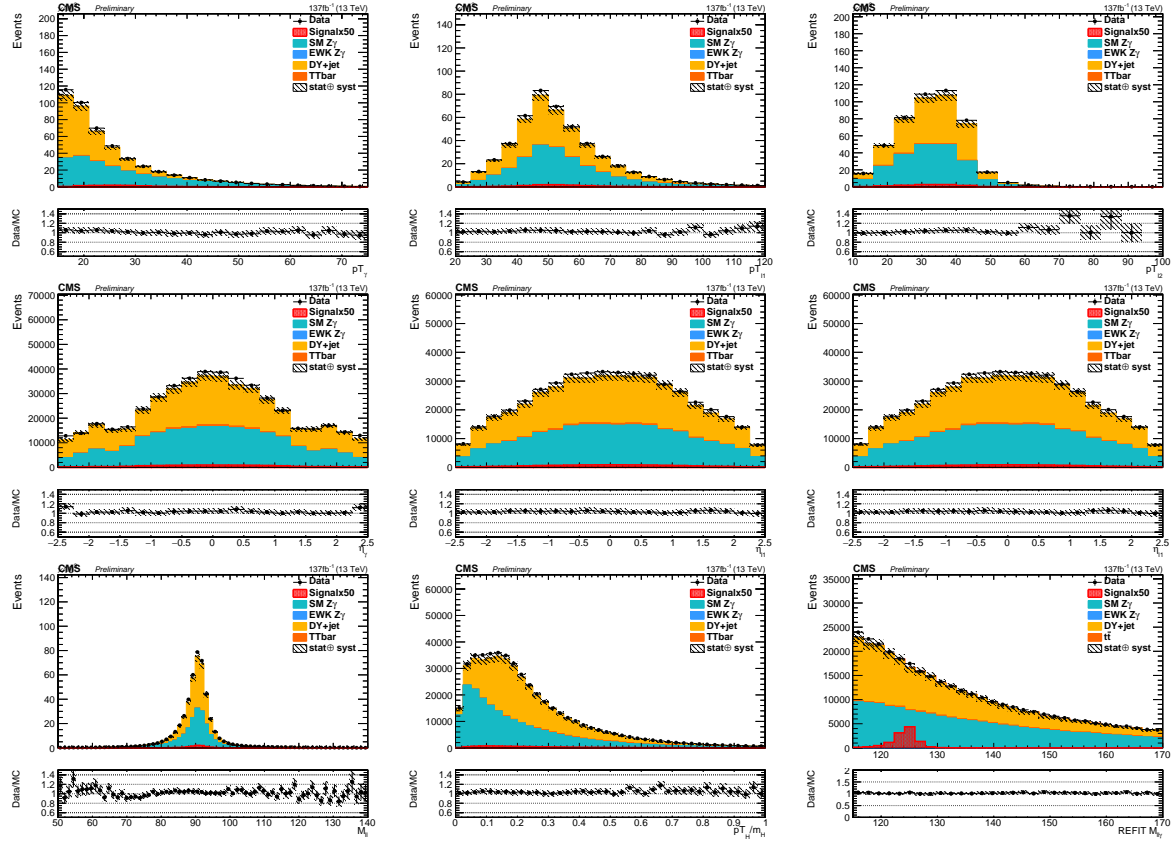


Figure 6.10. Basic kinematic distributions after event selection. The top (middle) row shows the $p_T(\eta)$ of the photon (left), leading lepton (middle), and trailing lepton (right). From left to right, the bottom row shows the dilepton mass, p_T/m of the $\ell^+\ell^-\gamma$ system, and corrected $m_{\ell^+\ell^-\gamma}$ after the kinematic fit is performed.

CHAPTER 7

Event Categorization

The sensitivity of the $H \rightarrow Z\gamma$ search can be significantly improved by leveraging the differences between signal events arising from different Higgs boson production mechanisms. In general, these production mechanisms have different final state topologies and kinematics. Mutually exclusive categories are defined in order to take advantage of this. In previously published CMS searches for $H \rightarrow Z\gamma$, cut-based approaches were used to define the categories. However, in the present analysis, the categorization strategy has been updated and improved using machine learning methods. The remainder of this chapter describes the categorization strategy in detail and summarizes the final categories used in the full Run 2 $H \rightarrow Z\gamma$ analysis.

The signal candidates from the VH and $t\bar{t}H$ production mechanisms are targeted using a lepton-tagged category, in which at least one electron or muon is present beyond those used to reconstruct the $Z\gamma$ system. The signal candidates from the VBF production mechanism are targeted by identifying events that have an additional dijet system. A BDT classifier (referred to as the VBF BDT) uses the properties of this dijet system to divide such events into a set of dijet categories. The VBF BDT discriminant value, transformed such that the VBF signal distribution is uniform, is denoted by \mathcal{D}_{VBF} . The signal candidates from the ggH production mechanism are targeted with events that do not fall within the lepton-tagged or dijet categories. A BDT classifier (referred to as

the kinematic BDT), trained on a set of kinematic variables, is used to further discriminate between signal and background events, defining a set of untagged categories. The kinematic BDT discriminant value, transformed such that the total signal distribution is uniform, is denoted by \mathcal{D}_{kin} .

7.1. Kinematic Boosted Decision Tree

The kinematic BDT is used to distinguish $H \rightarrow Z\gamma$ signal events from background events based on the kinematics of the leptons and photon in the $Z\gamma$ candidate system, as well as on the measured properties of these physics objects. It is trained using simulated $H \rightarrow Z\gamma$ signal events from all Higgs boson production modes described in Chapter 5 and background events from $Z\gamma$, $Z+\text{jets}$, $t\bar{t}$, and VBS $Z\gamma$. The training is restricted to use half of the simulated events, with the other half reserved for subsequent category optimization and signal $m_{\ell^+\ell^-\gamma}$ shape modeling. All training events are required to pass the object and event selection criteria described in Chapter 6. Events from 2016, 2017, and 2018 simulation samples in both the muon and electron channels are combined for training, weighted by their respective cross sections and by the recorded integrated luminosity of each data-taking year.

7.1.1. Training Features

The choice of training variables (features) for the kinematic BDT is guided by existing theoretical physics knowledge, categorization strategies in the prior $H \rightarrow Z\gamma$ analyses, and empirical methods. From a theoretical perspective, the decay angles between the final state particles are known to provide some discriminating power between signal and

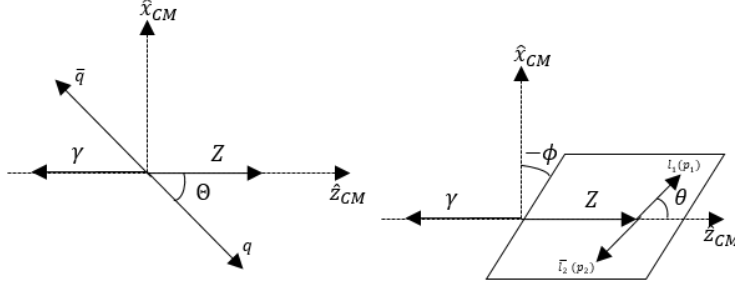


Figure 7.1. Definitions of theoretical angles used for kinematic BDT training. The left diagram is in the Higgs boson center-of-mass frame, and the right diagram is in the Z boson center-of-mass frame.

background. These angular features, described in Refs. [84, 85], include $\cos\Theta$, $\cos\theta$, and ϕ , where Θ is the production angle of the Z boson in the Higgs boson center-of-mass frame, and θ and ϕ are the polar and azimuthal decay angles of the leptons in the Z boson center-of-mass frame, respectively. Figure 7.1 shows how these angles are defined, and Fig. 7.2 shows the theoretical and reconstructed distributions of these quantities. Based on the theoretical distributions, these angular features are expected to offer good discriminating power between signal and background. However, it must be noted that the discriminating power is reduced for the final reconstructed quantities, since these angles are highly correlated with other analysis selection requirements, such as the mass cuts.

Several fundamental kinematic quantities of the final state particles are also used as training features. These include the pseudorapidity of each lepton, the ΔR between each lepton and the photon, and the p_T/m of the $\ell^+\ell^-\gamma$ system. We note that the p_T values of each final state particle were also considered for training, but were found to have a negligible impact on discrimination power. This is likely because they are highly correlated with these other fundamental kinematic quantities, and thus, do not

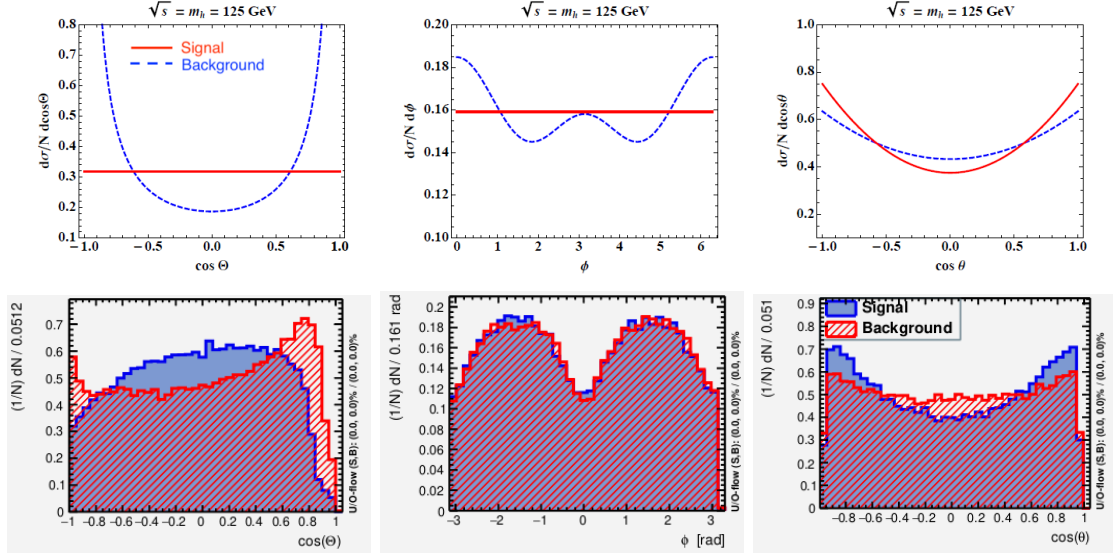


Figure 7.2. Top: Expected theoretical shapes [84] for the angular features used for kinematic BDT training. Bottom: Reconstructed shapes for these quantities after the $H \rightarrow Z\gamma$ selection requirements have been applied. Please note that the red and blue color conventions are reversed for the top and bottom plots.

introduce much additional information to the BDT model. A comparison between signal and background shapes for these kinematic features is shown in Fig. 7.3.

Finally, training features related to the quality of the final state photon are used. These include the corrected photon MVA ID score and the photon energy resolution. There are several motivations for these features. First, they are important for distinguishing $H \rightarrow Z\gamma$ signal events from the large $Z+jets$ background, where a jet is misreconstructed as a photon. Second, they are inspired by the previous CMS $H \rightarrow Z\gamma$ searches, which used photon pseudorapidity and R_9 for categorization. In our current analysis, the photon R_9 was also considered as a training feature. However, it did not contribute any meaningful

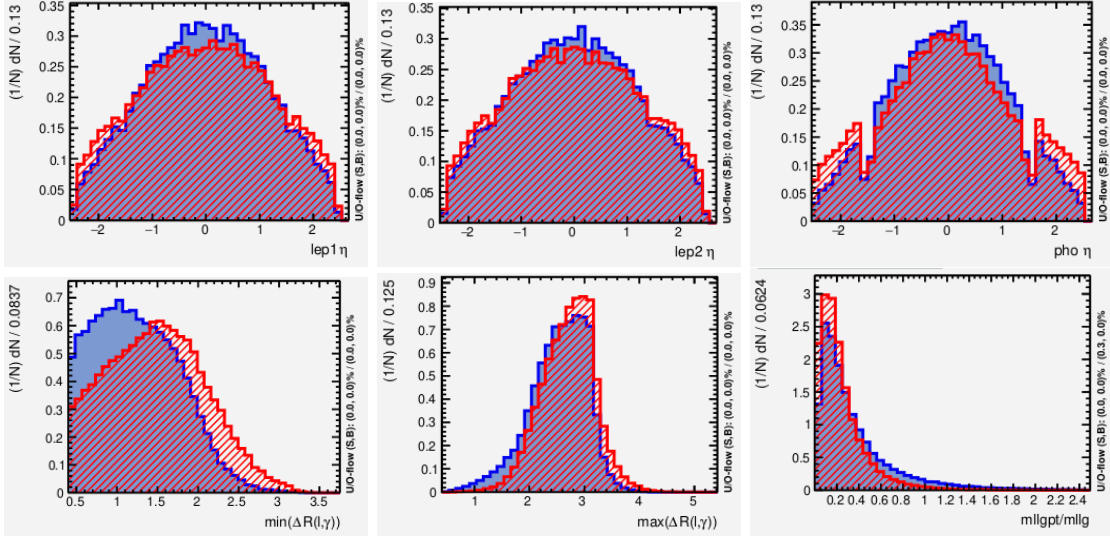


Figure 7.3. Comparison of reconstructed signal and background shapes for several kinematic variables used for kinematic BDT training. The blue histograms represent the signal, while the red histograms represent the background.

additional discriminating power. This is likely because the R_9 is already part of the corrected photon MVA ID. Figure 7.4 shows the comparison between signal and background shapes for these features after the full set of $H \rightarrow Z\gamma$ selection requirements has been applied. Both features offer strong discrimination power, particularly the corrected photon MVA ID score. However, we note that this is partially by construction, since a very loose photon MVA ID cut was applied in order to preserve maximal information for the kinematic BDT training.

Since the kinematic BDT training is carried out using simulated events, it is necessary to check that the simulation accurately models the training feature distributions in data. A comparison of data to simulation, combining all years of data-taking in both the electron and muon channels, is shown in Fig. 7.5. We observe good agreement between data and simulation for all kinematic BDT training features.

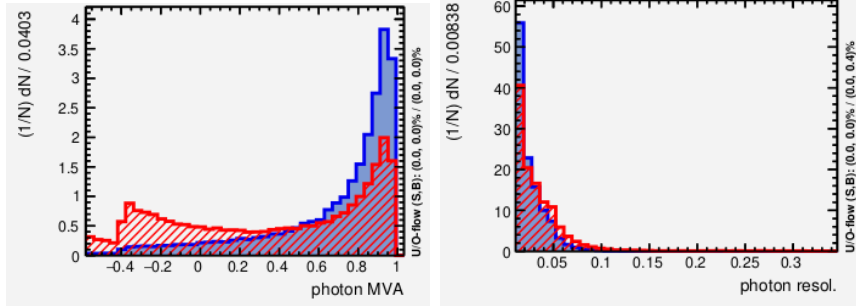


Figure 7.4. Comparison of reconstructed signal and background shapes for the photon quality features used for kinematic BDT training. The blue histograms represent the signal, while the red histograms represent the background.

7.1.2. Training Results

The output kinematic BDT shapes for signal and background are shown in Fig. 7.6. No overtraining is observed, as evidenced by the similarity between training and test distributions. The importance of each training feature for the discrimination power of the final kinematic BDT discriminant is given in Table 7.1. We see that the corrected photon MVA score is the most discriminating feature, since it distinguishes real photons from misreconstructed jets. The variable $p_T^{\ell^+\ell^-\gamma}/m_{\ell^+\ell^-\gamma}$ also contributes good discrimination power, and effectively replaces the need for a boosted Higgs category, as was used in the CMS 2016 search.

7.2. Vector Boson Fusion Boosted Decision Tree

The VBF BDT is used to discriminate signal events arising via the VBF Higgs production mechanism from other sources of signal and background events. The training and evaluation of the VBF BDT is carried out on events that have two jets selected according to the requirements in Chapter 6. Signal events for training are taken from the simulated

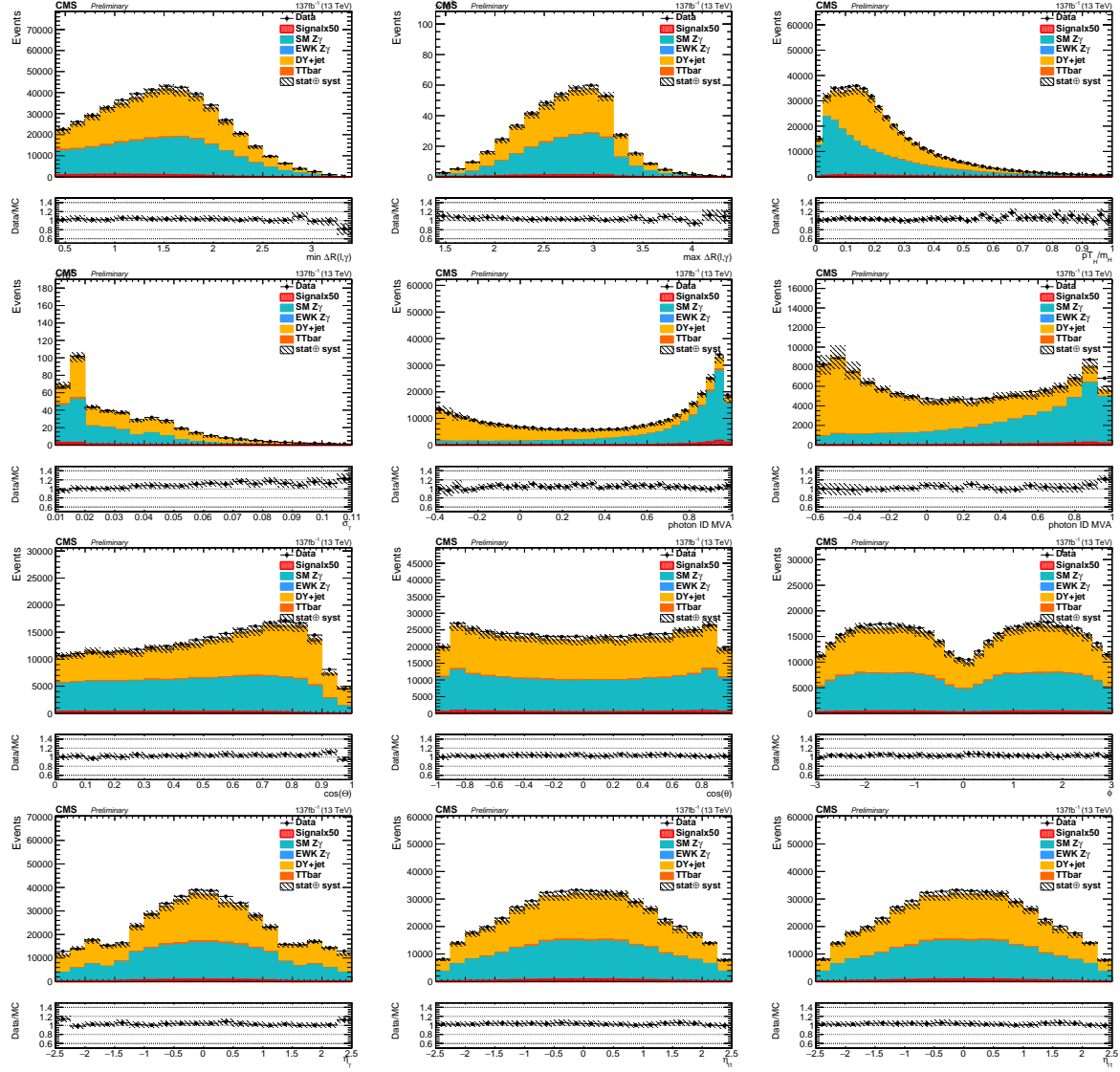


Figure 7.5. Comparison of data and simulation for the kinematic BDT training features. The plotted distributions include data and simulated samples from the combination of the three data-taking years in both the electron and muon channels.

VBF $H \rightarrow Z\gamma$ samples, while ggH $H \rightarrow Z\gamma$, $Z\gamma$, $Z+jets$, and $t\bar{t}$ events are considered background. Due to their very small contribution, VH and $t\bar{t}H$ $H \rightarrow Z\gamma$ events are neglected. Only about 65% of the selected jets from the VBF signal correspond to the true

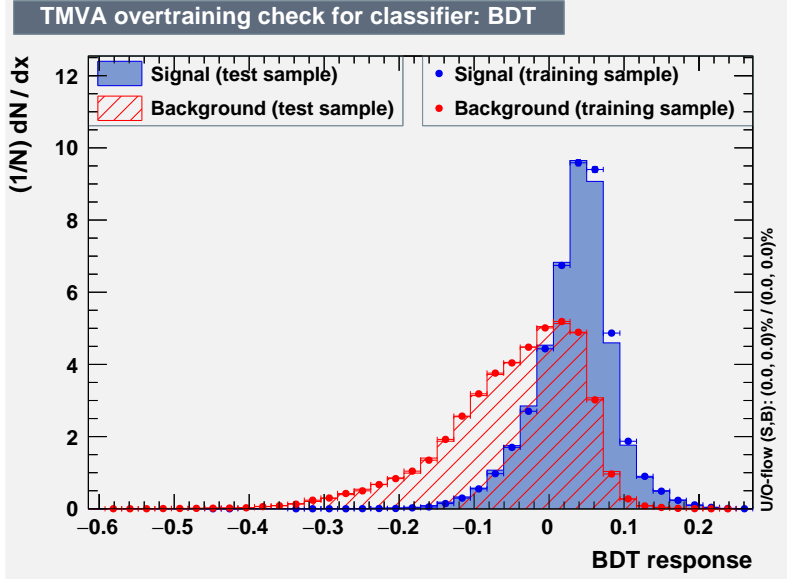


Figure 7.6. Shapes of the kinematic BDT distributions for signal and background for both training and test sets. No BDT overtraining is observed.

Variable	Variable Importance (%)
corrected photon MVA score	12.8
$\min(\Delta R(\ell, \gamma))$	12.0
$p_T^{\ell^+ \ell^- \gamma} / m_{\ell^+ \ell^- \gamma}$	10.2
$\cos \Theta$	10.0
$\frac{\sigma_\gamma}{E_\gamma}$	9.1
$\cos \theta$	8.2
$\max(\Delta R(\ell, \gamma))$	8.1
$\eta_{\ell 2}$	8.1
$\eta_{\ell 1}$	7.9
η_γ	7.2
ϕ	6.2

Table 7.1. Importance of the kinematic BDT training features.

VBF jets in which we are interested. Because of this, we perform an additional matching procedure for these jets. In order for a VBF signal event to be used in the training, both reconstructed jets must be matched to generator-level partons, which must, in turn,

be matched to the generator-level p_T values of the true VBF partons. Only half of the simulated events are used for the training procedure, with the remainder used for category optimization and signal $m_{\ell^+\ell^-\gamma}$ shape modeling. Events from all three data-taking years in both the muon and electron channels are combined for training, weighted by the respective cross sections and by the recorded integrated luminosity of each data-taking year.

7.2.1. Training Features

The training features used for the VBF BDT include quantities that distinguish events with the VBF topology from other types of events, as well as quantities that distinguish signal from background based on kinematics. Since the categorization strategy treats dijet jets separately from other types of events, including these kinematic variables is not redundant with the kinematic BDT described above. The two variables used for kinematic separation of signal and background for the VBF BDT are the kinematic BDT score and the variable p_T^t , defined in Chapter 4. Because the kinematics of the two leptons and photon are similar for VBF signal events and other signal production mechanisms, the previously trained kinematic BDT is expected to yield good discrimination power between VBF signal and backgrounds. By introducing the variable p_T^t , we add another feature sensitive to boost of the Higgs boson. This takes advantage of the recoil of the Higgs boson against the jets, and along with the p_T/m in the kinematic BDT, replaces the need for a boosted category. Signal and background shapes for the kinematic BDT score and p_T^t are shown in Fig. 7.7, where background refers to the full training background, including ggH $H \rightarrow Z\gamma$ events.

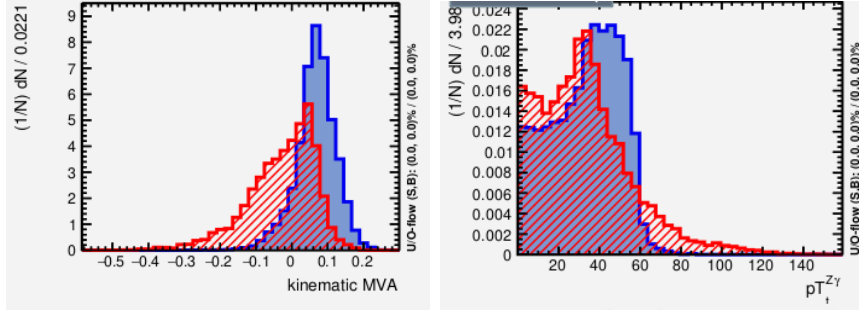


Figure 7.7. Comparison of signal and background shapes for the kinematic features used for VBF BDT training. The blue histograms represent the VBF signal, while the red histograms represent the training background, including ggH $H \rightarrow Z\gamma$ events.

We also include training features that aim to distinguish VBF events from non-VBF events, using information about the jets. These include (i) the difference in pseudorapidity between the two jets; (ii) the difference in azimuthal angle between the two jets; (iii) the photon Zeppenfeld variable [86] ($\eta_\gamma - (\eta_{j_1} + \eta_{j_2})/2$), where η_γ, η_{j_1} and η_{j_2} are the pseudorapidities of the photon, leading jet, and subleading jet, respectively; (iv) the ratio between the p_T of the $Z\gamma j_1 j_2$ system and the corresponding scalar sum of momenta ($|\sum_{Z\gamma j_1 j_2} \vec{p}_T| / \sum_{Z\gamma j_1 j_2} p_T$); (v) the difference in azimuthal angle between the dijet system and the $Z\gamma$ system; (vi) the p_T of each jet; and (vii) the ΔR separation between each jet and the photon. Other training features were also tried, including the individual pseudorapidities of the jets and the Zeppenfeld variable for the $Z\gamma$ system. However, these features were not included, as they offered negligible improvement for the final trained model. Signal and background shape comparisons for the above variables are shown in Fig. 7.8.

Since the VBF BDT training is carried out using simulated events, it is necessary to check that the simulation accurately models the training feature distributions in data. A

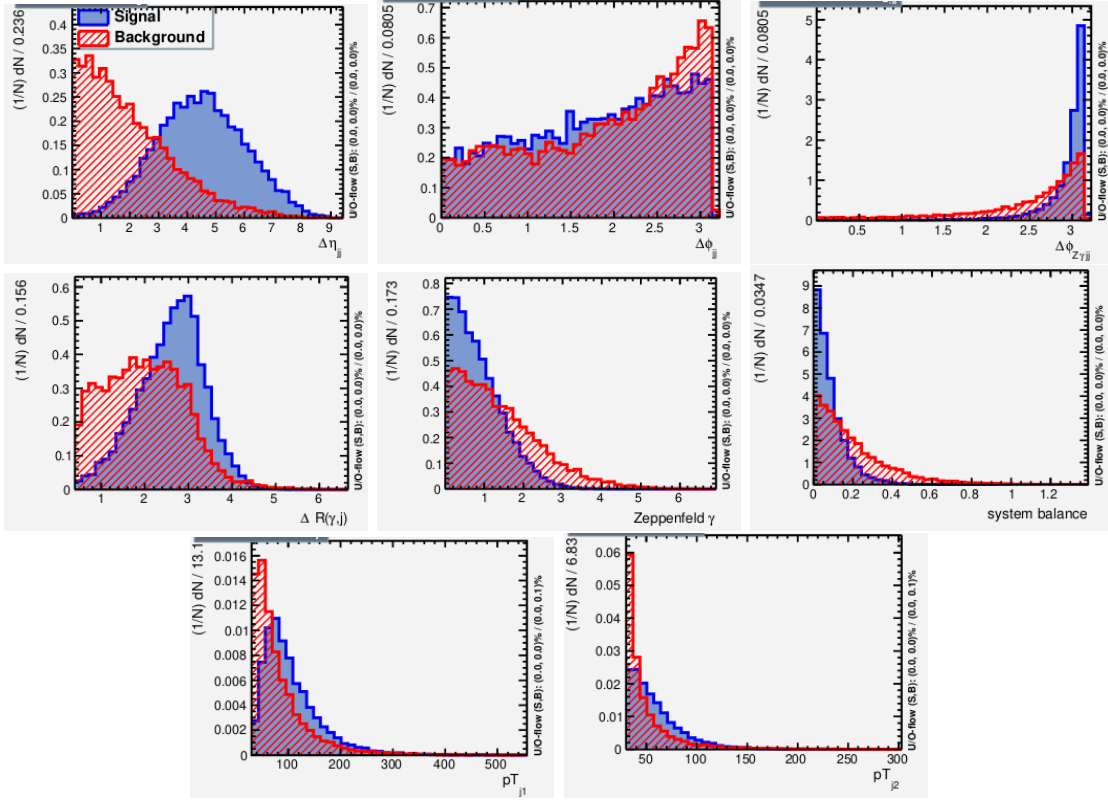


Figure 7.8. Comparison of signal and background shapes for several variables used for VBF BDT training. The blue histograms represent the VBF signal, while the red histograms represent the training background, including ggH $H \rightarrow Z\gamma$ events.

comparison of data to simulation, combining all years of data-taking in both the electron and muon channels, is shown in Fig. 7.9. We observe good agreement between data and simulation for all VBF BDT training features.

7.2.2. Training Results

The output VBF BDT shapes for signal and background are shown in Fig. 7.10. No overtraining is observed, as evidenced by the similarity between training and test distributions. The importance of each training feature for the discrimination power of the final

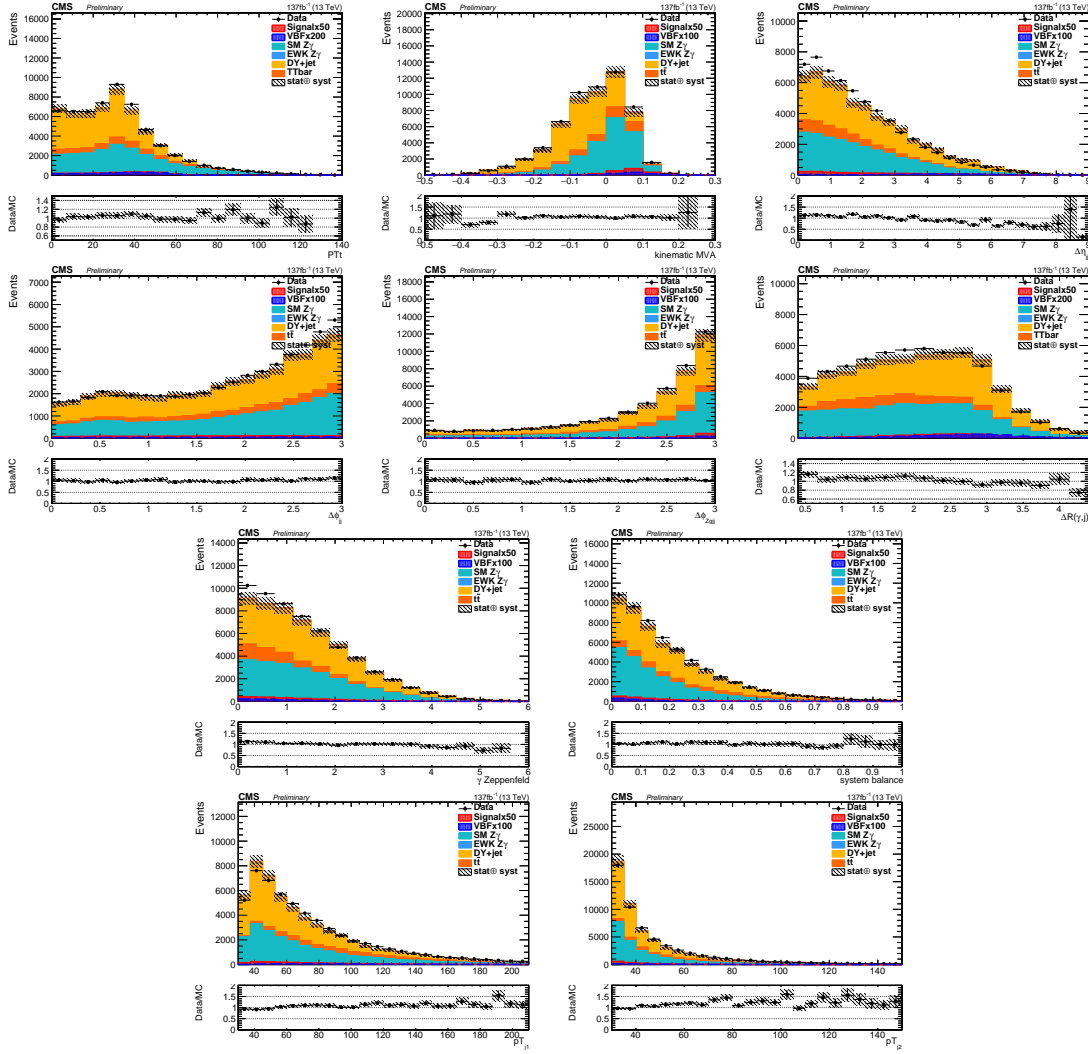


Figure 7.9. Comparison of data and simulation for the VBF BDT training features. The plotted distributions include data and simulated samples from the combination of the three data-taking years in both the electron and muon channels.

VBF BDT discriminant is given in Table 7.2. We see that the most important feature is the $\Delta\eta$ between the jets, followed by the kinematic BDT score and quantities relating the dijet system to the $Z\gamma$ system.

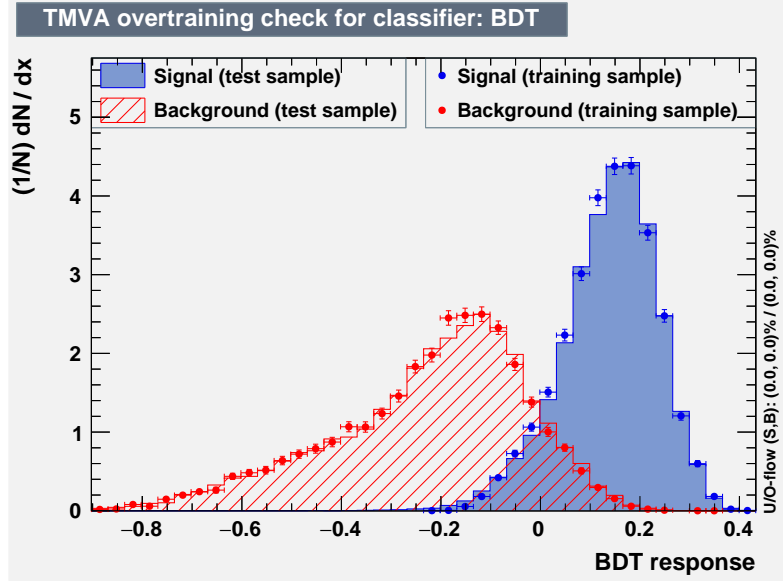


Figure 7.10. Shapes of the VBF BDT distributions for signal and background for both training and test sets. No BDT overtraining is observed.

Variable	Variable Importance (%)
$ \Delta\eta(j_1, j_2) $	15.9
kinematic BDT score	12.3
$ \Delta\phi(Z\gamma, j_1 j_2) $	11.7
$ \sum_{Z\gamma j_1 j_2} \vec{p}_T / \sum_{Z\gamma j_1 j_2} p_T $	11.4
p_T^t	10.7
$ \Delta\phi(j_1, j_2) $	10.4
$ \eta_\gamma - \frac{\eta_{j_1} + \eta_{j_2}}{2} $	8.6
$p_T^{j_2}$	7.8
$p_T^{j_1}$	6.2
$\Delta R(\gamma, j)$	5.0

Table 7.2. Importance of the VBF BDT training features.

7.3. Categorization Procedure

The procedure used for event categorization is described below.

- (1) Events with at least one additional electron (muon) with $p_T > 7$ (5) GeV are assigned to the lepton-tagged category.

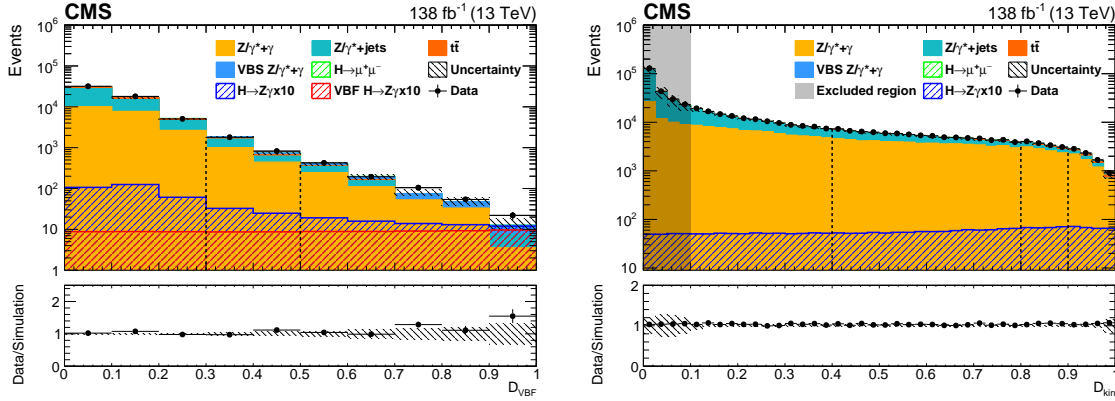


Figure 7.11. The \mathcal{D}_{VBF} (left) and \mathcal{D}_{kin} (right) distributions for signal, simulated background, and data. The \mathcal{D}_{VBF} distribution includes only dijet-tagged events, and the \mathcal{D}_{kin} distribution includes only untagged events. The sum of contributions from all signal production mechanisms is shown by the blue line, while the contribution from only the VBF mechanism is shown by the red line. The uncertainty band incorporates all statistical and systematic uncertainties in the expected background. The dashed lines indicate the boundaries for the dijet and untagged categories. The gray shaded region in the \mathcal{D}_{kin} distribution is excluded from the analysis.

- (2) Events not assigned to the lepton-tagged category, but which contain two jets satisfying the selection requirements described in Chapter 6, are classified as dijet events, indicative of possible VBF production. The subdivision of dijet events into a set of three dijet categories using the VBF BDT is described below.
- (3) Events not assigned to the lepton-tagged or dijet categories are classified as untagged events. The subdivision of untagged events into a set of four untagged categories using the kinematic BDT is described below.

Distributions of the transformed VBF BDT score (\mathcal{D}_{VBF}) and transformed kinematic BDT score (\mathcal{D}_{kin}) are shown in Fig. 7.11. The subdivision of dijet and untagged events into categories is based on these distributions. Category boundaries are defined as mutually exclusive regions of \mathcal{D}_{VBF} and \mathcal{D}_{kin} . The locations of the boundaries defining the categories

Table 7.3. Summary of the category definitions. The lepton-tagged category requires at least one additional electron or muon. Dijet categories are defined by regions of \mathcal{D}_{VBF} and untagged categories are defined by regions of \mathcal{D}_{kin} .

Lepton	Dijet 1	Dijet 2	Dijet 3	Untagged 1	Untagged 2	Untagged 3	Untagged 4
	\mathcal{D}_{VBF} selection			\mathcal{D}_{kin} selection			
$\geq 1 \text{ e}, \mu$	0.5–1.0	0.3–0.5	0.0–0.3	0.9–1.0	0.8–0.9	0.4–0.8	0.1–0.4

are optimized by iterating over all possible combinations of boundaries using $\sum_{i=1}^n S_i^2 / B_i$ as a figure-of-merit. The variables S_i and B_i represent the number of expected signal and background events in the i^{th} category, and n is the total number of categories. We consider categories with boundaries corresponding to signal efficiencies between 0 and 100% in 10% increments. This optimization procedure results in three dijet categories and four untagged categories. The lowest \mathcal{D}_{kin} boundary corresponds to the 10% point in integrated signal efficiency, and events below the 10% point are excluded from the analysis to preserve the stability of the background model.

The full categorization and optimization procedure results in the following eight mutually exclusive categories: one lepton-tagged category, three dijet categories, and four untagged categories. The category definitions are summarized in Table 7.3.

Table 7.4 lists the event categories used in the analysis, along with the expected event yields for an $m_H = 125.38 \text{ GeV}$ signal arising from ggH, VBF, VH, and $t\bar{t}H$ production, as well as the resonant background contribution from FSR from $H \rightarrow \mu^+ \mu^-$, which is 3–8% of the $H \rightarrow Z\gamma$ yield, depending on the category. Event yields from other Higgs backgrounds such as $H \rightarrow \tau^+ \tau^-$ and $H \rightarrow \gamma\gamma$ are estimated to be below the 1% level relative to the $H \rightarrow Z\gamma$ yield and are neglected. The dominant contribution to the signal yield is generally from ggH production, except in the lepton-tagged category, in which

Table 7.4. Yields and approximate significance (S/\sqrt{B}) for each category, where S and B are the expected number of signal and background events in the narrowest $m_{\ell^+\ell^-\gamma}$ interval containing 95% of the expected signal distribution. Also shown is the $m_{\ell^+\ell^-\gamma}$ resolution, computed using the narrowest interval containing 68% of the expected signal distribution.

	138 fb^{-1}	Lepton	Dijet 1	Dijet 2	Dijet 3	Untagged 1	Untagged 2	Untagged 3	Untagged 4
SM signal yield									
ggH	0.51	e^+e^- $\mu^+\mu^-$	1.10 1.41	1.62 2.05	9.44 12.1	6.89 8.52	7.35 9.17	29.8 38.0	22.5 29.0
VBF	0.09	e^+e^- $\mu^+\mu^-$	1.94 2.40	0.76 0.97	1.13 1.43	0.71 0.89	0.35 0.43	0.92 1.18	0.51 0.65
VH + t̄H	1.84	e^+e^- $\mu^+\mu^-$	0.04 0.05	0.13 0.16	1.89 2.36	0.31 0.39	0.17 0.21	0.45 0.57	0.27 0.33
SM resonant background									
$H \rightarrow \mu^+\mu^-$	0.14	$\mu^+\mu^-$	0.27	0.27	0.43	0.62	0.49	2.02	1.78
Mass resolution (GeV)	2.12	e^+e^- $\mu^+\mu^-$	1.91 1.52	2.06 1.61	2.15 1.72	1.80 1.37	1.97 1.42	2.12 1.62	2.33 1.83
Data yield	1485		168	589	11596	1485	1541	2559	17608
S/\sqrt{B}	0.06		0.54	0.24	0.26	0.45	0.35	0.53	0.30

VH and t̄H events dominate, and in the dijet 1 category, in which VBF events dominate. The categorization procedure increases the sensitivity of the analysis by 24% with respect to an inclusive event selection.

CHAPTER 8

Statistical Analysis

The signal search is performed using a simultaneous fit to the $m_{\ell^+\ell^-\gamma}$ distribution in the eight event categories. The fit uses a binned maximum likelihood method in the range $105 < m_{\ell^+\ell^-\gamma} < 170 \text{ GeV}$. In each category, a likelihood function is defined using analytic models of signal and background events, along with nuisance parameters for systematic uncertainties. The combined likelihood function is the product of the likelihood functions in each category. The parameter of interest in the maximum likelihood fit is the signal strength μ , defined as the product of the cross section and the branching fraction $[\sigma(pp \rightarrow H)\mathcal{B}(H \rightarrow Z\gamma)]$, relative to the SM expectation.

8.1. Signal Modeling

The signal model is defined as the sum of Crystal Ball [87] and Gaussian functions. The signal shape parameters are determined by fitting this model to simulated signal events in each category. To account for differences in mass resolution, these fits are performed separately for the event samples used to model each data-taking year, as well as for muon and electron channel events. This results in six signal models that are summed to give the total expected signal in a given category. Table 7.4 gives these mass resolutions for $H \rightarrow Z\gamma$, summed over the three years, as obtained from simulation. The mass resolutions range from 1.4–2.3 GeV, depending on the category. Separate sets of parameter values are found by fitting simulated events with m_H of 120, 125, and 130 GeV. Using linear

interpolation, parameter values are also determined at 1 GeV intervals in m_H from 120–130 GeV, as well as at 125.38 GeV. In the fit to data, the mean and resolution parameters are allowed to vary subject to constraints from several systematic uncertainties, described in Section 9, while the remaining parameters are held fixed.

Figure 8.1 (8.2) shows the signal fits for the $m_H = 125$ GeV simulated samples in the electron (muon) channel for the 2016 data-taking period. Figure 8.3 shows the signal fits for the lepton-tagged category for the 2016 data-taking period, in which electron and muon channel events are combined. In the lepton-tagged category, the signal shape is modeled separately for ZH and WH production in order to account for differences in potential lepton mispairing. Signal fits for the full set of data-taking periods are shown in Appendix B.

8.2. Resonant Background Modeling

The process $H \rightarrow \mu^+ \mu^-$, where at least one muon radiates an FSR photon, is expected to contribute at the 6% level relative to the $H \rightarrow Z\gamma$ signal yield. Because of this, we treat it as a resonant background. To model the $H \rightarrow \mu^+ \mu^-$ shape, we perform fits to the $m_{\ell^+\ell^-\gamma}$ distributions in simulated event samples, following the same procedure used for the signal fits described above. As for the signal, the analytic model is taken to be the sum of Crystal Ball and Gaussian functions. The resulting fits are shown in Appendix C.

8.3. Nonresonant Background Modeling

The nonresonant background model in each category is obtained from the data using the discrete profiling method [88]. This technique accounts for the systematic uncertainty associated with choosing an analytic functional form to fit the background. The

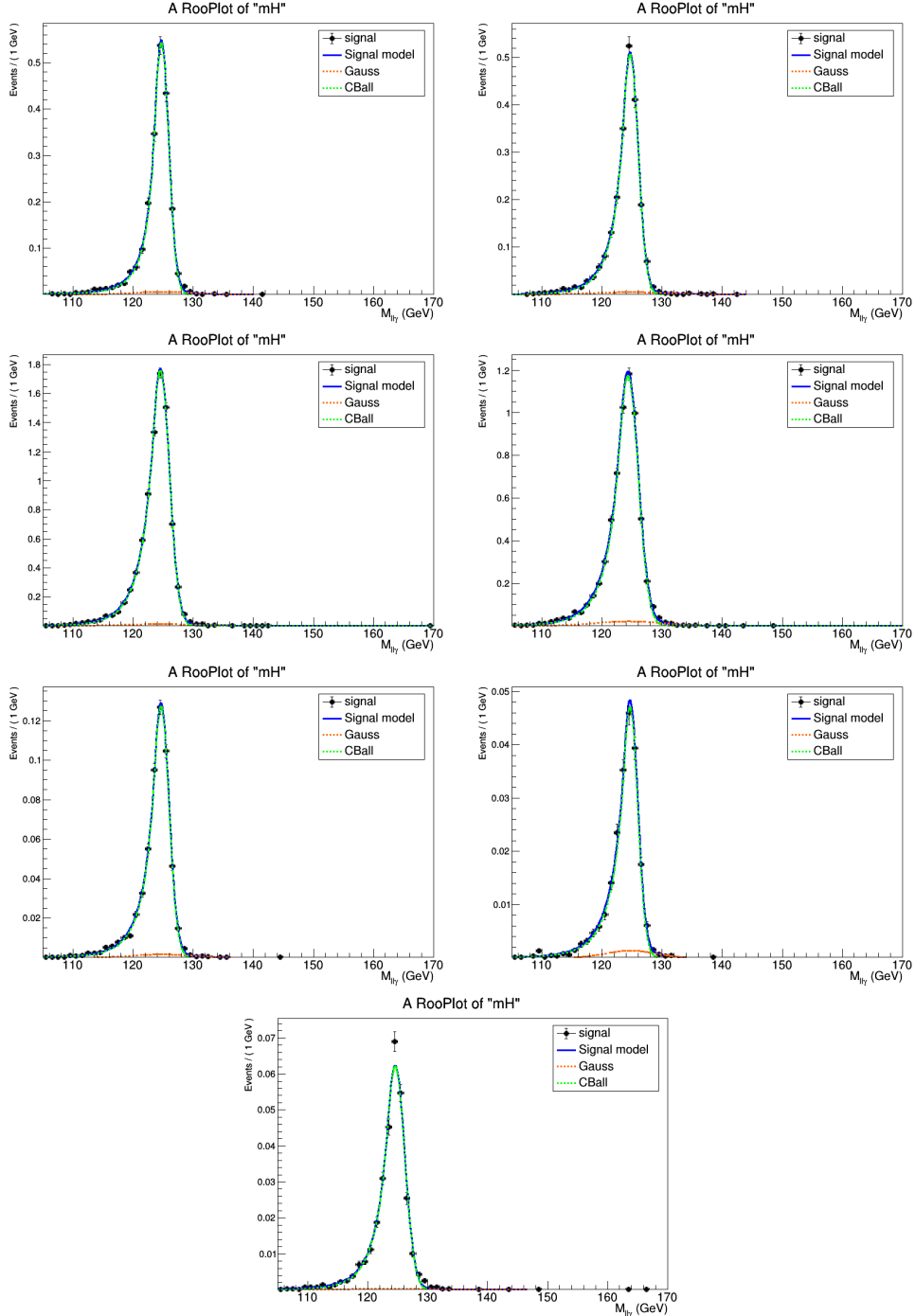


Figure 8.1. Fits to simulated $m_{\ell^+\ell^-\gamma}$ signal distributions in the electron channel for $m_H = 125$ GeV for the 2016 data-taking period. The blue line shows the total fit function, the green line shows the Crystal Ball function component, and the red line shows the Gaussian function component. The top four plots correspond to the untagged categories, and the bottom three plots correspond to the dijet categories.

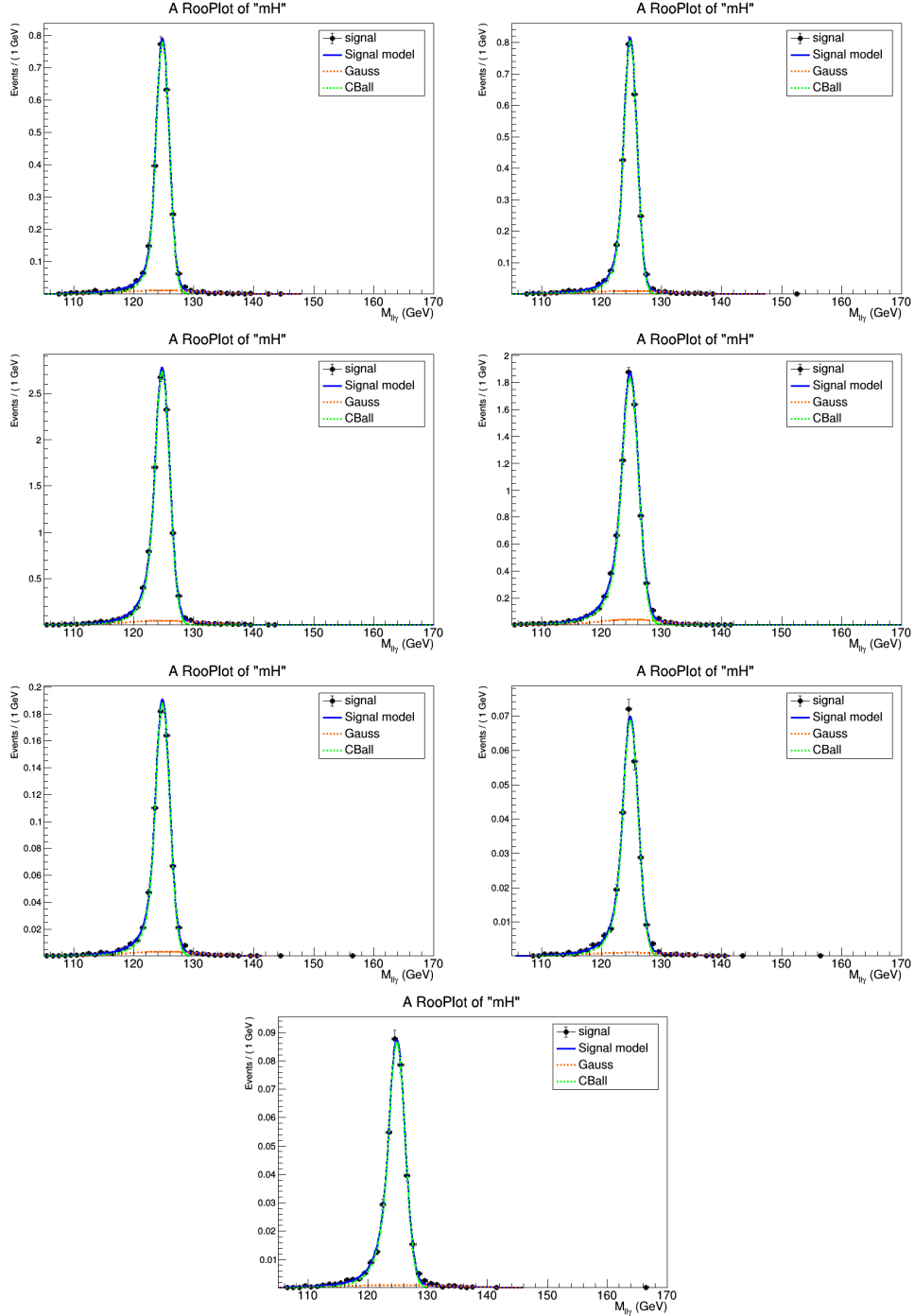


Figure 8.2. Fits to simulated $m_{\ell^+\ell^-\gamma}$ signal distributions in the muon channel for $m_H = 125$ GeV for the 2016 data-taking period. The blue line shows the total fit function, the green line shows the Crystal Ball function component, and the red line shows the Gaussian function component. The top four plots correspond to the untagged categories, and the bottom three plots correspond to the dijet categories.

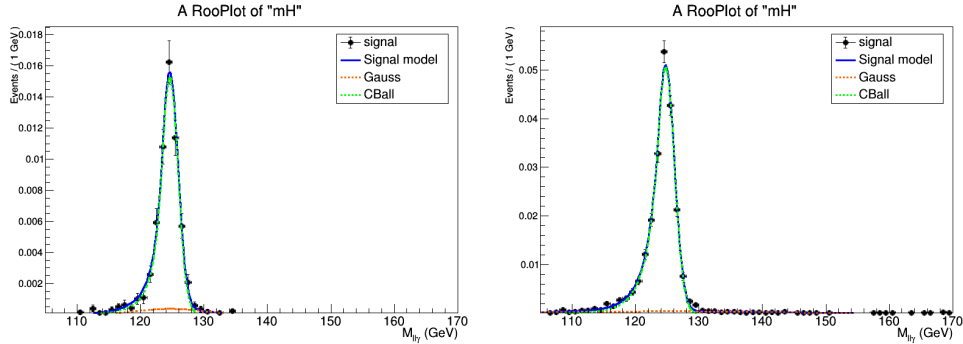


Figure 8.3. Fits to simulated $m_{\ell^+\ell^-\gamma}$ signal distributions in the electron and muon channels combined in the lepton-tagged category for $m_H = 125$ GeV for the 2016 data-taking period. The left plot shows the fit to simulated ZH production events, and the right plot shows the fit to simulated WH production events. The blue line shows the total fit function, the green line shows the Crystal Ball function component, and the red line shows the Gaussian function component.

background function is chosen from a set of candidate functions via a discrete nuisance parameter in the fit. These functions are derived from the data in each category, with muon and electron events from all data-taking years combined. The $m_{\ell^+\ell^-\gamma}$ spectrum consists of a turn-on peak around 110–115 GeV and a monotonically falling spectrum in the high-mass tail, where the turn-on peak is driven by the photon p_T selection. These features are modeled by the convolution of a Gaussian function, which is used to describe the lower-mass (turn-on) portion of the spectrum, with a step function that is multiplied by one of several functions, which are used to describe the higher-mass (tail) portion of the spectrum. The complete function has the general form:

$$(8.1) \quad \mathcal{F}(m_{\ell^+\ell^-\gamma}; \mu_G, \sigma_G, s, \vec{\alpha}) = \int_{m_{\min}}^{m_{\max}} \mathcal{N}(m_{\ell^+\ell^-\gamma} - t; \mu_G, \sigma_G) \Theta(t; s) f(t; \vec{\alpha}) dt,$$

where t is the integration variable for the convolution, $m_{\min} = 105 \text{ GeV}$ and $m_{\max} = 170 \text{ GeV}$ are the limits of integration, $\mathcal{N}(m_{\ell^+\ell^-\gamma} - t; \mu_G, \sigma_G)$ is the Gaussian function with mean μ_G and standard deviation σ_G , $\Theta(t; s)$ is the Heaviside step function with step location s , and $f(t; \vec{\alpha})$ is the falling spectrum function with shape parameters $\vec{\alpha}$.

Since the background modeling strategy has been changed several times throughout the history of the CMS $H \rightarrow Z\gamma$ searches, it is worthwhile to understand the motivation for the current approach. Previously, in the 2016 analysis, the background was modeled for the $m_{\ell^+\ell^-\gamma}$ range of 115–170 GeV. The choice to extend the mass range down to 105 GeV was made in order to improve the model in the low mass region near the turn-on peak and avoid potential bias. Figure 8.4 shows a comparison of fits in each category with and without modeling the turn-on. From the plots, it is clear that modeling the turn-on properly yields a better fit around 115 GeV, the previous lower bound of the fit used in the 2016 search.

8.3.1. Falling Spectrum Component Families

The choice of falling spectrum component to model the background in a given category is not a priori known. For this reason, we consider several function families for the falling spectrum. The families considered include exponential functions, power law functions, Laurent series, and Bernstein polynomials. These families are described in more detail below.

- exponential series of order N:

$$(8.2) \quad \text{Exp}_N(m_{\ell\ell\gamma}) = \sum_{i=1}^N f_i e^{p_i m_{\ell\ell\gamma}}$$

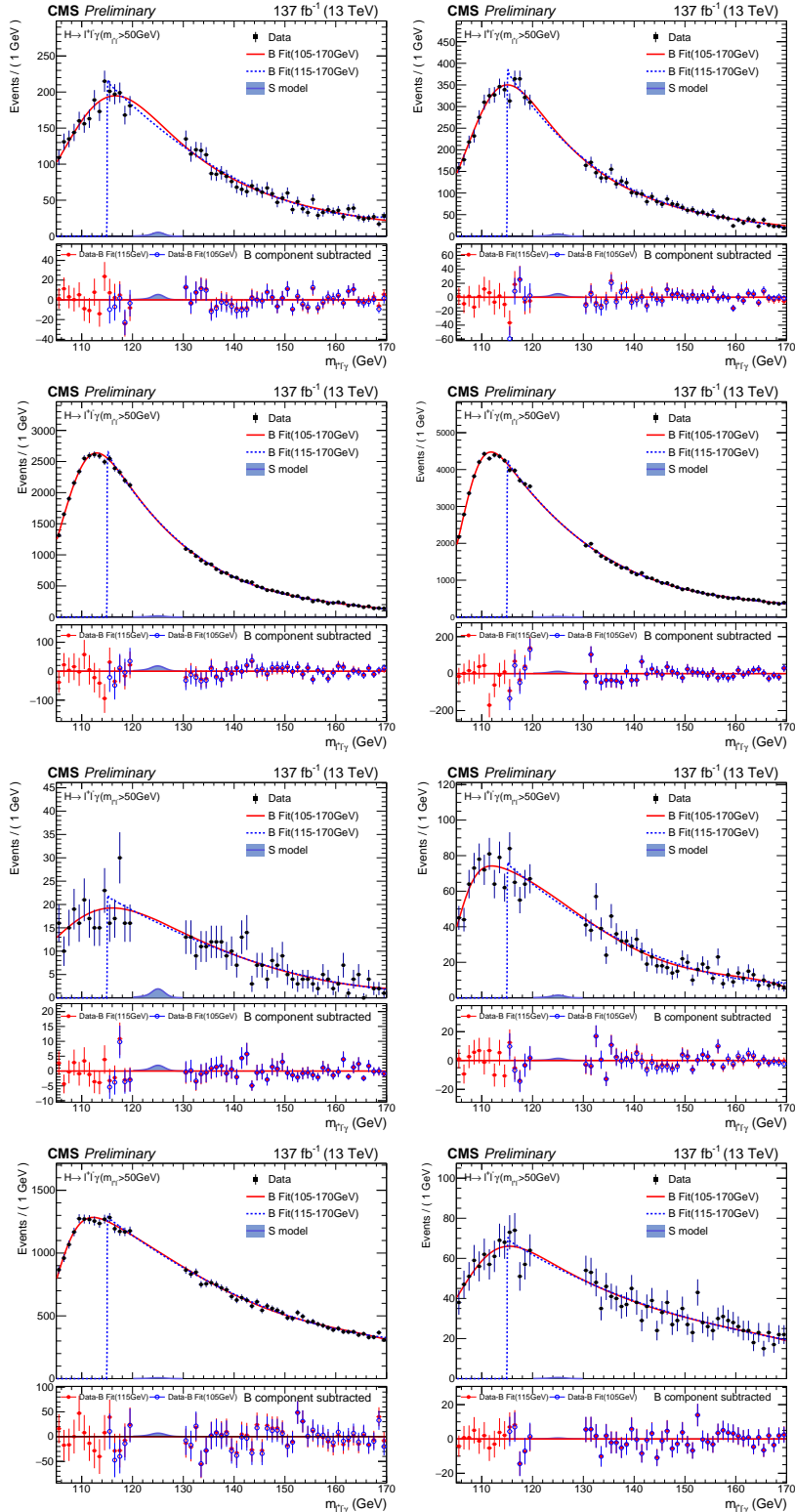


Figure 8.4. Comparison of background fits with and without modeling the turn-on. The top four plots correspond to the untagged categories, and the bottom four plots correspond to the dijet categories and lepton-tagged category.

with $2N$ free parameters: $p_i < 0$ and f_i . The lowest order considered has $N = 1$,

i.e. one term. The next order has 2 exponential terms, but 3 parameters.

- power law series of order N:

$$(8.3) \quad \text{Pow}_N(m_{\ell\ell\gamma}) = \sum_{i=1}^N f_i m_{\ell\ell\gamma}^{p_i}$$

with $2N$ free parameters: $p_i < 0$ and f_i . The lowest order considered has $N = 1$,

i.e. one term.

- Laurent series with 2, 3, 4, 5, or 6 terms, where $N + 1$ equals the number of free parameters:

$$(8.4) \quad \text{Lau}_1(m_{\ell\ell\gamma}) = f_2 m_{\ell\ell\gamma}^{-4} + f_3 m_{\ell\ell\gamma}^{-5}$$

$$(8.5) \quad \text{Lau}_2(m_{\ell\ell\gamma}) = f_1 m_{\ell\ell\gamma}^{-3} + f_2 m_{\ell\ell\gamma}^{-4} + f_3 m_{\ell\ell\gamma}^{-5}$$

$$(8.6) \quad \text{Lau}_3(m_{\ell\ell\gamma}) = f_1 m_{\ell\ell\gamma}^{-3} + f_2 m_{\ell\ell\gamma}^{-4} + f_3 m_{\ell\ell\gamma}^{-5} + f_4 m_{\ell\ell\gamma}^{-6}$$

$$(8.7) \quad \text{Lau}_4(m_{\ell\ell\gamma}) = f_1 m_{\ell\ell\gamma}^{-2} + f_2 m_{\ell\ell\gamma}^{-3} + f_3 m_{\ell\ell\gamma}^{-4} + f_4 m_{\ell\ell\gamma}^{-5} + f_5 m_{\ell\ell\gamma}^{-6}$$

$$(8.8) \quad \text{Lau}_5(m_{\ell\ell\gamma}) = f_1 m_{\ell\ell\gamma}^{-2} + f_2 m_{\ell\ell\gamma}^{-3} + f_3 m_{\ell\ell\gamma}^{-4} + f_4 m_{\ell\ell\gamma}^{-5} + f_5 m_{\ell\ell\gamma}^{-6} + f_6 m_{\ell\ell\gamma}^{-7}$$

- Bernstein polynomial of order N:

$$(8.9) \quad \text{Bern}_N(m_{\ell\ell\gamma}) = \sum_{i=0}^N f_i b_{i,N}(m_{\ell\ell\gamma})$$

$$(8.10) \quad b_{i,N}(m_{\ell\ell\gamma}) = \binom{N}{i} m_{\ell\ell\gamma}^i (1 - m_{\ell\ell\gamma}^{N-i})$$

with N free parameters f_i . The lowest order considered has $N = 1$.

8.3.2. Discrete Profiling Method

In each category, there is ambiguity about which function to choose to model the background. In principle, the choice of function is a source of systematic uncertainty in the measurement. The discrete profiling method was developed as a way to assess this uncertainty in a formal way. In this method, the choice of function for the background fit is included as a discrete nuisance parameter in the full likelihood function. All reasonable families of functions should be considered, and a range of orders should be considered within each family. The set of functions profiled in a given category is referred to as an *envelope*. The exact composition of the envelope in each category is based on a set of selection requirements that account for goodness of fit, an \mathcal{F} -test [94] procedure that determines the highest order function to be included, and an assessment of bias and frequentist coverage. The details of this selection will be described later in this chapter. When fitting the background, all functions in the envelope are tried, with a penalty term added to the likelihood to account for the number of free parameters in the fit and ensure that higher-order functions are not preferred a priori. When a measurement is made of a

parameter of interest, such as the signal strength, the function with the smallest negative log likelihood, profiled as a function of the parameter of interest, is used. This profiling allows the best fit function to change for different values of the parameter of interest, so we can say that we carry out the fit with the full envelope of functions. The envelope yields a profile likelihood curve that is broader than the profile likelihood curve obtained from any individual function. This increase in breadth reflects the uncertainty associated with the choice of background function.

8.3.3. Envelope Selection

Individual functions are added to the envelope in a given category based on a series of selection requirements. In general, the requirements are related to three main factors: goodness of fit, \mathcal{F} -test results, and bias results. The simplest requirement is a basic goodness of fit cut. For each function considered, the chi-squared per number of degrees of freedom is calculated. This is then converted into a p -value, or chi-squared probability. If the chi-squared probability is greater than 0.01, we consider the quality of the fit good enough for the envelope. Any function failing this requirement is thrown away, as it cannot be considered a reasonable description of the background in data.

The second consideration is the result of an \mathcal{F} -test. The \mathcal{F} -test is a way to compare functions within a specific family of falling spectrum component functions. It compares the fit of a lower-order function in the family to that of a higher-order function. While it is expected that the higher-order function will always provide a better fit, the question is whether the higher-order fit is better in a statistically significant way. If it is not significantly better, there is a motivation to stick to the lower-order function and exclude

the higher-order function from the envelope. The details of the \mathcal{F} -test procedure are as follows. First, the lowest-order function in a given family is fit to the data in a given category. Then, the next-highest-order function is fit to the same data. The difference between twice the negative log likelihood between the two fits, $2\Delta NLL_{N+1} = 2(NLL_N - NLL_{N+1})$, can be used to determine whether the data better support the higher-order function. More specifically, $2\Delta NLL_{N+1}$ is distributed as a chi-squared function with M degrees of freedom, where M is the difference in the number of free parameters between the order $N + 1$ function and the order N function. For example, in the case of the first two orders of the exponential family, $M = 4 - 2 = 2$, and for the Bernstein polynomial family, $M = 3 - 2 = 1$. After carrying out the fits and computing the negative log likelihoods, a p -value is then calculated as

$$(8.11) \quad p = P(2\Delta NLL > 2\Delta NLL_{N+1} | \chi^2(M)).$$

If this p -value is less than 0.05, we state that the higher-order function is supported by the data, and the procedure is repeated for the next-highest-order function. Alternatively, if the p -value is greater than 0.05, the higher-order function is assumed to be too flexible, and the \mathcal{F} -test ends, having found the highest-order function supported by the data. In this analysis, we consider fits up to order 5 for each falling spectrum family. In each family, we use this procedure to identify the highest-order function to include in the envelope. We then also include all lower-order functions within the family that pass the chi-squared goodness of fit criterion.

The final factor in selecting functions for the envelope is an assessment of bias and frequentist coverage. After constructing an initial envelope in a given category based on

the chi-squared and \mathcal{F} -test results, an envelope bias study is performed. For this study, 1,000 pseudo-data sets are generated from each function contained in the envelope, which are subsequently fit with the full envelope, where the discrete index of the background function is allowed to float. In general, this means that different pseudo-data sets may be fit by different constituent functions within the envelope, and these functions may be different from the generating function. With the resulting collection of fits, we compute the bias and frequentist coverage of the signal strength μ . For each fit, we obtain a best fit signal strength $\hat{\mu}$ and a 68% confidence interval ($\hat{\mu}_{\text{down}}$, $\hat{\mu}_{\text{up}}$). We define the pull for each toy as $(\hat{\mu} - \mu_{\text{true}})/\sigma_{\hat{\mu}}$. The pull distribution is expected to be drawn from a unit Gaussian function. We fit the pull distribution with a Gaussian, and the best fit mean value is taken to be the bias. The coverage is defined as the frequency with which zero falls within the confidence interval ($\hat{\mu}_{\text{down}}$, $\hat{\mu}_{\text{up}}$). It is expected to be near 68%. If overcoverage is observed, this implies the uncertainty in the signal strength may be overly conservative. Within a few percent of 68%, this is acceptable. If undercoverage of a significant amount is observed, this implies a problem with the model, and may mean that the individual functions are biased or that the envelope should be made more flexible.

There are several possible outcomes of the bias studies in each category. One outcome is that the bias is minimal and the coverage good for all truth functions. In this case, we accept the composition of the envelope as good for the analysis. Another possible outcome is that one or more truth functions is associated with a large (significantly greater than 14%) bias or low (significantly less than 68%) coverage. In this case, we can consider adding more functions to the envelope to increase the flexibility of the model, and then retry the bias study using the extended envelope.

The fits of the final chosen envelope functions in each category are shown in Figure 8.5. The corresponding bias and coverage results for the final envelope in each category are shown in Tables 8.1a through 8.1h. In the categories untagged 3, untagged 4, and dijet 3, it was observed that the initial functions chosen by the chi-squared and F-test procedure showed large biases (greater than 20%) and low coverages (less than 60%) for certain truth functions. Therefore, the envelope was extended to include higher order Bernstein functions up to order 5 for each of these categories. The bias tables for these categories reflect the results for the final extended envelope, including these added functions.

8.4. Obtaining Results

The best fit value of the signal strength, $\hat{\mu}$, is determined by maximizing the likelihood, accounting for all nuisance parameters. The uncertainty in $\hat{\mu}$ and the observed significance are derived from the profile likelihood test statistic [95],

$$(8.12) \quad q(\mu) = -2\ln\left(\frac{\mathcal{L}(\mu, \hat{\vec{\theta}}_\mu)}{\mathcal{L}(\hat{\mu}, \hat{\vec{\theta}})}\right),$$

where $\vec{\theta}$ is the set of nuisance parameters, $\hat{\mu}$ and $\hat{\vec{\theta}}$ are unconditional best fit values, and $\hat{\vec{\theta}}_\mu$ is the set of conditional best fit values of the nuisance parameters for a given value of μ . An upper limit on μ is determined using the profile likelihood statistic with the CL_s criterion. The asymptotic approximation for the sampling distribution of $q(\mu)$ is assumed in the derivation of these results [95, 96, 97, 98]. The expected significance under the SM hypothesis and the expected upper limits under the background-only hypothesis are also reported. These are obtained by fitting to the corresponding Asimov data sets [98].

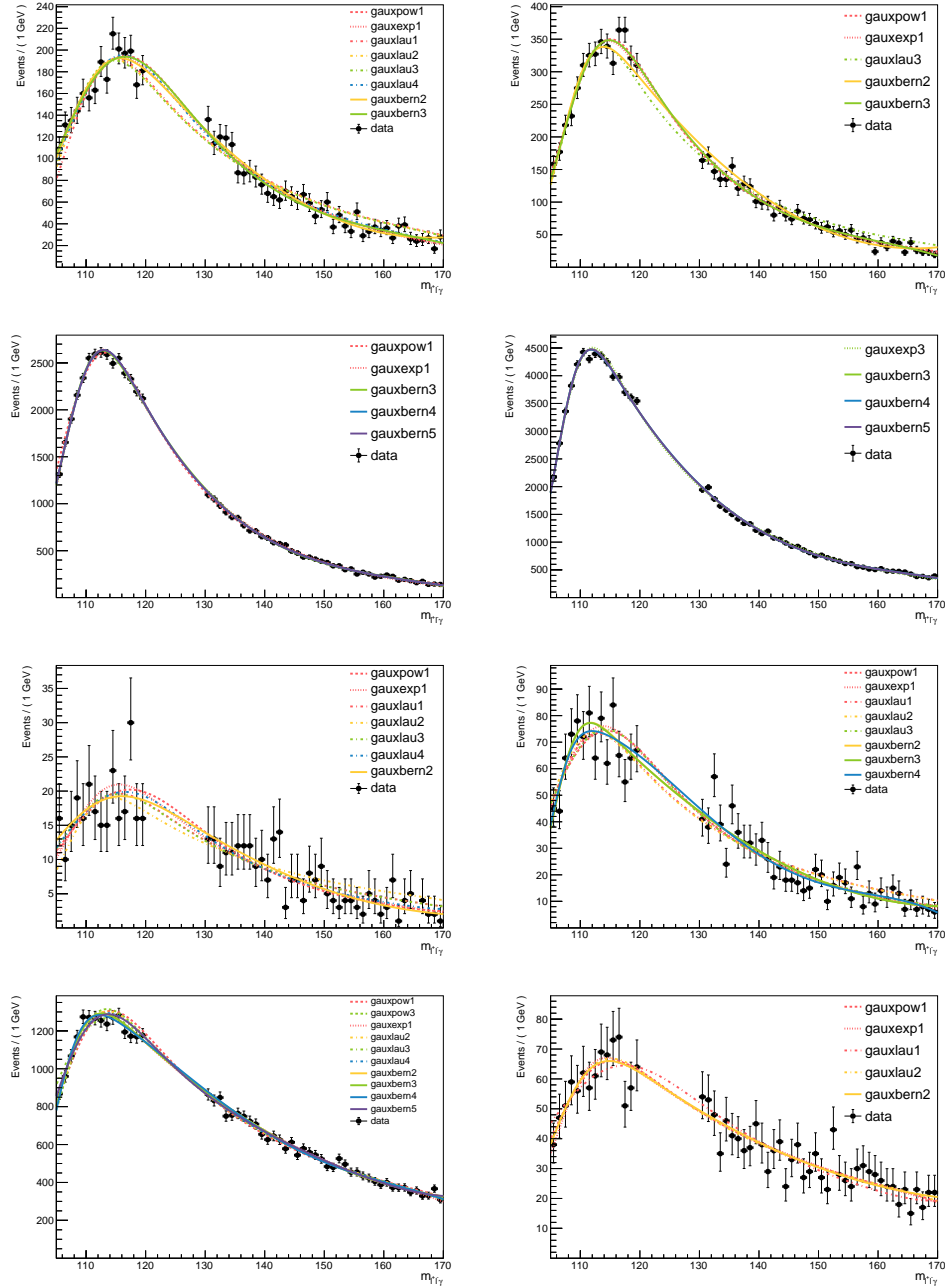


Figure 8.5. Background functions selected for the envelope in each category. The top four plots correspond to the untagged categories, and the bottom four correspond to the dijet categories and lepton tag category.

Table 8.1. Bias and coverage results for each category.

Generating Function	Exp1	Pow1	Lau1	Lau2	Lau3	Lau4	Bern2	Bern3
Bias	-0.03	0.02	0.02	0.06	0.04	-0.09	-0.07	0.00
Coverage	± 0.03	± 0.04	± 0.03	± 0.04				
	0.68	0.66	0.71	0.68	0.71	0.68	0.65	0.70

(a) Untagged 1 bias and coverage results from the final envelope bias study.

Generating Function	Exp1	Pow1	Lau3	Bern2	Bern3
Bias	-0.10	-0.09	-0.27	-0.07	0.07
Coverage	± 0.04	± 0.05	± 0.04	± 0.03	± 0.04
	0.67	0.66	0.67	0.67	0.65

(b) Untagged 2 bias and coverage results from the final envelope bias study.

Generating Function	Exp1	Pow1	Bern3	Bern4	Bern5
Bias	-0.05	-0.11	0.03	-0.02	0.27
Coverage	± 0.04	± 0.03	± 0.04	± 0.03	± 0.04
	0.67	0.67	0.70	0.67	0.66

(c) Untagged 3 bias and coverage results from the final envelope bias study.

Generating Function	Exp3	Bern3	Bern4	Bern5
Bias	-0.08	0.07	0.16	0.10
Coverage	± 0.03	± 0.03	± 0.03	± 0.03
	0.68	0.67	0.67	0.68

(d) Untagged 4 bias and coverage results from the final envelope bias study.

Generating Function	Exp1	Pow1	Lau1	Lau2	Lau3	Lau4	Bern2
Bias	0.03	0.09	-0.02	-0.06	-0.02	0.02	-0.04
Coverage	± 0.03	± 0.03	± 0.04	± 0.04	± 0.03	± 0.03	± 0.03
	0.64	0.66	0.66	0.68	0.67	0.68	0.66

(e) Dijet 1 bias and coverage results from the final envelope bias study.

Generating Function	Exp1	Pow1	Pow3	Lau2	Lau3	Lau4	Bern2	Bern3	Bern4	Bern5
Bias	-0.12	-0.29	-0.14	-0.22	-0.16	-0.18	-0.06	-0.05	0.05	-0.13
Coverage	± 0.04	± 0.03	± 0.03	± 0.03						
	0.67	0.65	0.68	0.66	0.66	0.67	0.68	0.64	0.67	0.65

(f) Dijet 2 bias and coverage results from the final envelope bias study.

Generating Function	Exp1	Pow1	Pow3	Lau2	Lau3	Lau4	Bern2	Bern3	Bern4	Bern5
Bias	-0.12	-0.29	-0.14	-0.22	-0.16	-0.18	-0.06	-0.03	0.05	-0.13
Coverage	± 0.03	± 0.04	± 0.04	± 0.04	± 0.03	± 0.03	± 0.03	± 0.05	± 0.03	± 0.03
	0.67	0.65	0.68	0.67	0.66	0.67	0.68	0.64	0.67	0.65

(g) Dijet 3 bias and coverage results from the final envelope bias study.

Generating Function	Exp1	Pow1	Lau1	Lau2	Bern2
Bias	-0.04	0.05	0.27	0.03	-0.03
Coverage	± 0.03	± 0.03	± 0.04	± 0.03	± 0.03
	0.71	0.69	0.66	0.70	0.70

(h) Lepton-tagged bias and coverage results from the final envelope bias study.

In addition, a combined maximum likelihood fit with the CMS measurement [13] of $H \rightarrow \gamma\gamma$ using the same data sample is performed to determine the ratio $\mathcal{B}(H \rightarrow Z\gamma)/\mathcal{B}(H \rightarrow \gamma\gamma)$. The $H \rightarrow \gamma\gamma$ analysis obtained a signal strength for $\sigma(pp \rightarrow H)\mathcal{B}(H \rightarrow \gamma\gamma)$ of 1.12 ± 0.09 . In this combined fit, the branching fraction $\mathcal{B}(H \rightarrow \gamma\gamma)$ is an additional free parameter. The uncertainty in the measured ratio of the two branching fractions is dominated by the statistical uncertainties in the branching fractions. Common sources of theoretical and experimental uncertainty in the two measurements, described in the next section, are treated as correlated in the fit. The combination is performed at $m_H = 125.38\text{ GeV}$, and the discrete profiling method is used for the background modeling in both cases.

CHAPTER 9

Systematic Uncertainties

The uncertainties associated with the choice of background shape are incorporated into the fit to the data through the use of the discrete profiling method. They are, therefore, reflected in the statistical uncertainties obtained from the fit. The systematic uncertainties, affecting either the normalization or the shape of the signal expectation, are listed below, and the numerical values are summarized in Table 9.1, which also indicates whether the effect is correlated between the data-taking periods. Overall, systematic uncertainty comprises only about 5% of the total uncertainty in the measurement, as the statistical uncertainty due to the small number of expected signal events dominates. Observed and expected nuisance parameter impacts on the signal strength are included in Appendix D. Nuisance parameter impacts corresponding to the $\mathcal{B}(H \rightarrow Z\gamma)/\mathcal{B}(H \rightarrow \gamma\gamma)$ measurement are also included.

- Theoretical cross section calculations: These include the effects of the choice of PDFs, the value of the strong coupling constant (α_S), and the effect of missing higher orders in the perturbative cross section calculations, evaluated from variations of the renormalization and factorization scales (μ_R , μ_F) [90, 91, 92]. The uncertainties are treated as independent for each Higgs boson production mechanism. The uncertainty in $\mathcal{B}(H \rightarrow Z\gamma)$ is also considered [12].

- Underlying event and parton shower modeling: The uncertainty associated with the choice and tuning of the generator is estimated with dedicated samples which are generated by varying the parameters of the tune used to generate the original signal samples. The uncertainties are treated as correlated for the 2017 and 2018 samples, which use the CP5 tune [72], while being uncorrelated with the 2016 sample, which uses the CUETP8M1 tune [71].
- Integrated luminosity: The integrated luminosities for the 2016, 2017, and 2018 data-taking years have uncertainties of 1.2%, 2.3%, and 2.5% [59, 60, 61], respectively, corresponding to an overall uncertainty for the 2016–2018 period of 1.6%, the improvement in precision reflecting the (uncorrelated) time evolution of some systematic effects.
- L1 trigger: During the 2016 and 2017 data-taking periods, a gradual shift in the timing of the inputs of the ECAL L1 trigger in the $|\eta| > 2.4$ region led to a specific inefficiency. A correction of approximately 1% is applied to the simulation along with the corresponding uncertainty in the inefficiency measurement.
- Trigger: Uncertainties are evaluated for the corrections applied to the simulation to match the trigger efficiencies measured in data with $Z \rightarrow e^+e^-$ and $Z \rightarrow \mu^+\mu^-$ events.
- Photon identification and isolation: Uncertainties are evaluated for the corrections applied to the simulation to match the selection efficiencies in data measured with $Z \rightarrow e^+e^-$ events.

- Lepton identification and isolation: Uncertainties are evaluated for the corrections applied to the simulation to match electron and muon selection efficiencies in data measured with $Z \rightarrow e^+e^-$ and $Z \rightarrow \mu^+\mu^-$ events.
- Pileup modeling: The uncertainty in the description of the pileup in the signal simulation is estimated by varying the total inelastic cross section by $\pm 4.6\%$ [93].
- Kinematic BDT: The uncertainties in the photon and lepton energy and the correction of the photon MVA discriminant are propagated to \mathcal{D}_{kin} . Changes in \mathcal{D}_{kin} cause the migration of signal events across category boundaries.
- VBF BDT: The uncertainties in the jet energy and the uncertainty in \mathcal{D}_{kin} are propagated to \mathcal{D}_{VBF} . Changes in \mathcal{D}_{VBF} cause the migration of signal events across category boundaries.
- Photon energy scale and resolution: The photon energy in the simulation is varied due to the ECAL energy scale and resolution uncertainties, and the effects on the signal mean and resolution parameters are propagated to the fits.
- Lepton momentum scale and resolution: The lepton momentum in the simulation is varied due to the lepton momentum scale and resolution uncertainties, and the effects on signal mean and resolution parameters are propagated to the fits.

In the $\mathcal{B}(H \rightarrow Z\gamma)/\mathcal{B}(H \rightarrow \gamma\gamma)$ measurement, the common sources of theoretical and systematic uncertainty in the two analyses are treated as correlated in the fit. These are the theoretical uncertainties in the Higgs production cross section calculations, and the systematic uncertainties in the underlying event and parton shower modeling, the integrated luminosity, and the L1 trigger inefficiency. The remaining uncertainties are treated as uncorrelated.

Table 9.1. Sources of systematic uncertainty affecting the simulated signal. The normalization effect on the expected yield, or the effect on the signal shape parameters, is given as indicated, with the values averaged over all event categories. The third column shows the uncertainties that have a correlated effect across the three data-taking periods.

Sources	Uncertainty (%)	Year-to-year correlation
Normalization		
Theoretical		
– $\mathcal{B}(H \rightarrow Z\gamma)$	5.7	Yes
– ggH cross section (μ_F, μ_R)	3.9	Yes
– ggH cross section (α_S)	2.6	Yes
– ggH cross section (PDF)	1.9	Yes
– VBF cross section (μ_F, μ_R)	0.4	Yes
– VBF cross section (α_S)	0.5	Yes
– VBF cross section (PDF)	2.1	Yes
– WH cross section (μ_F, μ_R)	$+0.6$ -0.7	Yes
– WH cross section (PDF)	1.7	Yes
– ZH cross section (μ_F, μ_R)	$+3.8$ -3.1	Yes
– ZH cross section (PDF)	1.3	Yes
– WH/ZH cross section (α_S)	0.9	Yes
– $t\bar{t}H$ cross section (μ_F, μ_R)	$+5.8$ -9.2	Yes
– $t\bar{t}H$ cross section (α_S)	2.0	Yes
– $t\bar{t}H$ cross section (PDF)	3.0	Yes
Underlying event and parton shower	3.7–4.4	Partial
Integrated luminosity	1.2–2.5	Partial
L1 trigger	0.1–0.4	No
Trigger		
– Electron channel	0.9–1.9	No
– Muon channel	0.1–0.4	No
Photon identification and isolation	0.2–5.0	Yes
Lepton identification and isolation		
– Electron channel	0.5–0.7	Yes
– Muon channel	0.3–0.4	Yes
Pileup	0.4–1.0	Yes
Kinematic BDT	2.5–3.7	Yes
VBF BDT	5.9–14.0	Yes
Shape parameters		
Photon energy and momentum		
– Signal mean	0.1–0.4	Yes
– Signal resolution	3.1–5.9	Yes
Lepton energy and momentum		
– Signal mean	0.007	Yes
– Signal resolution	0.007–0.010	Yes

CHAPTER 10

Results and Interpretation

Figures 10.1 and 10.2 show the $m_{\ell^+\ell^-\gamma}$ distributions of the data events in each category. The expected SM $H \rightarrow Z\gamma$ distributions, scaled by a factor of 10, are also shown. Figure 10.3 shows the signal-plus-background fit to the data and the corresponding distribution after background subtraction for the sum of all categories. Each category is weighted by the factor $S/(S + B)$, where S is the signal yield and B is the background yield in the narrowest mass interval containing 95% of the signal distribution.

The best fit value of the signal strength is $2.4^{+0.8}_{-0.9}$ (stat) $^{+0.3}_{-0.2}$ (syst) at $m_H = 125.38$ GeV. The corresponding measured value of $\sigma(pp \rightarrow H)\mathcal{B}(H \rightarrow Z\gamma)$ is $0.21^{+0.07}_{-0.08}$ (stat) $^{+0.03}_{-0.02}$ (syst) pb. This measurement is consistent with the SM prediction of 0.09 ± 0.01 pb at the 1.6 standard deviation level. Figure 10.4 shows the signal strengths obtained for each category separately, corresponding to the fit results shown in Figs. 10.1 and 10.2, as well as from simultaneous fits to the dijet categories, the untagged categories, and all categories combined. Among the eight categories, dijet 1 is the most sensitive. A category compatibility p -value, under the hypothesis of a common signal strength in all categories, is calculated from the likelihood ratio between the nominal combined fit, in which all categories have the same signal strength parameter, and a separate fit, in which each category has its own signal strength parameter. This p -value is found to be 0.02, corresponding to 2.3 standard deviations, and is driven by the dijet 3 category, which has a signal strength of $\hat{\mu} = 12.3^{+3.7}_{-3.5}$. The observed (expected) local significance is 2.7 (1.2) standard

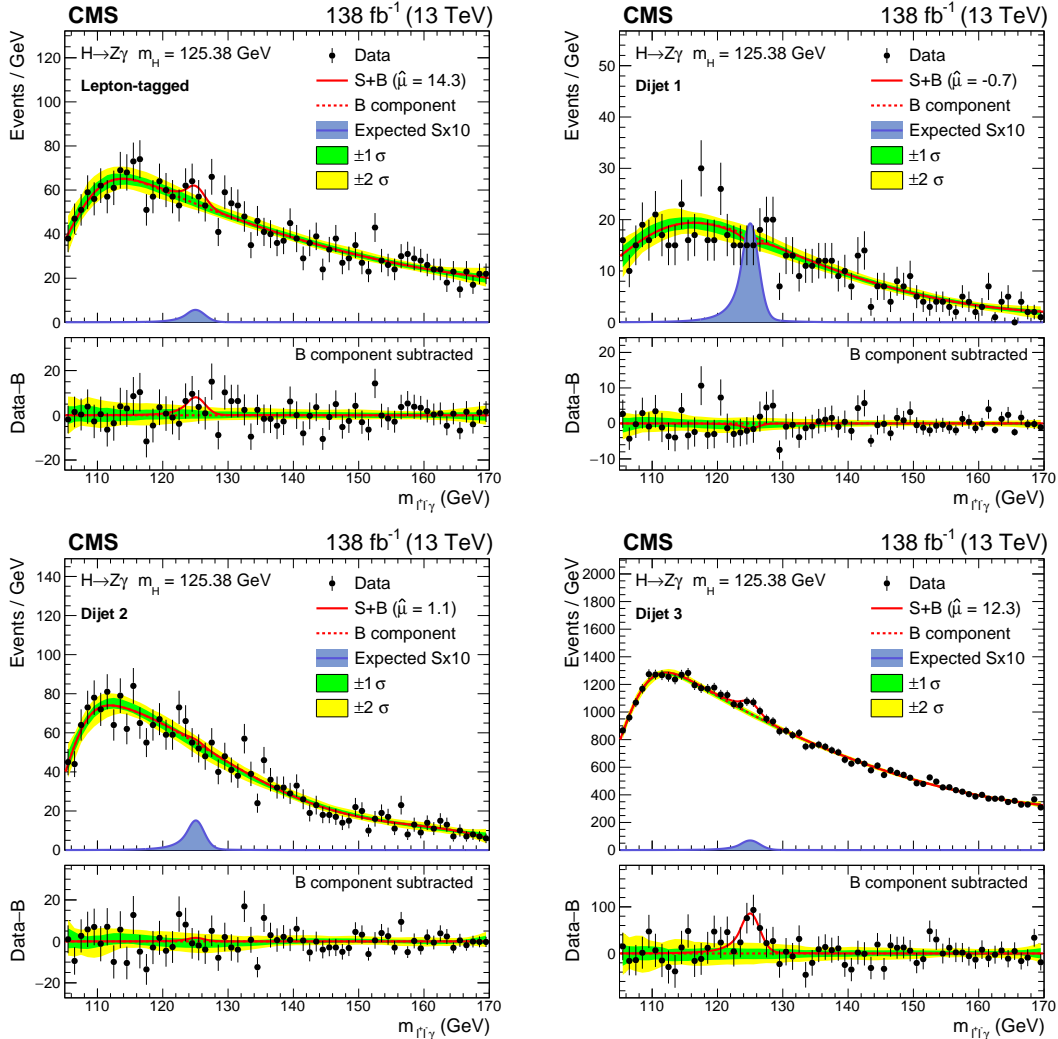


Figure 10.1. Fits to the $m_{\ell^+\ell^-\gamma}$ data distribution in the lepton-tagged (upper left), dijet 1 (upper right), dijet 2 (lower left), and dijet 3 (lower right) categories. In the upper panel, the red solid line shows the result of a signal-plus-background fit to the given category. The red dashed line shows the background component of the fit. The green and yellow bands represent the 68 and 95% CL uncertainties in the fit. Also plotted is the expected SM signal, scaled by a factor of 10. In the lower panel, the data minus the background component of the fit is shown.

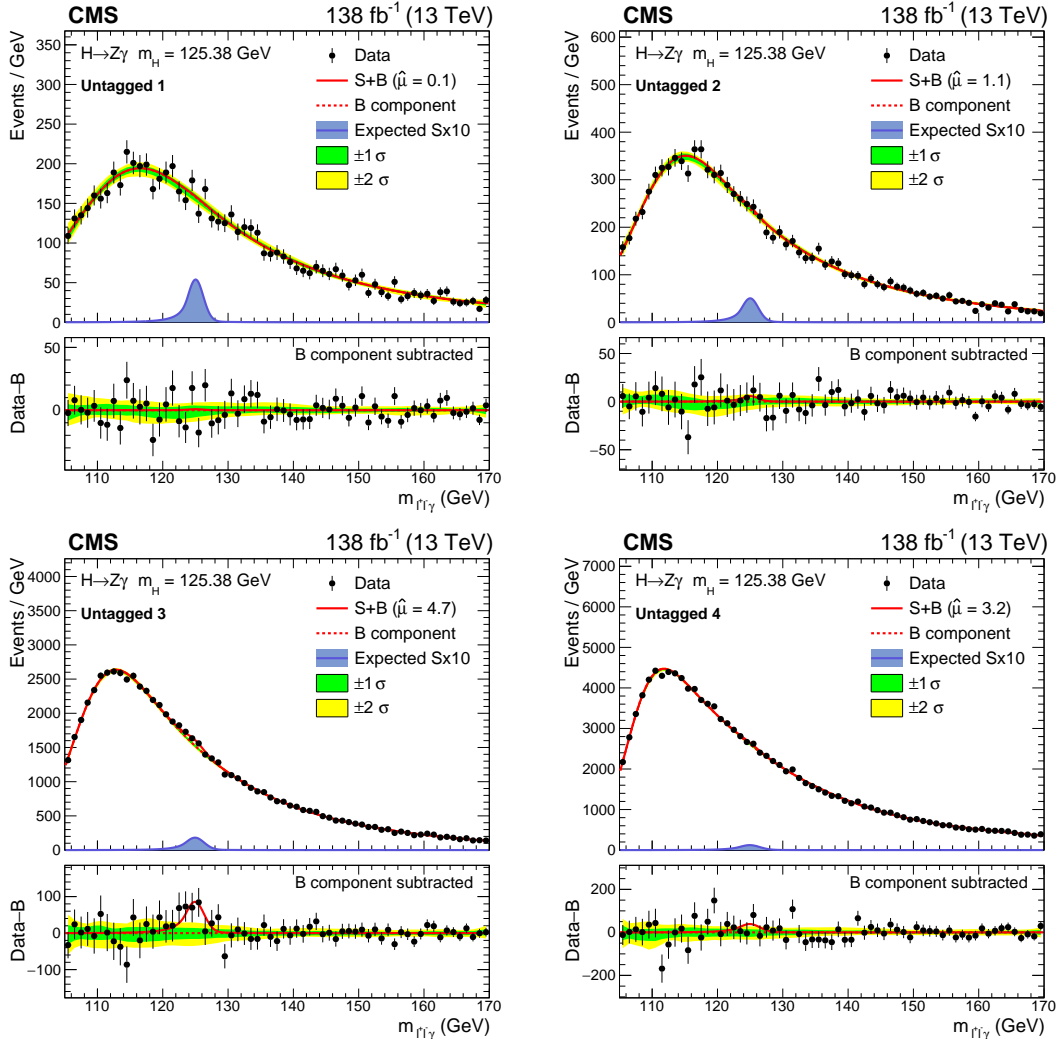


Figure 10.2. Fits to the $m_{\ell^+\ell^-\gamma}$ data distribution in the untagged 1 (upper left), untagged 2 (upper right), untagged 3 (lower left), and untagged 4 (lower right) categories. In the upper panel, the red solid line shows the result of a signal-plus-background fit to the given category. The red dashed line shows the background component of the fit. The green and yellow bands represent the 68 and 95% CL uncertainties in the fit. Also plotted is the expected SM signal, scaled by a factor of 10. In the lower panel, the data minus the background component of the fit is shown.

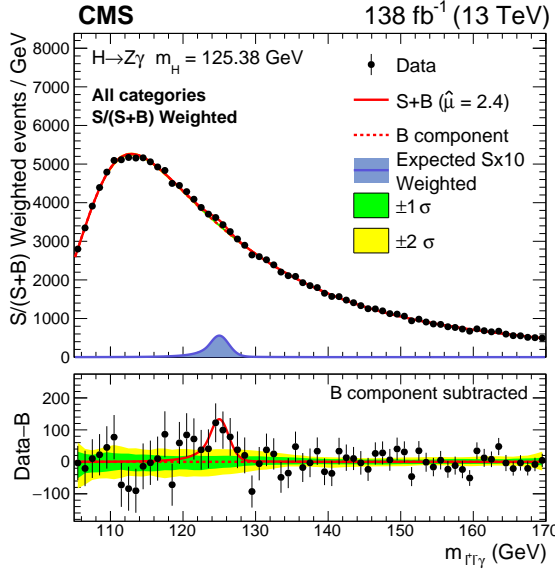


Figure 10.3. Sum over all categories of the data points and signal-plus-background model after the simultaneous fit to each $m_{\ell^+\ell^-\gamma}$ distribution. The contribution from each category is weighted by $S/(S + B)$, as defined in the text. In the upper panel, the red solid line shows the signal-plus-background fit. The red dashed line shows the background component of the fit. The green and yellow bands represent the 68 and 95% CL uncertainties in the fit. Also plotted is the expected SM signal weighted by $S/(S + B)$ and scaled by a factor of 10. In the lower panel, the data minus the background component of the fit is shown.

deviations. Upper limits on μ are calculated at 1 GeV intervals in the mass range of $120 < m_{\ell^+\ell^-\gamma} < 130$ GeV and at $m_H = 125.38$ GeV, as shown in Fig. 10.5. The observed (expected) limit at 95% CL relative to the SM expectation for $m_H = 125.38$ GeV is 4.1 (1.8).

10.1. Ratio Measurement

The ratio $\mathcal{B}(H \rightarrow Z\gamma)/\mathcal{B}(H \rightarrow \gamma\gamma)$ is theoretically interesting, as it is potentially sensitive to BSM physics, as described in Chapter 1. By combining the $H \rightarrow Z\gamma$ analysis

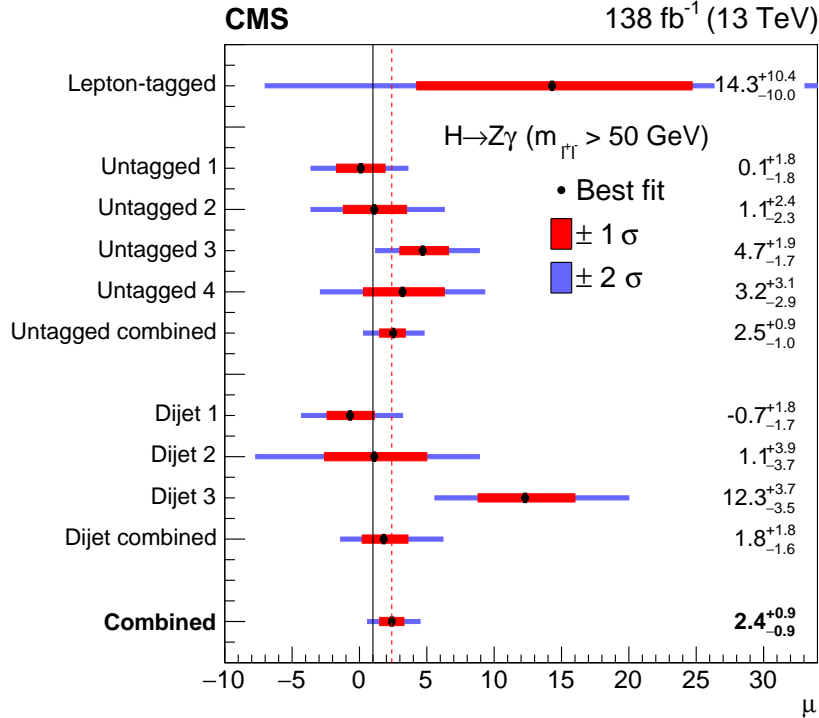


Figure 10.4. Observed signal strength (μ) for a SM Higgs boson with $m_H = 125.38$ GeV. The labels “untagged combined,” “dijet combined,” and “combined” represent the results obtained from simultaneous fits of the untagged categories, dijet categories, and full set of categories, respectively. The black solid line shows $\mu = 1$, and the red dashed line shows the best fit value $\hat{\mu} = 2.4 \pm 0.9$ of all categories combined.

with the existing CMS $H \rightarrow \gamma\gamma$ analysis of the same data set [13], we can obtain a measurement of this ratio and compare it to the SM prediction of 0.69 ± 0.04 .

The profile likelihood scans for the parameters of interest in the ratio fit are shown in Figure 10.6. The best fit values of the parameters of interest are $\mu_{\gamma\gamma} = 1.121^{+0.095}_{-0.090}$ and $\mu_{Z\gamma}/\mu_{\gamma\gamma} = 2.225^{+0.926}_{-0.825}$. The value of $\mu_{\gamma\gamma}$ agrees well with the standalone $H \rightarrow \gamma\gamma$ fit. Multiplying through, the value of $\mu_{Z\gamma}$ is 2.49, which agrees well with the result of the standalone $H \rightarrow Z\gamma$ fit. The measured value of $\mathcal{B}(H \rightarrow Z\gamma)/\mathcal{B}(H \rightarrow \gamma\gamma)$ is $1.5^{+0.7}_{-0.6}$.

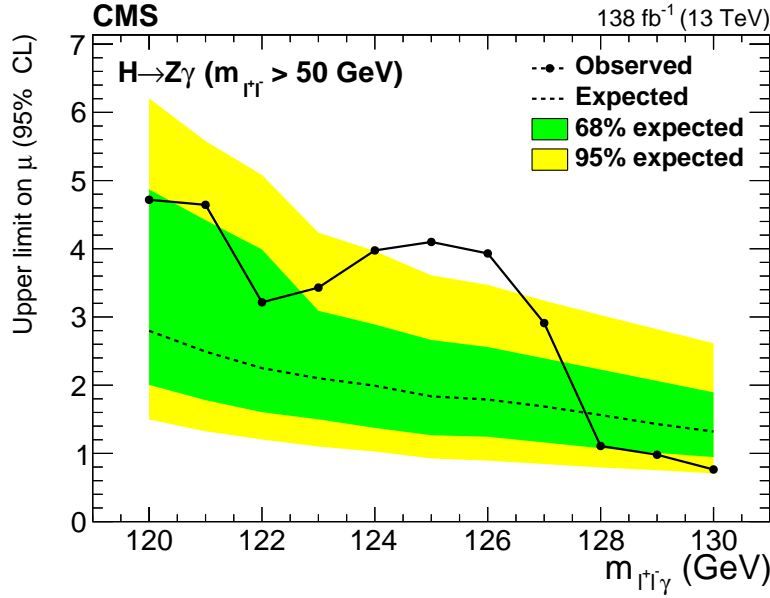


Figure 10.5. Upper limit (95% CL) on the signal strength (μ) relative to the SM prediction, as a function of the assumed value of the Higgs boson mass used in the fit.

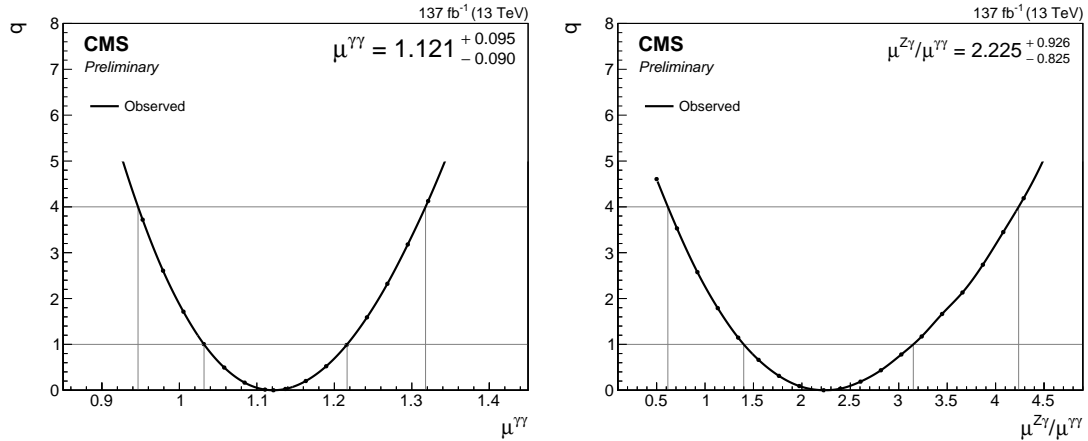


Figure 10.6. Profile likelihood scans of $\mu_{\gamma\gamma}$ and $\mu_{Z\gamma}/\mu_{\gamma\gamma}$ for $m_H = 125.38$ GeV.

This measurement is consistent with the SM prediction for the ratio at the 1.5 standard deviation level.

CHAPTER 11

Conclusion

A search is performed for a standard model (SM) Higgs boson decaying into a lepton pair (e^+e^- or $\mu^+\mu^-$) and a photon with $m_{\ell^+\ell^-} > 50$ GeV. The analysis is performed using a sample of proton-proton (pp) collision data at $\sqrt{s} = 13$ TeV, corresponding to an integrated luminosity of 138 fb^{-1} . The main contribution to this final state is from Higgs boson decays to a Z boson and a photon ($H \rightarrow Z\gamma \rightarrow \ell^+\ell^-\gamma$). The best fit value of the signal strength $\hat{\mu}$ for $m_H = 125.38$ GeV is $\hat{\mu} = 2.4^{+0.8}_{-0.9}$ (stat) $^{+0.3}_{-0.2}$ (syst) $= 2.4 \pm 0.9$. This measurement corresponds to $\sigma(\text{pp} \rightarrow H)\mathcal{B}(H \rightarrow Z\gamma) = 0.21 \pm 0.08$ pb. The measured value is 1.6 standard deviations higher than the SM prediction. The observed (expected) local significance is 2.7 (1.2) standard deviations, where the expected significance is determined for the SM hypothesis. The observed (expected) upper limit at 95% confidence level on μ is 4.1 (1.8). In addition, a combined fit with the $H \rightarrow \gamma\gamma$ analysis of the same data set is performed to measure the ratio $\mathcal{B}(H \rightarrow Z\gamma)/\mathcal{B}(H \rightarrow \gamma\gamma) = 1.5^{+0.7}_{-0.6}$, which is consistent with the ratio of 0.69 ± 0.04 predicted by the SM at the 1.5 standard deviation level.

While no observation has yet been made of $H \rightarrow Z\gamma$, the CMS Run 2 search marks the most optimal analysis carried out by the collaboration to date in this channel. In particular, the kinematic fit procedure and machine learning-based categorization strategy have greatly improved the sensitivity of the analysis. Moreover, detailed studies have led to a far more robust statistical approach to background modeling than in the previous

CMS searches, and these studies have greatly improved our understanding. We are confident that the innovations and insights of this analysis position CMS well for an eventual discovery of $H \rightarrow Z\gamma$. The wealth of data to be acquired and analyzed during Run 3 of the LHC will provide an excellent opportunity. We wish our colleagues the best of luck as they continue the search!

References

- [1] G. Aad *et al.* “Observation of a new particle in the search for the standard model Higgs boson with the ATLAS detector at the LHC.” *Phys. Lett. B* (2012) **716**:1. doi:10.1016/j.physletb.2012.08.020. 1207.7214.
- [2] S. Chatrchyan *et al.* “Observation of a new boson at a mass of 125 GeV with the CMS experiment at the LHC.” *Phys. Lett. B* (2012) **716**:30. doi:10.1016/j.physletb.2012.08.021. 1207.7235.
- [3] S. Chatrchyan *et al.* “Observation of a new boson with mass near 125 GeV in pp collisions at $\sqrt{s} = 7$ and 8 TeV.” *JHEP* (2013) **06**:081. doi:10.1007/JHEP06(2013)081. 1303.4571.
- [4] Particle Data Group, P. A. Zyla, *et al.* “Review of particle physics.” *Prog. Theor. Exp. Phys.* (2020) **2020**:083C01. doi:10.1093/ptep/ptaa104.
- [5] A. Abbasabadi, D. Bowser-Chao, D. A. Dicus, and W. W. Repko. “Radiative Higgs boson decays $H \rightarrow f\bar{f}\gamma$.” *Phys. Rev. D* (1997) **55**:5647. doi:10.1103/PhysRevD.55.5647. hep-ph/9611209.
- [6] L. B. Chen, C. F. Qiao, and R. L. Zhu. “Reconstructing the 125 GeV SM Higgs boson through $\ell\bar{\ell}\gamma$.” *Phys. Lett. B* (2013) **726**:306. doi:10.1016/j.physletb.2013.08.050. 1211.6058.
- [7] Y. Sun, H. Chang, and D. Gao. “Higgs decays to $\gamma\ell^+\ell^-$ in the standard model.” *JHEP* (2013) **05**:061. doi:10.1007/JHEP05(2013)061. 1303.2230.
- [8] G. Passarino. “Higgs boson production and decay: Dalitz sector.” *Phys. Lett. B* (2013) **727**:424. doi:10.1016/j.physletb.2013.10.052. 1308.0422.
- [9] J. M. Campbell, R. K. Ellis, W. T. Giele, and C. Williams. “Finding the Higgs boson in decays to $Z\gamma$ using the matrix element method at next-to-leading order.” *Phys. Rev. D* (2013) **87**:073005. doi:10.1103/PhysRevD.87.073005. 1301.7086.

- [10] G. Degrassi and M. Vitti. “The effect of an anomalous Higgs trilinear self-coupling on the $h \rightarrow \gamma Z$ decay.” *Eur. Phys. J. C* (2020) **80**:307. doi:10.1140/epjc/s10052-020-7860-7. 1912.06429.
- [11] I. Low, J. Lykken, and G. Shaughnessy. “Singlet scalars as Higgs imposters at the Large Hadron Collider.” *Phys. Rev. D* (2011) **84**:035027. doi:10.1103/PhysRevD.84.035027. 1105.4587.
- [12] D. de Florian *et al.* “Handbook of LHC Higgs cross sections: 4. deciphering the nature of the Higgs sector.” (2016) **2/2017**. doi:10.23731/CYRM-2017-002. 1610.07922.
- [13] A. M. Sirunyan *et al.* “Measurements of Higgs boson production cross sections and couplings in the diphoton decay channel at $\sqrt{s} = 13$ TeV.” *JHEP* (2021) **07**:027. doi:10.1007/JHEP07(2021)027. 2103.06956.
- [14] A. M. Sirunyan *et al.* “A measurement of the Higgs boson mass in the diphoton decay channel.” *Phys. Lett. B* (2020) **805**:135425. doi:10.1016/j.physletb.2020.135425. 2002.06398.
- [15] A. Djouadi, V. Driesen, W. Hollik, and A. Kraft. “The Higgs-photon-Z boson coupling revisited.” *Eur. Phys. J. C* (1998) **1**:163. doi:10.1007/BF01245806. hep-ph/9701342.
- [16] M. Carena, I. Low, and C. E. M. Wagner. “Implications of a modified Higgs to diphoton decay width.” *JHEP* (2012) **08**:060. doi:10.1007/JHEP08(2012)060. 1206.1082.
- [17] C.-W. Chiang and K. Yagyu. “Higgs boson decays to $\gamma\gamma$ and $Z\gamma$ in models with Higgs extensions.” *Phys. Rev. D* (2013) **87**:033003. doi:10.1103/PhysRevD.87.033003. 1207.1065.
- [18] C.-S. Chen, C.-Q. Geng, D. Huang, and L.-H. Tsai. “New scalar contributions to $h \rightarrow Z\gamma$.” *Phys. Rev. D* (2013) **87**:075019. doi:10.1103/PhysRevD.87.075019. 1301.4694.
- [19] G. Aad *et al.* “Search for Higgs boson decays to a photon and a Z boson in pp collisions at $\sqrt{s} = 7$ and 8 TeV with the ATLAS detector.” *Phys. Lett. B* (2014) **732**:8. doi:10.1016/j.physletb.2014.03.015. 1402.3051.
- [20] S. Chatrchyan *et al.* “Search for a Higgs boson decaying into a Z and a photon in pp collisions at $\sqrt{s} = 7$ and 8 TeV.” *Phys. Lett. B* (2013) **726**:587. doi:10.1016/j.physletb.2013.09.057. 1307.5515.

- [21] A. M. Sirunyan *et al.* “Search for the decay of a Higgs boson in the $\ell\ell\gamma$ channel in proton-proton collisions at $\sqrt{s} = 13$ TeV.” *JHEP* (2018) **11**:152. doi:10.1007/JHEP11(2018)152. 1806.05996.
- [22] G. Aad *et al.* “A search for the $Z\gamma$ decay mode of the Higgs boson in pp collisions at $\sqrt{s} = 13$ TeV with the ATLAS detector.” *Phys. Lett. B* (2020) **809**:135754. doi: 10.1016/j.physletb.2020.135754. 2005.05382.
- [23] G. Aad *et al.* “Evidence for Higgs boson decays to a low-mass dilepton system and a photon in pp collisions at $\sqrt{s}=13$ TeV with the ATLAS detector.” *Phys. Lett. B* (2021) **819**:136412. doi:10.1016/j.physletb.2021.136412. 2103.10322.
- [24] V. Khachatryan *et al.* “Search for a Higgs boson decaying into $\gamma^*\gamma \rightarrow \ell\ell\gamma$ with low dilepton mass in pp collisions at $\sqrt{s} = 8$ TeV.” *Phys. Lett. B* (2016) **753**:341. doi:10.1016/j.physletb.2015.12.039. 1507.03031.
- [25] Wikipedia Commons. “File:standard model of elementary particles.svg.” https://en.wikipedia.org/wiki/File:Standard_Model_of_Elementary_Particles.svg#file (2019).
- [26] F. Hasert, H. Faissner, W. Krenz, J. Von Krogh, D. Lanske, *et al.* “Search for elastic muon-neutrino electron scattering.” *Physics Letters B* (1973) **46** (1):121–124. ISSN 0370-2693. doi:10.1016/0370-2693(73)90494-2.
- [27] F. Hasert, S. Kabe, W. Krenz, J. Von Krogh, D. Lanske, *et al.* “Observation of neutrino-like interactions without muon or electron in the gargamelle neutrino experiment.” *Physics Letters B* (1973) **46** (1):138–140. ISSN 0370-2693. doi:[https://doi.org/10.1016/0370-2693\(73\)90499-1](https://doi.org/10.1016/0370-2693(73)90499-1).
- [28] G. Arnison *et al.* “Experimental Observation of Isolated Large Transverse Energy Electrons with Associated Missing Energy at $\sqrt{s} = 540$ GeV.” *Phys. Lett. B* (1983) **122**:103–116. doi:10.1016/0370-2693(83)91177-2.
- [29] M. Banner *et al.* “Observation of Single Isolated Electrons of High Transverse Momentum in Events with Missing Transverse Energy at the CERN anti-p p Collider.” *Phys. Lett. B* (1983) **122**:476–485. doi:10.1016/0370-2693(83)91605-2.
- [30] F. Englert and R. Brout. “Broken Symmetry and the Mass of Gauge Vector Mesons.” *Phys. Rev. Lett.* (1964) **13**:321–323. doi:10.1103/PhysRevLett.13.321.
- [31] P. W. Higgs. “Broken symmetries, massless particles and gauge fields.” *Phys. Lett.* (1964) **12**:132–133. doi:10.1016/0031-9163(64)91136-9.

- [32] P. W. Higgs. “Broken Symmetries and the Masses of Gauge Bosons.” *Phys. Rev. Lett.* (1964) **13**:508–509. doi:10.1103/PhysRevLett.13.508.
- [33] A. Cho. “Spontaneous symmetry breaking decanted.” *Science* (2012) **337** (6100):1289–1289. doi:10.1126/science.337.6100.1289. <https://www.science.org/doi/pdf/10.1126/science.337.6100.1289>
URL <https://www.science.org/doi/abs/10.1126/science.337.6100.1289>
- [34] L. Evans and P. Bryant. “LHC machine.” *Journal of Instrumentation* (2008) **3** (08):S08001–S08001. doi:10.1088/1748-0221/3/08/s08001.
URL <https://doi.org/10.1088/1748-0221/3/08/s08001>
- [35] S. Myers. *The LEP Collider, from design to approval and commissioning*. John Adams’ memorial lecture. CERN, Geneva (1991). doi:10.5170/CERN-1991-008. Delivered at CERN, 26 Nov 1990.
URL <https://cds.cern.ch/record/226776>
- [36] “LHC Design Report. 3. The LHC injector chain.” (2004) doi:10.5170/CERN-2004-003-V-3.
- [37] <https://home.cern/science/accelerators/accelerator-complex>.
- [38] S. Chatrchyan *et al.* “The CMS experiment at the CERN LHC.” *JINST* (2008) **3**:S08004. doi:10.1088/1748-0221/3/08/S08004.
- [39] A. M. Sirunyan *et al.* “Performance of the CMS Level-1 trigger in proton-proton collisions at $\sqrt{s} = 13$ TeV.” *JINST* (2020) **15**:P10017. doi:10.1088/1748-0221/15/10/P10017. 2006.10165.
- [40] V. Khachatryan *et al.* “The CMS trigger system.” *JINST* (2017) **12**:P01020. doi:10.1088/1748-0221/12/01/P01020. 1609.02366.
- [41] V. Khachatryan *et al.* “Performance of photon reconstruction and identification with the CMS detector in proton-proton collisions at $\text{sqrt}(s) = 8$ TeV.” *JINST* (2015) **10**:P08010. doi:10.1088/1748-0221/10/08/P08010. 1502.02702.
- [42] V. Khachatryan *et al.* “Performance of electron reconstruction and selection with the CMS detector in proton-proton collisions at $\sqrt{s} = 8$ TeV.” *JINST* (2015) **10**:P06005. doi:10.1088/1748-0221/10/06/P06005. 1502.02701.
- [43] A. M. Sirunyan *et al.* “Performance of the CMS muon detector and muon reconstruction with proton-proton collisions at $\sqrt{s} = 13$ TeV.” *JINST* (2018) **13**:P06015. doi:10.1088/1748-0221/13/06/P06015. 1804.04528.

- [44] S. Chatrchyan *et al.* “Description and performance of track and primary-vertex reconstruction with the CMS tracker.” *JINST* (2014) **9**:P10009. doi:10.1088/1748-0221/9/10/P10009. 1405.6569.
- [45] <https://cms.cern/detector>.
- [46] F. Cavallari and C. I. Rovelli. “Calibration and Performance of the CMS Electromagnetic Calorimeter in LHC Run2.” (2021) .
URL <http://cds.cern.ch/record/2798128>
- [47] A. M. Sirunyan *et al.* “Particle-flow reconstruction and global event description with the CMS detector.” *JINST* (2017) **12**:P10003. doi:10.1088/1748-0221/12/10/P10003. 1706.04965.
- [48] W. Adam, R. Frühwirth, A. Strandlie, and T. Todor. “Reconstruction of Electrons with the Gaussian-Sum Filter in the CMS Tracker at the LHC.” (2005) .
URL <https://cds.cern.ch/record/815410>
- [49] A. M. Sirunyan *et al.* “Electron and photon reconstruction and identification with the CMS experiment at the CERN LHC.” *JINST* (2021) **16**:P05014. doi:10.1088/1748-0221/16/05/P05014. 2012.06888.
- [50] R. Frühwirth. “Application of kalman filtering to track and vertex fitting.” *Nuclear Instruments and Methods in Physics Research Section A: Accelerators, Spectrometers, Detectors and Associated Equipment* (1987) **262** (2):444–450. ISSN 0168-9002. doi:[https://doi.org/10.1016/0168-9002\(87\)90887-4](https://doi.org/10.1016/0168-9002(87)90887-4).
URL <https://www.sciencedirect.com/science/article/pii/0168900287908874>
- [51] CMS Collaboration. “Muon reconstruction performance during run 2.” (2019) .
URL https://cds.cern.ch/record/2682902/files/DP2019_022.pdf
- [52] M. Cacciari, G. P. Salam, and G. Soyez. “The anti- k_T jet clustering algorithm.” *JHEP* (2008) **04**:063. doi:10.1088/1126-6708/2008/04/063. 0802.1189.
- [53] M. Cacciari, G. P. Salam, and G. Soyez. “FastJet user manual.” *Eur. Phys. J. C* (2012) **72**:1896. doi:10.1140/epjc/s10052-012-1896-2. 1111.6097.
- [54] A. M. Sirunyan *et al.* “Pileup mitigation at CMS in 13 TeV data.” *JINST* (2020) **15**:P09018. doi:10.1088/1748-0221/15/09/P09018. 2003.00503.

- [55] V. Khachatryan *et al.* “Jet energy scale and resolution in the CMS experiment in pp collisions at 8 TeV.” *JINST* (2017) **12**:P02014. doi:10.1088/1748-0221/12/02/P02014. 1607.03663.
- [56] K. Ackerstaff *et al.* “Search for anomalous production of dilepton events with missing transverse momentum in e^+e^- collisions at $\sqrt{s} = 161$ GeV and 172 GeV.” *Eur. Phys. J. C* (1998) **4**:47. doi:10.1007/PL00021655. [hep-ex/9710010](#).
- [57] M. Vesterinen and T. R. Wyatt. “A novel technique for studying the Z boson transverse momentum distribution at hadron colliders.” *Nucl. Instrum. Meth. A* (2009) **602**:432. doi:10.1016/j.nima.2009.01.203. 0807.4956.
- [58] A. M. Sirunyan *et al.* “Measurements of properties of the Higgs boson decaying into the four-lepton final state in pp collisions at $\sqrt{s} = 13$ TeV.” *JHEP* (2017) **11**:047. doi:10.1007/JHEP11(2017)047. 1706.09936.
- [59] A. M. Sirunyan *et al.* “Precision luminosity measurement in proton-proton collisions at $\sqrt{s} = 13$ TeV in 2015 and 2016 at CMS.” *Eur. Phys. J. C* (2021) **81**:800. doi:10.1140/epjc/s10052-021-09538-2. 2104.01927.
- [60] “CMS luminosity measurement for the 2017 data-taking period at $\sqrt{s} = 13$ TeV.” *CMS Physics Analysis Summary CMS-PAS-LUM-17-004* (2018). URL <https://cds.cern.ch/record/2621960>
- [61] “CMS luminosity measurement for the 2018 data-taking period at $\sqrt{s} = 13$ TeV.” *CMS Physics Analysis Summary CMS-PAS-LUM-18-002* (2019). URL <https://cds.cern.ch/record/2676164>
- [62] S. Alioli, P. Nason, C. Oleari, and E. Re. “NLO Higgs boson production via gluon fusion matched with shower in POWHEG.” *JHEP* (2009) **04**:002. doi:10.1088/1126-6708/2009/04/002. 0812.0578.
- [63] P. Nason and C. Oleari. “NLO Higgs boson production via vector-boson fusion matched with shower in POWHEG.” *JHEP* (2010) **02**:037. doi:10.1007/JHEP02(2010)037. 0911.5299.
- [64] J. Alwall, R. Frederix, S. Frixione, V. Hirschi, F. Maltoni, *et al.* “The automated computation of tree-level and next-to-leading order differential cross sections, and their matching to parton shower simulations.” *JHEP* (2014) **07**:079. doi:10.1007/JHEP07(2014)079. 1405.0301.

- [65] S. Frixione, P. Nason, and G. Ridolfi. “A Positive-weight next-to-leading-order Monte Carlo for heavy flavour hadroproduction.” *JHEP* (2007) **09**:126. doi:10.1088/1126-6708/2007/09/126. 0707.3088.
- [66] C. Anastasiou, C. Duhr, F. Dulat, E. Furlan, T. Gehrmann, *et al.* “High precision determination of the gluon fusion Higgs boson cross-section at the LHC.” *JHEP* (2016) **05**:058. doi:10.1007/JHEP05(2016)058. 1602.00695.
- [67] M. Cacciari, F. A. Dreyer, A. Karlberg, G. P. Salam, and G. Zanderighi. “Fully differential vector-boson-fusion higgs production at next-to-next-to-leading order.” *Phys. Rev. Lett.* (2015) **115**:082002. doi:10.1103/PhysRevLett.115.082002. [Erratum: doi:10.1103/PhysRevLett.120.139901].
URL <https://link.aps.org/doi/10.1103/PhysRevLett.115.082002>
- [68] O. Brein, A. Djouadi, and R. Harlander. “NNLO QCD corrections to the Higgs-strahlung processes at hadron colliders.” *Phys. Lett. B* (2004) **579**:149. doi:10.1016/j.physletb.2003.10.112. hep-ph/0307206.
- [69] S. Dawson, C. Jackson, L. H. Orr, L. Reina, and D. Wackerlo. “Associated Higgs production with top quarks at the large hadron collider: NLO QCD corrections.” *Phys. Rev. D* (2003) **68**:034022. doi:10.1103/PhysRevD.68.034022. hep-ph/0305087.
- [70] T. Sjöstrand, S. Ask, J. R. Christiansen, R. Corke, N. Desai, *et al.* “An introduction to PYTHIA 8.2.” *Comput. Phys. Commun.* (2015) **191**:159. doi:10.1016/j.cpc.2015.01.024. 1410.3012.
- [71] V. Khachatryan *et al.* “Event generator tunes obtained from underlying event and multiparton scattering measurements.” *Eur. Phys. J. C* (2016) **76**:155. doi:10.1140/epjc/s10052-016-3988-x. 1512.00815.
- [72] A. M. Sirunyan *et al.* “Extraction and validation of a new set of CMS PYTHIA8 tunes from underlying-event measurements.” *Eur. Phys. J. C* (2020) **80**:4. doi:10.1140/epjc/s10052-019-7499-4. 1903.12179.
- [73] R. D. Ball *et al.* “Parton distributions for the LHC run II.” *JHEP* (2015) **04**:040. doi:10.1007/JHEP04(2015)040. 1410.8849.
- [74] R. D. Ball, V. Bertone, F. Cerutti, L. Del Debbio, S. Forte, *et al.* “Parton distributions from high-precision collider data.” *Eur. Phys. J. C* (2017) **77**:663. doi:10.1140/epjc/s10052-017-5199-5. 1706.00428.
- [75] “Geant4—a simulation toolkit.” *Nucl. Instrum. Meth. A* (2003) **506**:250. ISSN 0168-9002. doi:10.1016/S0168-9002(03)01368-8.

- [76] W. Erdmann. “Offline primary vertex reconstruction with deterministic annealing clustering.” *CMS Internal note* (2011) **2011/014**.
- [77] <https://twiki.cern.ch/twiki/bin/viewauth/CMS/L1PrefiringWeightRecipe>.
- [78] S. Chatrchyan *et al.* “Measurement of the inclusive W and Z production cross sections in pp collisions at $\sqrt{s} = 7$ TeV.” *JHEP* (2011) **10**:132. doi:10.1007/JHEP10(2011)132. 1107.4789.
- [79] <https://twiki.cern.ch/twiki/bin/view/CMS/MultivariatePhotonIdentificationRun2>.
- [80] <https://twiki.cern.ch/twiki/bin/view/CMS/MultivariateElectronIdentificationRun2>.
- [81] <https://twiki.cern.ch/twiki/bin/viewauth/CMS/EndcapHighPtMuonEfficiencyProblem>.
- [82] <https://docs.google.com/presentation/d/1PMWr9QEaHYAbyi6yAFLHEE6KT-u7Cjwm3wniJZCixcU/edit#slide=id.p>.
- [83] <https://twiki.cern.ch/twiki/bin/view/CMS/RochcorMuon>.
- [84] J. S. Gainer, W.-Y. Keung, I. Low, and P. Schwaller. “Looking for a light Higgs boson in the $Z\gamma \rightarrow \ell\ell\gamma$ channel.” *Phys. Rev. D* (2012) **86**:033010. doi:10.1103/PhysRevD.86.033010. 1112.1405.
- [85] J. S. Gainer, K. Kumar, I. Low, and R. Vega-Morales. “Improving the sensitivity of Higgs boson searches in the golden channel.” *JHEP* (2011) **11**:027. doi:10.1007/JHEP11(2011)027. 1108.2274.
- [86] D. L. Rainwater, R. Szalapski, and D. Zeppenfeld. “Probing color singlet exchange in $Z +$ two jet events at the CERN LHC.” *Phys. Rev. D* (1996) **54**:6680. doi:10.1103/PhysRevD.54.6680. hep-ph/9605444.
- [87] M. J. Oreglia. “A study of the reactions $\psi' \rightarrow \gamma\gamma\psi'$.” Ph.D. thesis, Stanford University (1980). SLAC Report SLAC-R-236, see Appendix D.
URL <http://www.slac.stanford.edu/pubs/slacreports/slac-r-236.html>
- [88] P. D. Dauncey, M. Kenzie, N. Wardle, and G. J. Davies. “Handling uncertainties in background shapes.” *JINST* (2015) **10**:P04015. doi:10.1088/1748-0221/10/04/P04015. 1408.6865.
- [89] CMS Collaboration. “Search for a higgs boson decaying into a z boson and a photon in pp collisions at $\sqrt{s} = 7$ and 8 tev.” *Phys. Lett. B* (2013) **726**:587––609.

- [90] A. D. Martin, W. J. Stirling, R. S. Thorne, and G. Watt. “Parton distributions for the LHC.” *Eur. Phys. J. C* (2009) **63**:189. doi:10.1140/epjc/s10052-009-1072-5. 0901.0002.
- [91] H. Lai, M. Guzzi, J. Huston, Z. Li, P. M. Nadolsky, *et al.* “New parton distributions for collider physics.” *Phys. Rev. D* (2010) **82**:74024. doi:10.1103/PhysRevD.82.074024. 1007.2241.
- [92] J. Butterworth *et al.* “PDF4LHC recommendations for LHC run II.” *J. Phys. G* (2016) **43**:023001. doi:10.1088/0954-3899/43/2/023001. 1510.03865.
- [93] A. M. Sirunyan *et al.* “Measurement of the inelastic proton-proton cross section at $\sqrt{s} = 13$ TeV.” *JHEP* (2018) **07**:161. doi:10.1007/JHEP07(2018)161. 1802.02613.
- [94] R. A. Fisher. “On the mathematical foundations of theoretical statistics.” *Phil. Trans. Roy. Soc. Lond.* (1922) **222**:309. doi:10.1098/rsta.1922.0009.
- [95] ATLAS and CMS Collaborations, The LHC Higgs combination group. “Procedure for the LHC Higgs boson search combination in summer 2011.” *Technical Report CMS-NOTE-2011-005. ATL-PHYS-PUB-2011-11* (2011).
URL <https://cds.cern.ch/record/1379837>
- [96] A. L. Read. “Presentation of search results: The CL_s technique.” *J. Phys. G* (2002) **28**:2693. doi:10.1088/0954-3899/28/10/313.
- [97] T. Junk. “Confidence level computation for combining searches with small statistics.” *Nucl. Instrum. Meth. A* (1999) **434**:435. doi:10.1016/S0168-9002(99)00498-2. hep-ex/9902006.
- [98] G. Cowan, K. Cranmer, E. Gross, and O. Vitells. “Asymptotic formulae for likelihood-based tests of new physics.” *Eur. Phys. J. C* (2011) **71**:1554. doi:10.1140/epjc/s10052-011-1554-0. [Erratum: doi:10.1140/epjc/s10052-013-2501-z], 1007.1727.

APPENDIX A

Shower Shape Corrections

For each shower shape variable, the three plots at the top (bottom) correspond to the barrel (endcaps). From left to right, the plots represent 2016, 2017, and 2018. All distributions are from $Z \rightarrow e^+e^-$ events.

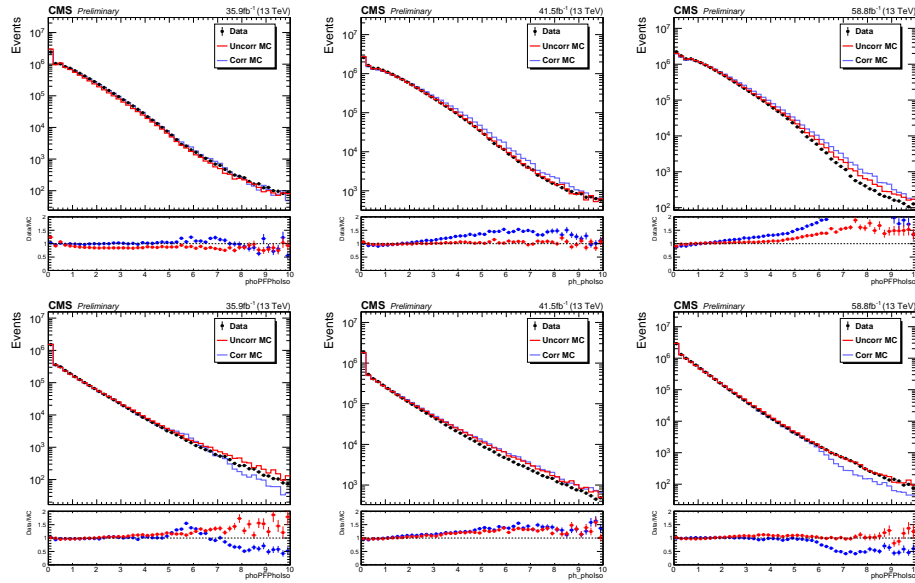


Figure A.1. Shower shape correction for the photon isolation.

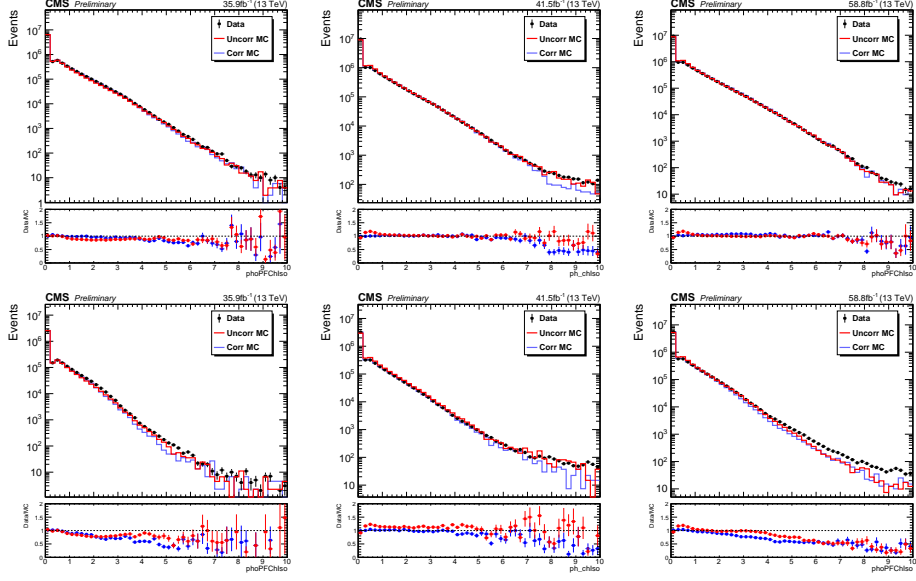


Figure A.2. Shower shape correction for the charged hadron isolation.

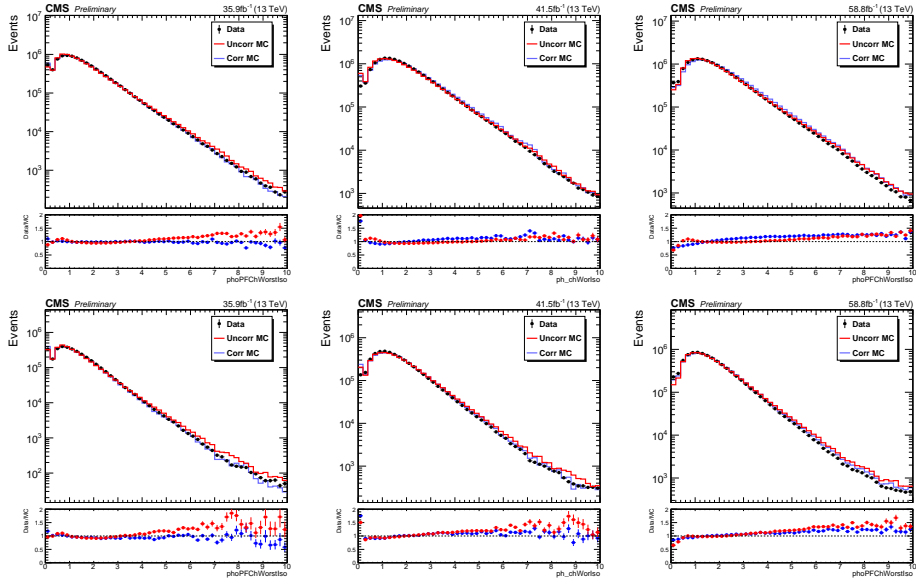


Figure A.3. Shower shape correction for the charged hadron isolation with worst vertex.

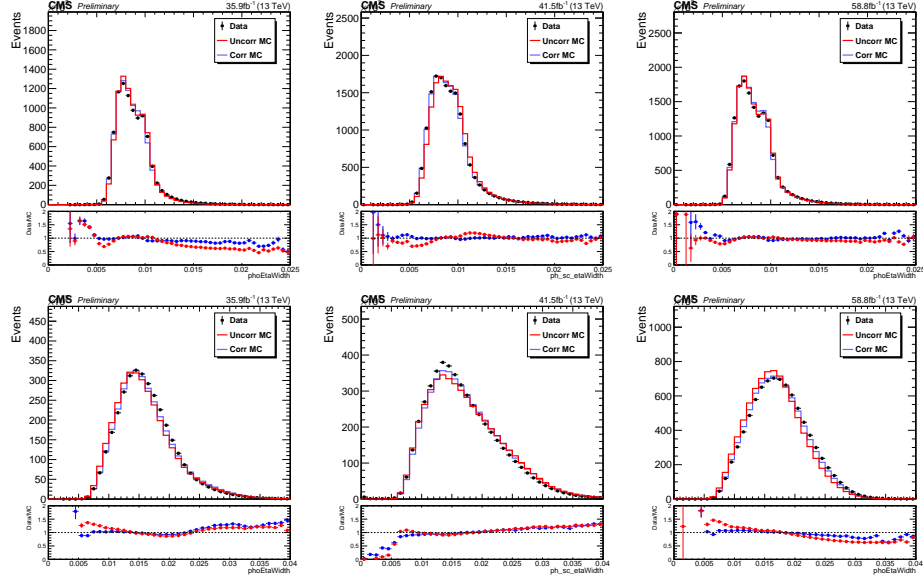


Figure A.4. Shower shape correction for the η width.

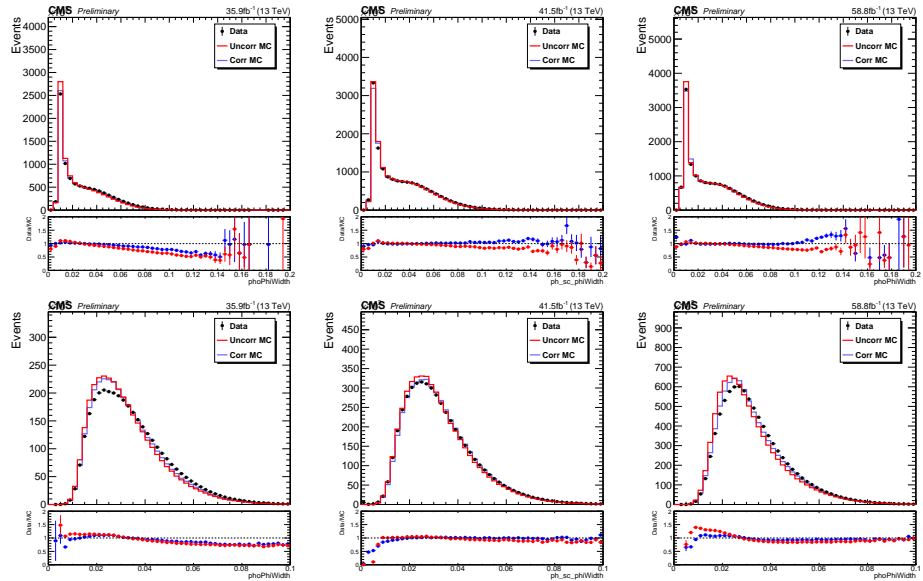
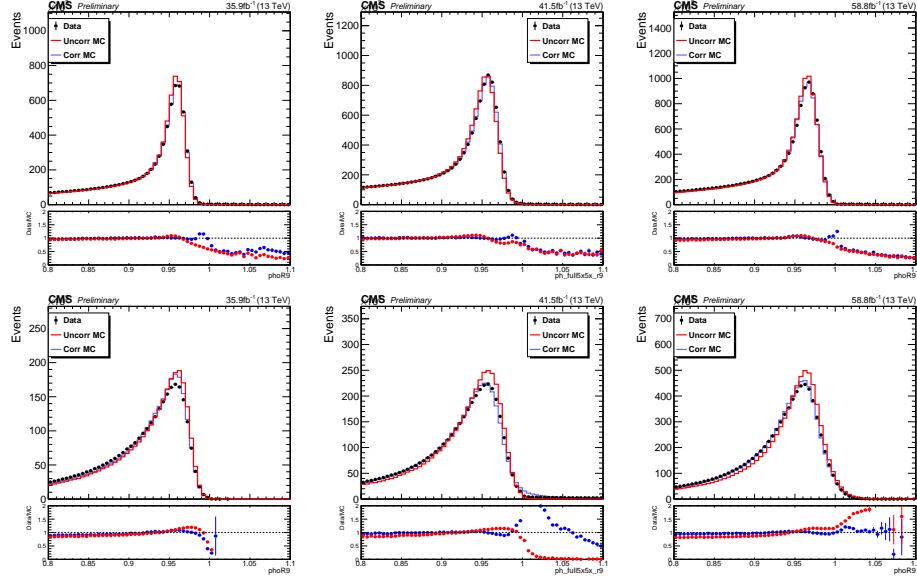
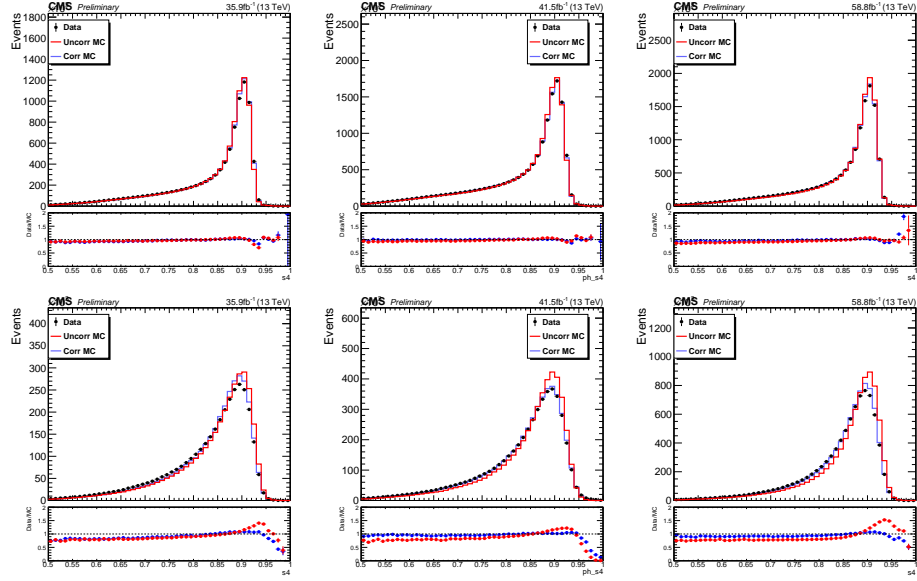
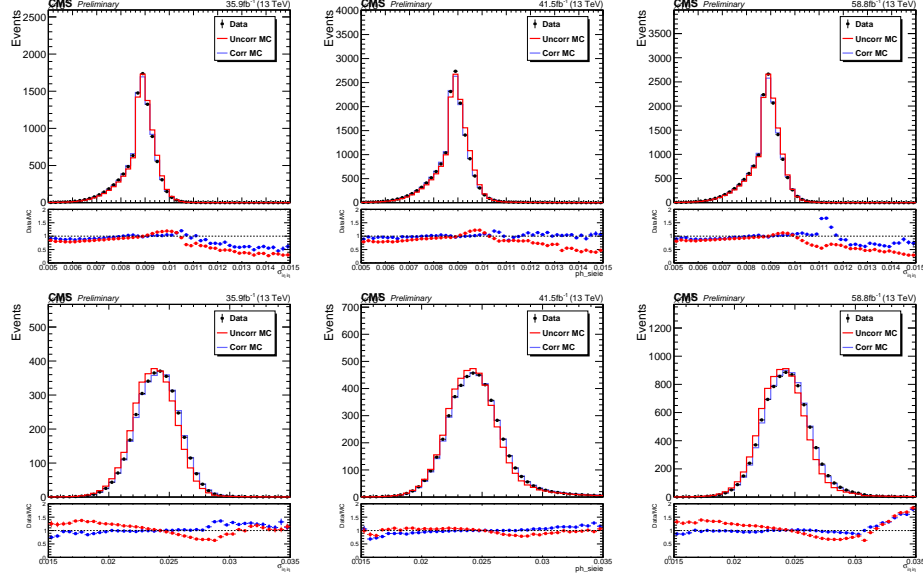
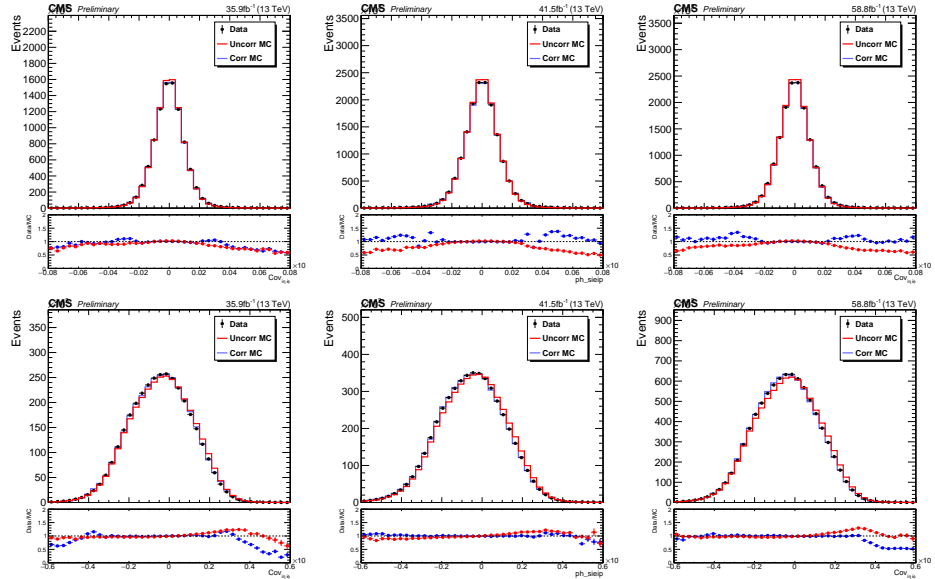


Figure A.5. Shower shape correction for the ϕ width.

Figure A.6. Shower shape correction for the variable R_9 .Figure A.7. Shower shape correction for the variable S_4 .

Figure A.8. Shower shape correction for the variable $\sigma_{i\eta i\eta}$.Figure A.9. Shower shape correction for the variable $\sigma_{i\eta i\phi}$.

APPENDIX B

Signal Fits

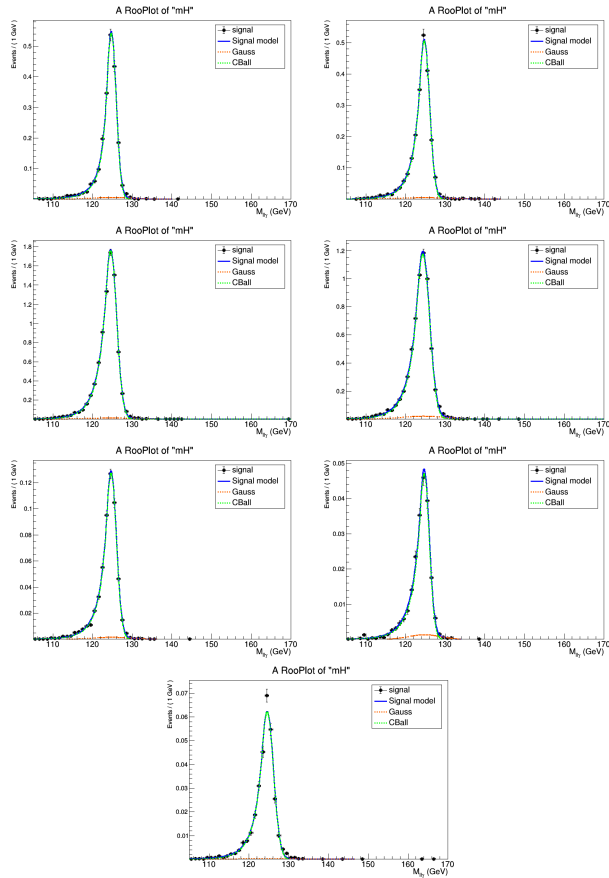


Figure B.1. Fits to simulated $m_{\ell^+\ell^-\gamma}$ signal distributions in the electron channel for $m_H = 125$ GeV for the 2016 data-taking period. The top four plots correspond to the untagged categories, and the bottom three plots correspond to the dijet categories.

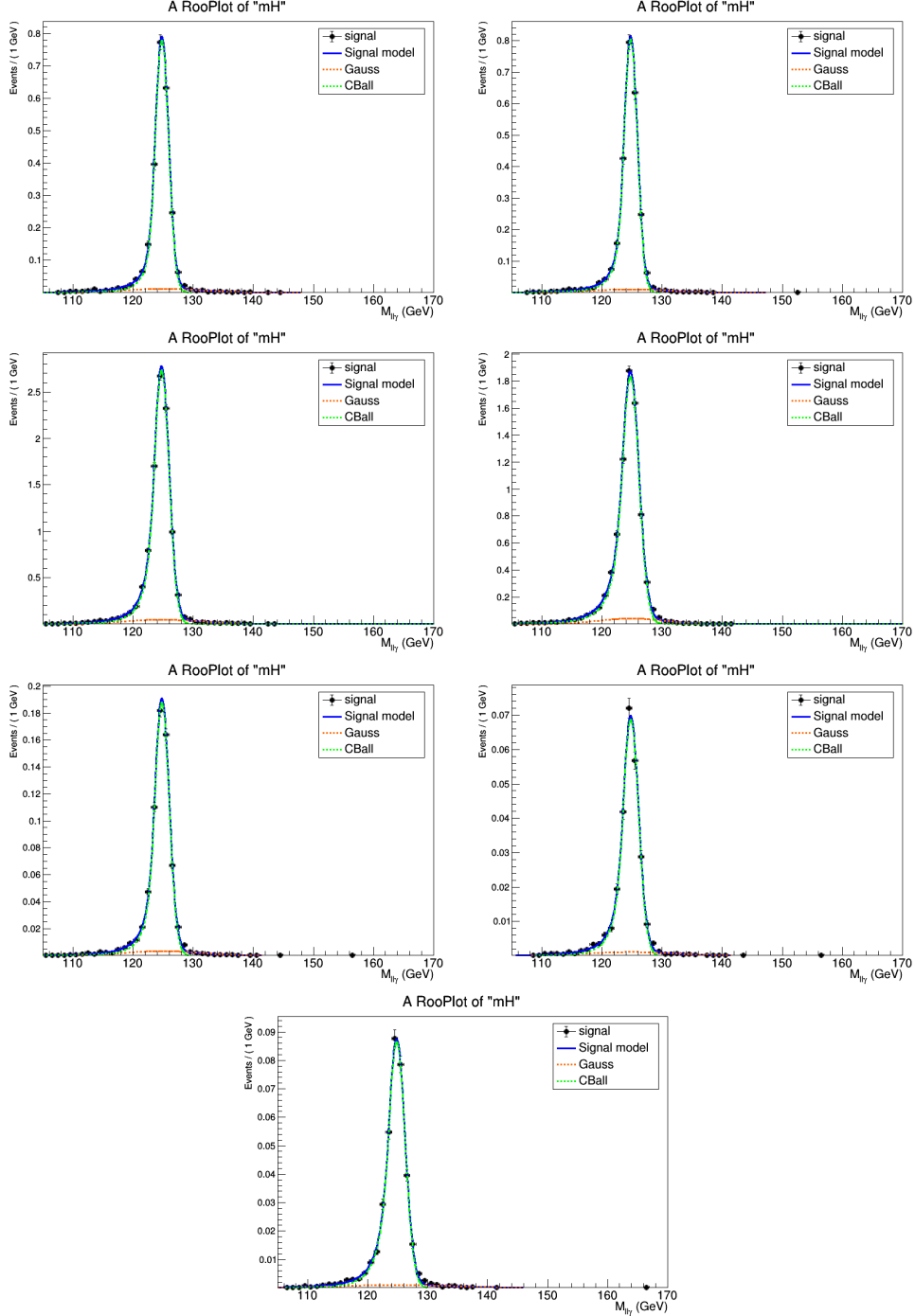


Figure B.2. Fits to simulated $m_{\ell^+\ell^-\gamma}$ signal distributions in the muon channel for $m_H = 125$ GeV for the 2016 data-taking period. The top four plots correspond to the untagged categories, and the bottom three plots correspond to the dijet categories.

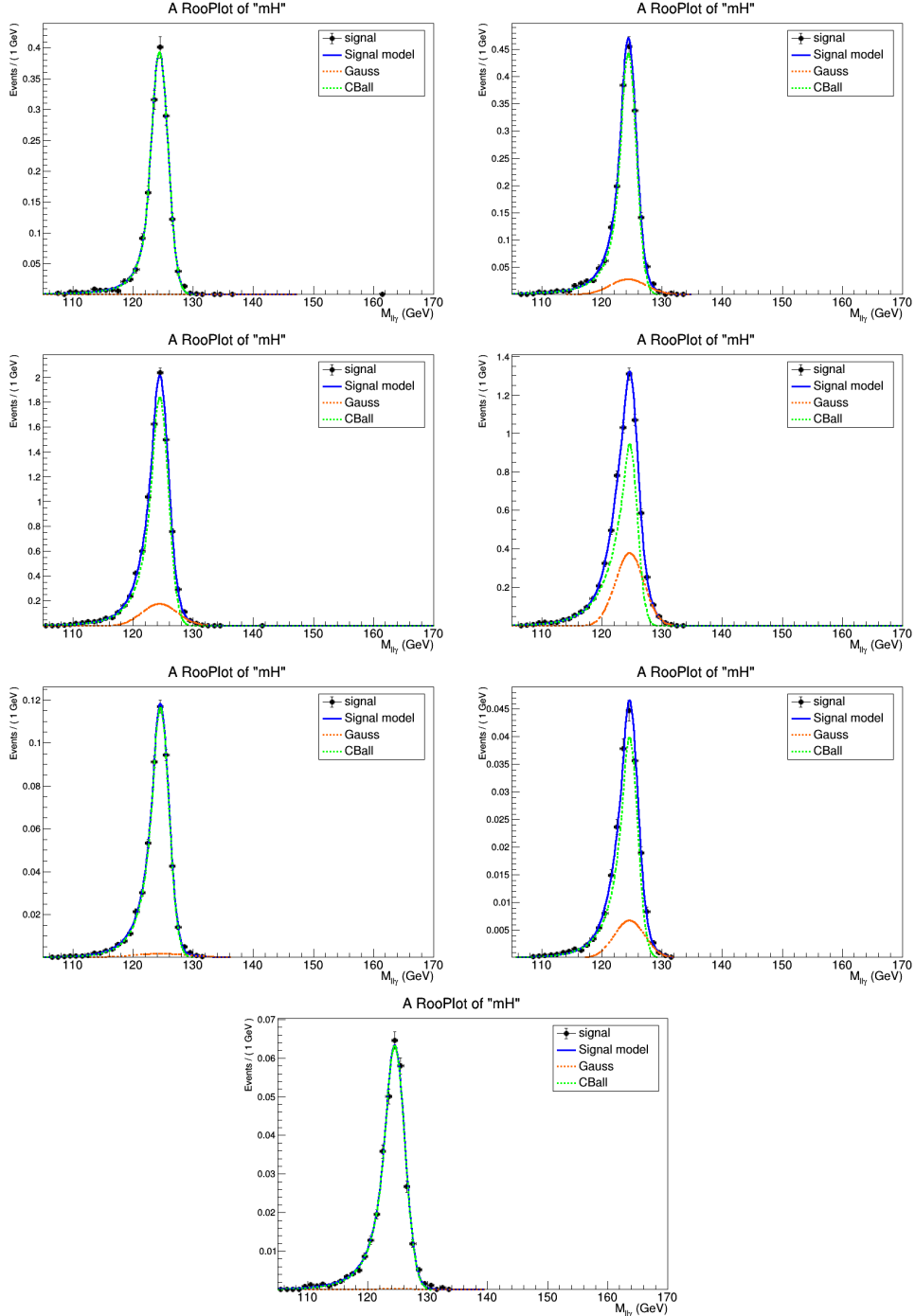


Figure B.3. Fits to simulated $m_{\ell^+\ell^-\gamma}$ signal distributions in the electron channel for $m_H = 125$ GeV for the 2017 data-taking period. The top four plots correspond to the untagged categories, and the bottom three plots correspond to the dijet categories.

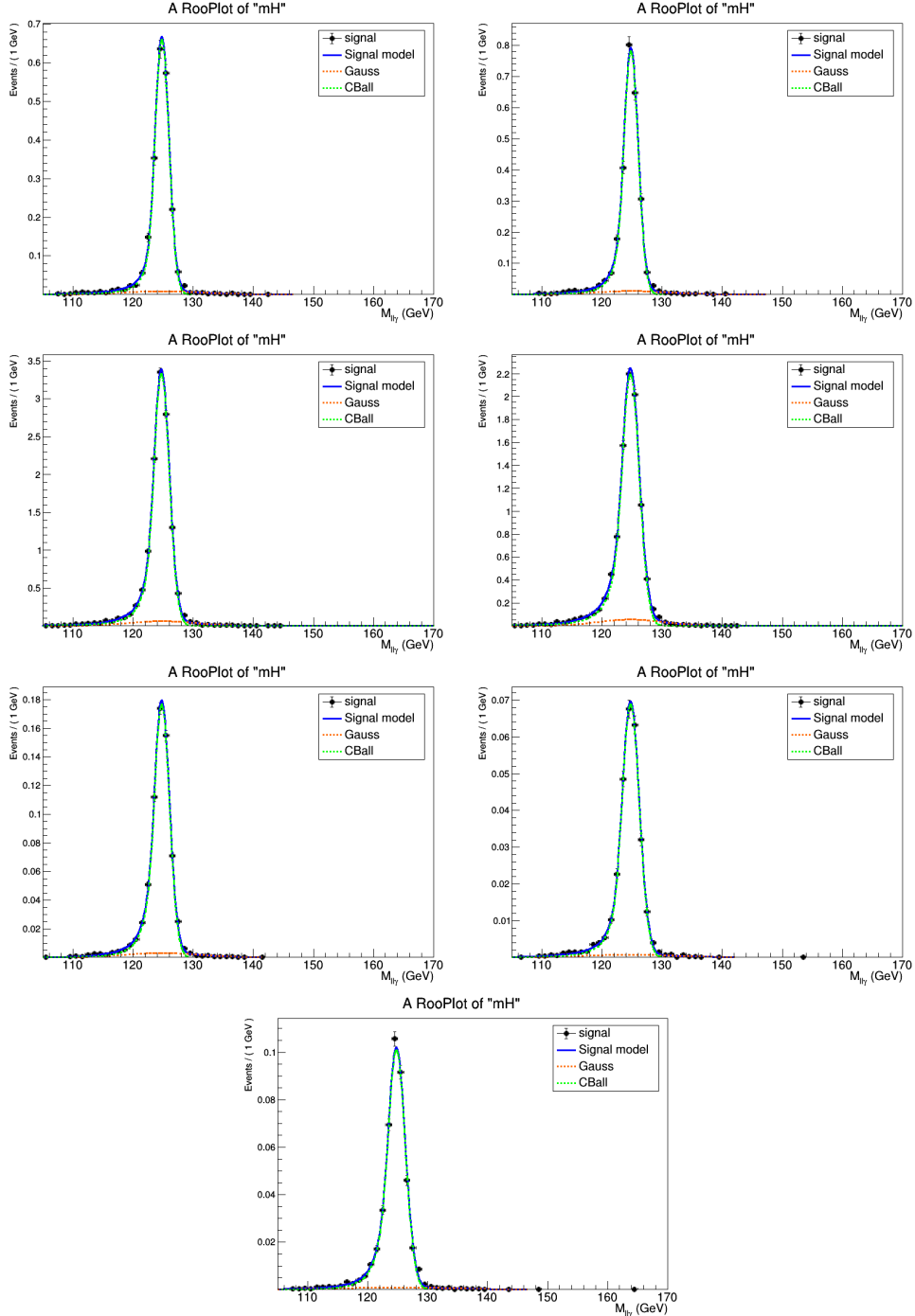


Figure B.4. Fits to simulated $m_{\ell^+\ell^-\gamma}$ signal distributions in the muon channel for $m_H = 125$ GeV for the 2017 data-taking period. The top four plots correspond to the untagged categories, and the bottom three plots correspond to the dijet categories.

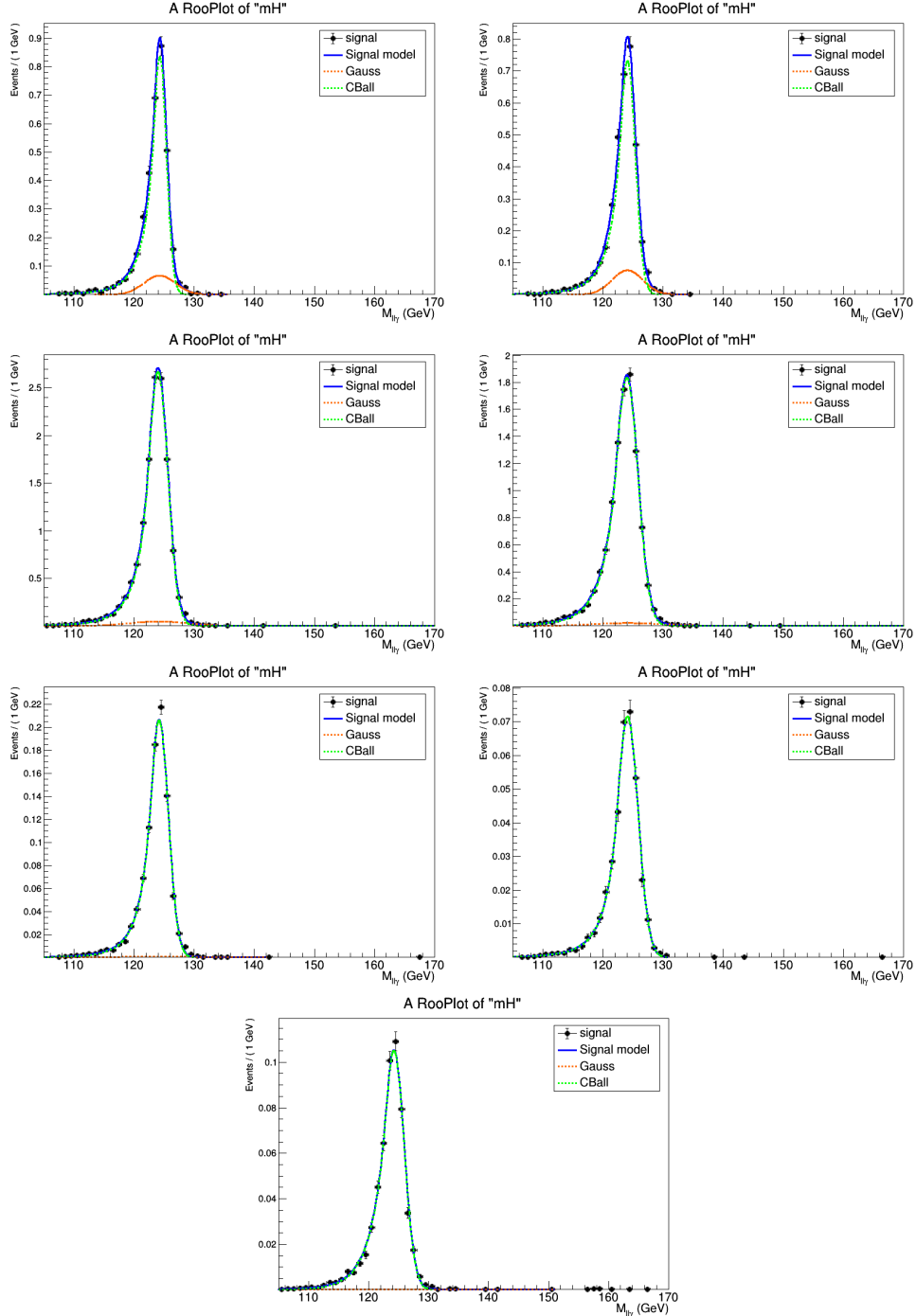


Figure B.5. Fits to simulated $m_{\ell^+\ell^-\gamma}$ signal distributions in the electron channel for $m_H = 125$ GeV for the 2018 data-taking period. The top four plots correspond to the untagged categories, and the bottom three plots correspond to the dijet categories.

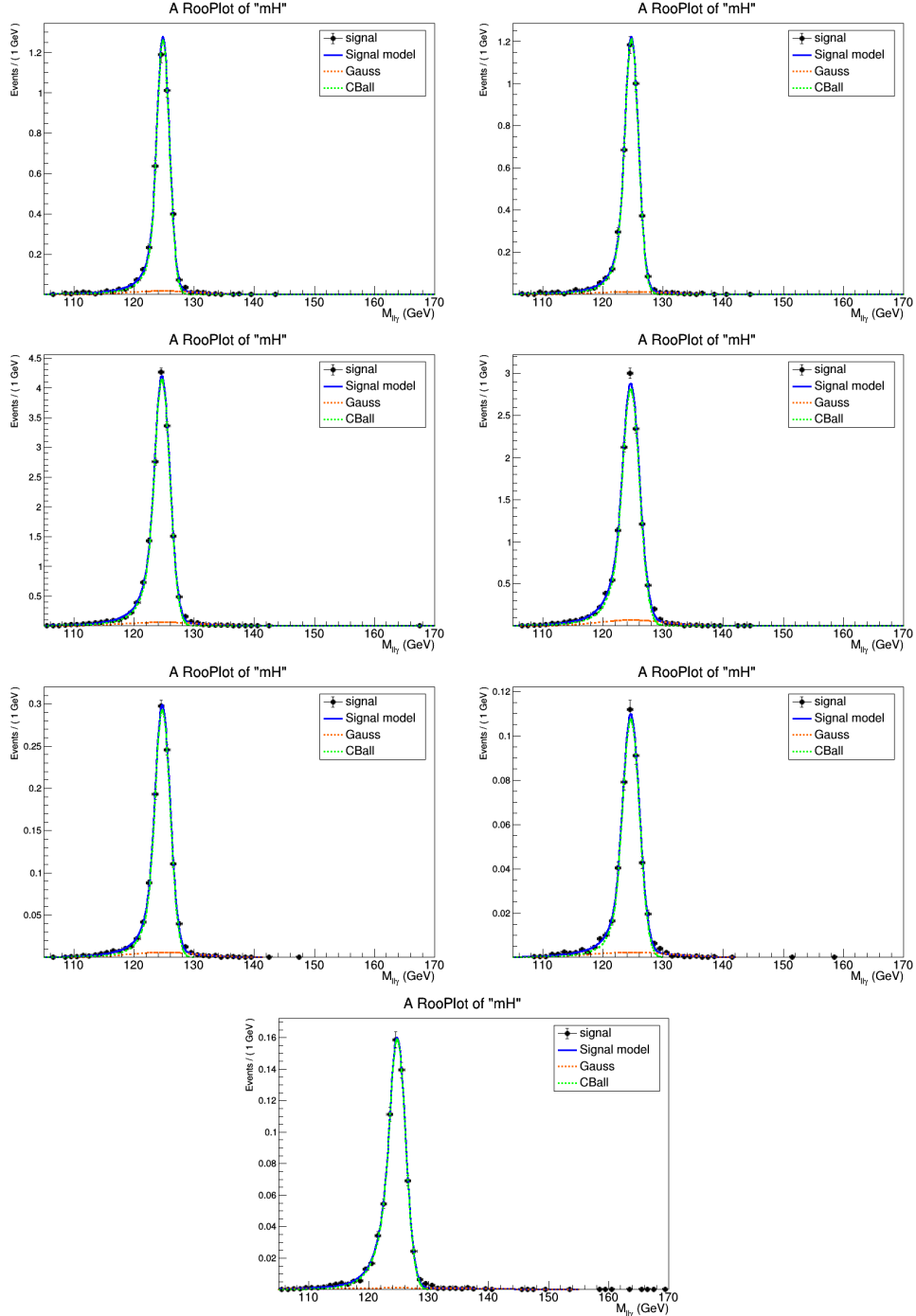


Figure B.6. Fits to simulated $m_{\ell^+\ell^-\gamma}$ signal distributions in the muon channel for $m_H = 125$ GeV for the 2018 data-taking period. The top four plots correspond to the untagged categories, and the bottom three plots correspond to the dijet categories.

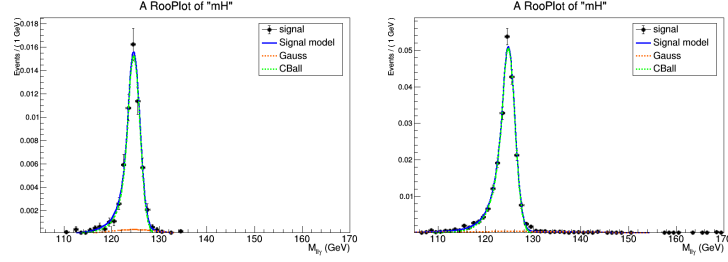


Figure B.7. Fits to simulated $m_{\ell^+\ell^-\gamma}$ signal distributions in the electron and muon channels combined in the lepton-tagged category for $m_H = 125$ GeV for the 2016 data-taking period. The left plot shows the fit to simulated ZH production events, and the right plot shows the fit to simulated WH production events.

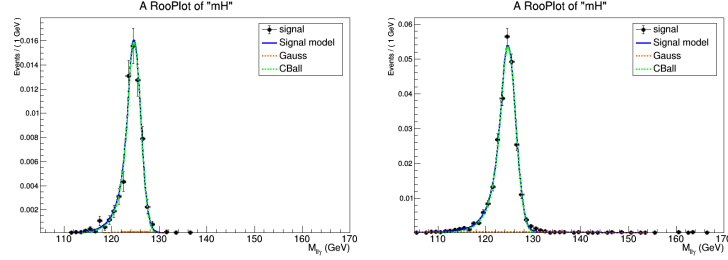


Figure B.8. Fits to simulated $m_{\ell^+\ell^-\gamma}$ signal distributions in the electron and muon channels combined in the lepton-tagged category for $m_H = 125$ GeV for the 2017 data-taking period. The left plot shows the fit to simulated ZH production events, and the right plot shows the fit to simulated WH production events.

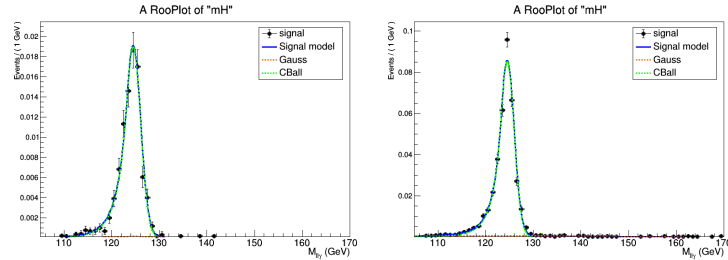


Figure B.9. Fits to simulated $m_{\ell^+\ell^-\gamma}$ signal distributions in the electron and muon channels combined in the lepton-tagged category for $m_H = 125$ GeV for the 2018 data-taking period. The left plot shows the fit to simulated ZH production events, and the right plot shows the fit to simulated WH production events.

APPENDIX C

Resonant Background Fits

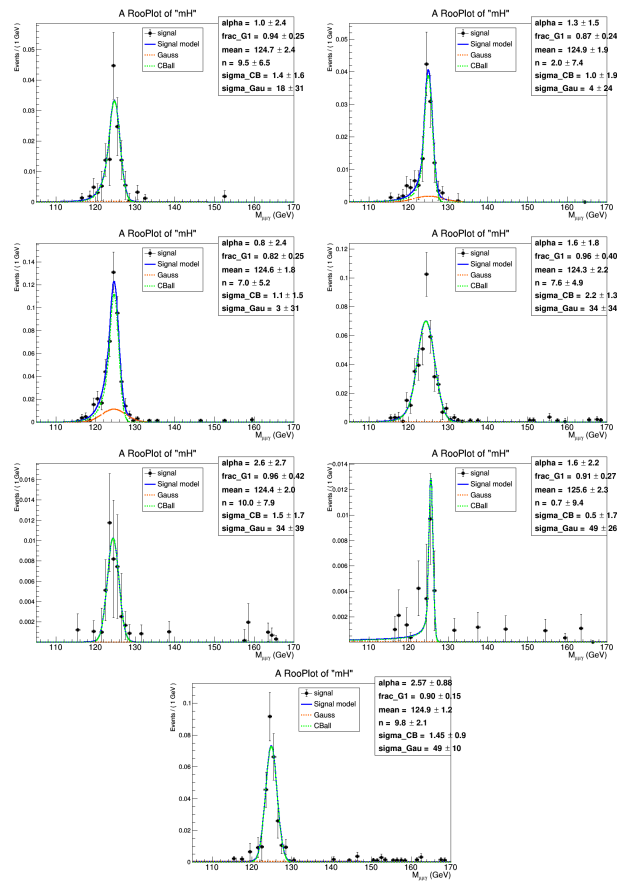


Figure C.1. Fits to simulated $m_{\mu^+\mu^-\gamma}$ resonant background distributions from $H \rightarrow \mu^+\mu^-$ for $m_H = 125$ GeV for the 2016 data-taking period. The blue line shows the total fit function, the green line shows the Crystal Ball function component, and the red line shows the Gaussian function component. The top four plots correspond to the untagged categories, and the bottom three plots correspond to the dijet categories.

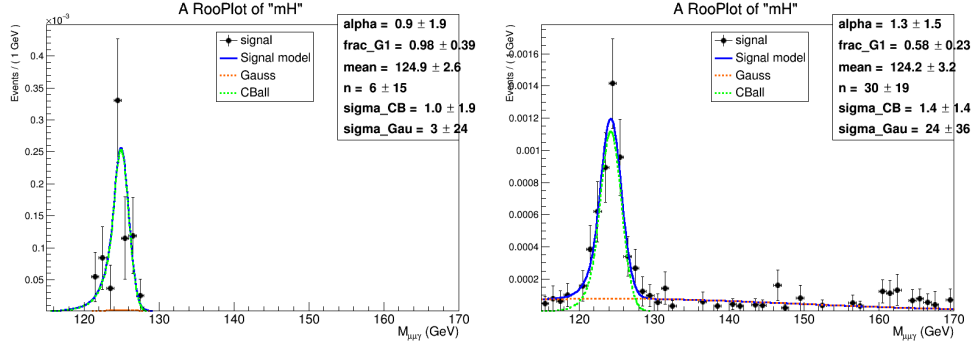


Figure C.2. Fits to simulated $m_{\ell^+\ell^-\gamma}$ resonant background distributions from $H \rightarrow \mu^+\mu^-$ in the electron and muon channels combined in the lepton-tagged category for $m_H = 125$ GeV for the 2016 data-taking period. The left plot shows the fit to simulated ZH production events, and the right plot shows the fit to simulated WH production events. The blue line shows the total fit function, the green line shows the Crystal Ball function component, and the red line shows the Gaussian function component.

APPENDIX D

Nuisance Parameter Impacts

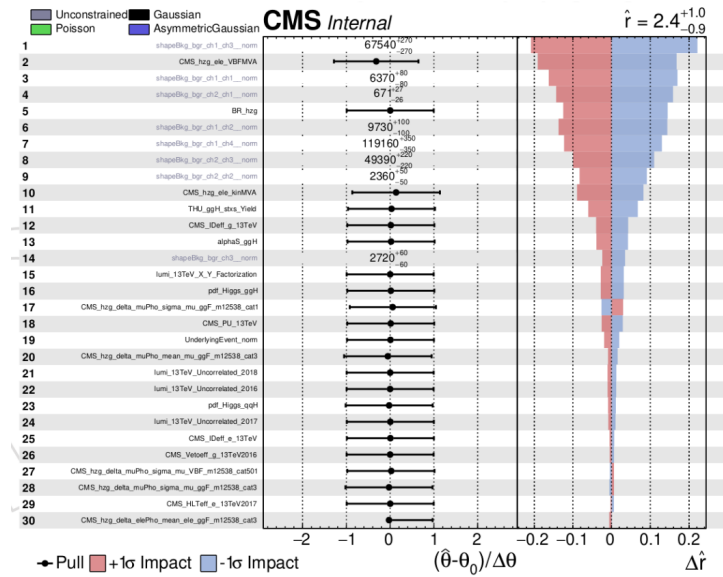


Figure D.1. Observed nuisance parameter impacts on the signal strength in the $H \rightarrow Z\gamma$ search.

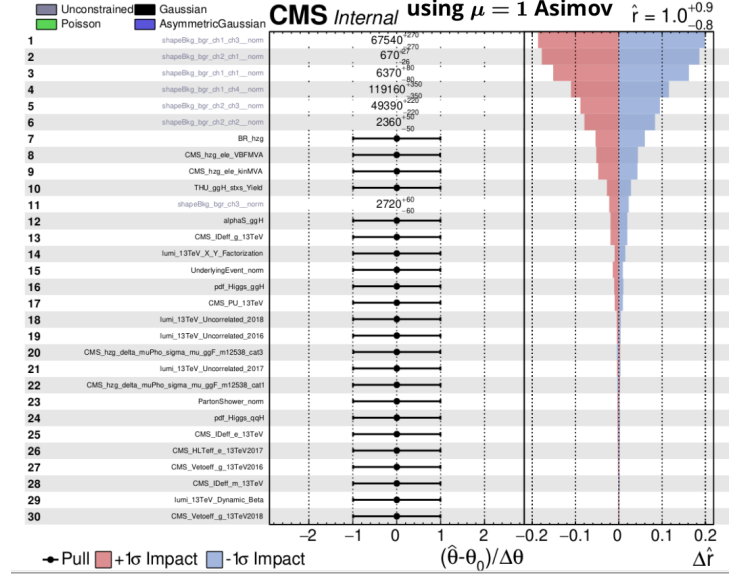
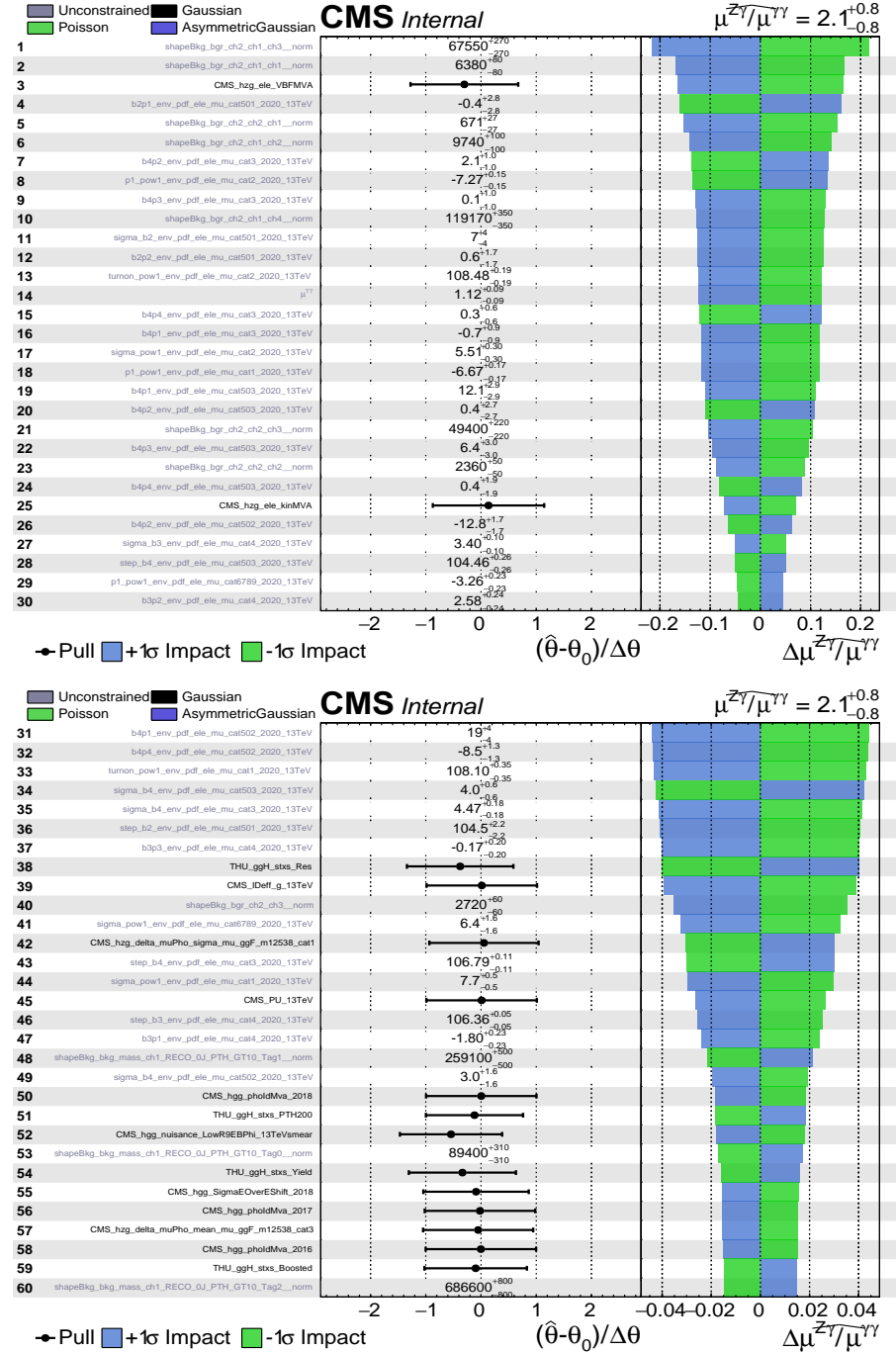


Figure D.2. Expected nuisance parameter impacts under the SM hypothesis on the signal strength in the $H \rightarrow Z\gamma$ search.

Figure D.2. Nuisance parameter impacts on $\mu_{Z\gamma}/\mu_{\gamma\gamma}$.